Advancing Ultra-High Field MRI functional and structural applications

Ícaro Oliveira

Advancing Ultra-High Field MRI functional and structural applications

Ícaro Agenor Ferreira de Oliveira

VRIJE UNIVERSITEIT

ADVANCING ULTRA-HIGH FIELD MRI FUNCTIONAL AND STRUCTURAL APPLICATIONS

ACADEMISCH PROEFSCHRIFT

ter verkrijging van de graad Doctor aan
de Vrije Universiteit Amsterdam,
op gezag van de rector magnificus
prof.dr. J.J.G. Geurts,
in het openbaar te verdedigen
ten overstaan van de promotiecommissie
van de Faculteit der Gedrags- en Bewegingswetenschappen
op donderdag 6 oktober 2022 om 13.45 uur
in een bijeenkomst van de universiteit,
De Boelelaan 1105

door

Icaro Agenor Ferreira de Oliveira

geboren te Ribeirão Preto, Brazilië

promotor:	prof.dr. S.O. Dumoulin
copromotoren:	dr.ir. J.C.W. Siero dr.ir. W. van der Zwaag
promotiecommissie:	prof.dr. D.J. Veltman dr. T.H.J. Knapen prof.dr. M. Callaghan prof.dr.ir. M.J.P. Van Osch dr. I. Jelescu

Contents

	Summary	5
Chapter 1	General introduction and thesis outline	7
Chapter 2	Can 7T MPRAGE match MP2RAGE for gray-white matter contrast?	21
Chapter 3	Comparing hand movement rate dependence of cerebral blood volume and BOLD responses at 7T	53
Chapter 4	Improved selectivity in 7T digit motor mapping using VASO-CBV	81
Chapter 5	Comparing BOLD and VASO-CBV population receptive field estimates in human visual cortex	102
Chapter 6	General discussion	134
	Curriculum Vitae	141
	List of Publications	142
	Acknowledgements	144

Summary

Magnetic resonance imaging (MRI) has shown to be a valuable tool for studying the human brain, allowing in-vivo visualization of structures and anatomy in great detail, especially at Ultra-High field strengths (≥ 7T). MRI is not limited by anatomical and structural information. It can study the brain's anatomy, functionality, connectivity (functional and structural), and chemical metabolism. Functional MRI (fMRI), for instance, enables the investigation of brain function mechanisms in-vivo with a non-invasive advantage compared to other tools.

The present thesis focuses on advanced MRI techniques for ultra-high field strength (≥ 7T), specifically for neuroscience applications. Combined with the higher field strength, these techniques provide better imaging quality and precise brain activity measurement. For example, high-quality anatomical T1 weighted images are essential for several MRI applications, notably, to serve as an anatomical reference in fMRI and gray matter segmentation. Unfortunately, increased field strength also induces non-uniformities in the transmit field ($B1^+$) that can compromise image contrast non-uniformly. One of the goals of the present thesis was to investigate new strategies to overcome this issue.

Regarding the functional brain investigation, the gradient-echo (GRE) is the typical method of choice for fMRI applications. Despite its high sensitivity to deoxyhemoglobin variations and widespread availability, the gradient-echo (GRE) BOLD signal is predominantly driven by the large draining vessels resulting in a limited spatial specificity, especially for 7T or higher field strength applications in which the BOLD sensitivity (susceptibility effect) is higher compared to lower static field scanners. In this context, we investigated an alternative fMRI method called vascular space occupancy (VASO) that promises higher spatial specificity than the typical GRE BOLD.

To achieve the aim of this thesis, we used four approaches (chapters 2-5). We first evaluated the universal pulses capabilities in combination with a more adiabatic inversion pulse (TR-FOCI) to mitigate the UHF inhomogeneity problem, evaluating the contrast enhancement of the T1-weighted image from the MPRAGE sequence in comparison to the T1-weighted image of the self-bias MP2RAGE sequence (***Chapter 2***), and we found that these combinations can mitigate the inhomogeneity problem and increase the image quality of T1-weighted

MPRAGE. For the second part of this thesis, we focused on the VASO fMRI approach; for our first fMRI assessment (***Chapter 3***), we implemented the Slab Selective Slab Inversion (SS-SI) VASO sequence. We investigated the linearity behavior of the VASO-CBV responses, comparing their behavior with respect to the movement rate in the motor cortex with BOLD responses. We observed a strong linear relationship between VASO-CBV and BOLD responses.

We used response selectivity measurements to investigate the cortical activation with sub-millimeter VASO-CBV and BOLD fMRI data during individual finger movement (***Chapter 4***). We found that the higher vascular specificity of VASO-CBV fMRI results in higher response selectivity or less vascular overlap than BOLD imaging. Finally, we investigated how VASO-CBV compares to BOLD fMRI for cognitive neuroscience applications in the visual cortex (***Chapter 5***). We show similar eccentricity and polar angle maps. Likewise, the pRF size estimates were similar between VASO-CBV and BOLD.

This work brings the ability to improve image quality and overcome typical challenges of ultra-high field MRI for both anatomical and functional applications. I hope that the neuroscience and technical fundaments discussed here can further contribute to the developing field of MRI and neuroimaging.

Chapter 1

General Introduction and thesis outline

General Introduction

The human brain is the most important organ of the nervous system. Our brain is in charge of coordinating all the vital functions of our body, making sense of what is happening around us. The brain receives signals from the outside world through our five senses; sight, smell, touch, taste, and hearing. The brain interprets this information, releases chemicals, and sends electrical signals to cause the body to respond.

The brain not only regulates our bodies and our movements but is also the home of our minds. Our minds constantly control the flow of information, memories, thoughts, emotion, and imagination, working as a network. The flow of information is sent to different brain parts along neurons and relies on the brain's underlying structure and chemical composition to function successfully.

Magnetic resonance (MR) has empowered neuroscience with a fantastic tool to investigate the brain's inner structure and function in vivo. Although brain research has made considerable progress over recent years, especially after neuroimaging technology such as MRI, many questions remain unsolved. A thorough investigation and validation of the newly available tools and techniques are needed to answer those questions reliably.

MRI at Ultra-High fields

Magnetic resonance imaging (MRI) is the most efficient investigative tool of choice for many clinical diagnoses and research applications (Ledig et al., 2018; MacDonald and Frayne, 2015; Meijer et al., 2017; O'Brien et al., 2014a; Rüber et al., 2018). From a neuroimaging perspective, MRI can study the brain's anatomy, functionality, connectivity (functional and structural), and chemical metabolism. Its diversity and broad applicability are the pillars of its efficiency and popularity.

Anatomical, T1-weighted (MRI) are essential for several MRI applications in clinical and research settings. Regarding the clinical applications, T1-weighted images are used to assess structural details. For example, it is often used with exogenous contrasts in clinical routine to enhance the signal contrast. For research applications, because of the excellent contrast between gray and white matter, the T1w serves as an anatomical reference in functional MRI

(fMRI) and is often used for gray-matter segmentation. Moreover, it can benefit substantially from the use of Ultra-High Field (UHF, ≥ 7T). Compared to conventional, clinical, field strengths, imaging at 7T offers a higher signal-to-noise ratio (SNR), which can be traded for an increased spatial resolution to reduce partial volume effects and more precise cortical measurements. The increased use of UHF scanners resulted in a significant increase in submillimetre topographic and cortical-depth dependent studies (Fracasso et al., 2016; Gulban et al., 2018; Huber et al., 2017; Kashya et al., 2018). As a result, many cortical areas have been identified or used to support previous findings (Dumoulin et al., 2017; Wiggins et al., 2017).

Additionally to the increase in SNR, the higher static field affect other MR parameters and the image contrast (T1, T2, and T2* of brain tissue), and these changes can be advantageous or not, depending on the image method used (van der Zwaag et al., 2016). Nevertheless, producing a high quality image is then challenging with UHF. For example, the field uniformity from both the static (B_0) and the transmit (B_1^+) is often compromised, as well the increase in specific absorption rate (SAR). Specifically, the transmit and receive radiofrequency field inhomogeneities also affects the traditional T1-weighted image acquired with a Magnetic Prepared Rapid Gradient Echo (MPRAGE) sequence to the extent that the inversion efficiency of an adiabatic pulse may also be affected, especially in the cerebellum and temporal lobes (O'Brien et al., 2014b).

To obtain a more homogeneous contrast, it is necessary to provide an effective inversion, independent of $B1^+$ inhomogeneities (Marques and Norris, 2018; O'Brien et al., 2014b). The B1 uniformity can be achieved using either more homogeneous adiabatic pulses such as a flattened hyperbolic secant pulse (HS8) (Garwood and DelaBarre, 2001) or time resampled frequency offset compensated inversion (TR-FOCI) pulse (Hurley et al., 2010), which promises a higher B1 uniformity or using dielectric pads (van Gemert et al., 2019). A further and more sophisticated alternative is the use of special pulse design for both the inversion and excitation pulses on parallel transmission systems (pTx or Multix system), like Universal Pulses (Gras et al., 2017b), in which the required prescans can be avoided.

Parallel transmit system and universal pulses

At Ultra-high field (B0) strengths, the wavelength of the fields generated by the transmit coil elements inside the object becomes equal to or smaller than its diameter (Ibrahim et al., 2001). As a result, constructive and destructive interferences occur, leading to an inhomogeneous B1 distribution with alternating bright and dark regions across the sample. Moreover, when a subject is inserted inside the magnet, tissue dielectric properties distort the B1 profile (Ibrahim et al., 2001; Padormo et al., 2016).

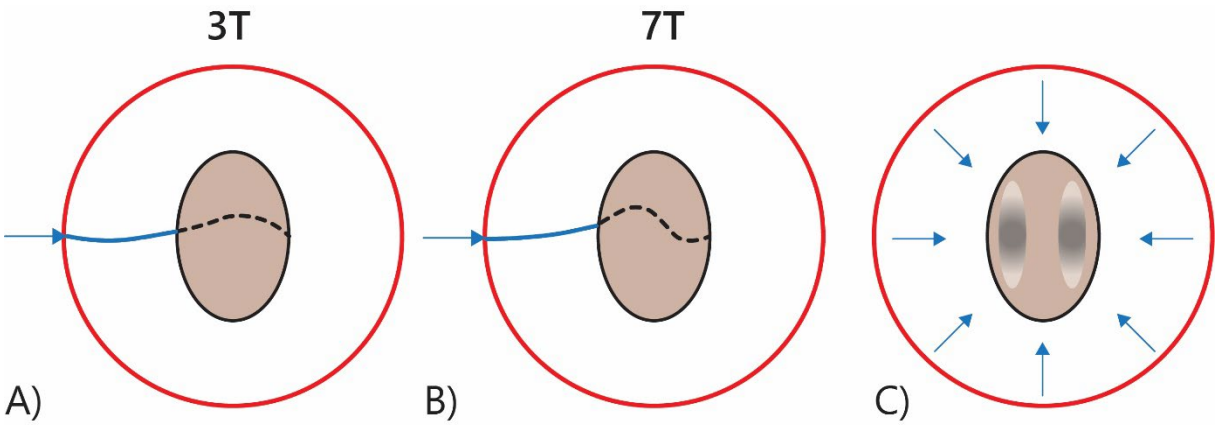

Fig1. Schematic representation shows the RF field's interferences when moving from 3T to 7T. A) At 3T, relatively little interference. B) At 7T, a higher degree of interference occurs because the wavelength of the field is equal to or smaller than the object's diameter. C) The increased wave interference manifests itself in areas of low transmit efficiency. (Figure adapted from https://www.lumc.nl/org/radiologie/research/gortercenter/DielectricPads/)

As mentioned before, a more recent and sophisticated alternative to improve contrast homogeneity is using multiple transmission channels, also known as parallel transmission (so-called pTx or Multix systems). The idea is relatively simple, instead of a single RF coil transmitting a single B1 field, multiple element arrays are individually controlled to generate their own B1 subfields. The sum of these subfields constitutes the net B1 experienced by the tissue. The magnitude and phase of each element can be optimized such that the most homogeneous B1 distribution is produced. In addition to controlling their amplitudes and phases (RF shimming), the individual array elements can also run different RF waveforms.

There are several pTx pulse design approaches (see Deniz 2019 for a thorough review); nevertheless, in general, the optimization of the transmit field relies on calibration

measurements performed before scanning the participants. Thus, two issues usually compromise the workflow of the calibration. First, it requires expertise to calculate the waveforms, and second, the pre-acquisition images ($B1^+$maps for each array element and B0 distribution) might take up to 10 to 15 minutes to be acquired and post-processed, including the data transfer, analysis, and pulse design. These issues prevent more effective use of this technology in routine clinical and neuroscience applications (Deniz, 2019). Aiming to solve this issue, broadly-calibrated plug-and-play pulses were developed (Gras et al., 2017b) for inversion and excitation (Gras et al., 2017a). The so-called universal pulses have proven to be a highly effective pTx solution not only for its calibration-free characteristic but also because it shows that it is possible to mitigate the inhomogeneity problem accurately on several different applications (Gras et al., 2019b, 2019a, 2018; Le Ster et al., 2019). The universal pTx solution is also relatively simple, it relies on the calculation of individual performance (B1+ and B0) of a group of participants, and the solution is the average of this group.

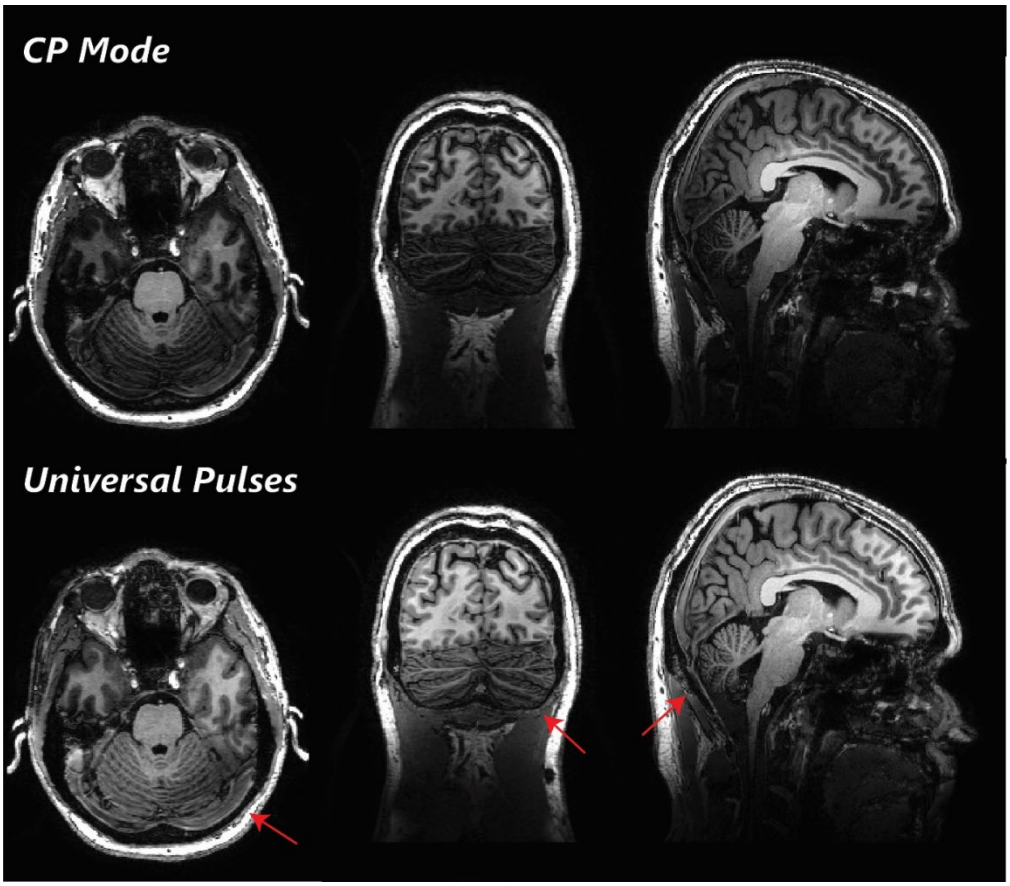

Fig.2. T1-weighted MPRAGE illustrates the differences between Universal Pulses versus CP mode. A signal increase is seen in cerebellar and temporal areas after applying the universal pulse (red arrows).

Functional MRI

One of the most exciting discoveries in the NMR field is functional MRI (fMRI). fMRI was first demonstrated in 1990 by Seiji Ogawa (Ogawa et al., 1990). He observed the MRI signal changes in brain regions depending on their oxy- and deoxyhemoglobin concentrations. When brain neurons are activated, the oxygen consumption required to active brain regions leads to measurable variations in the MRI signal. This concept was further used to map brain regions responding to various stimulations.

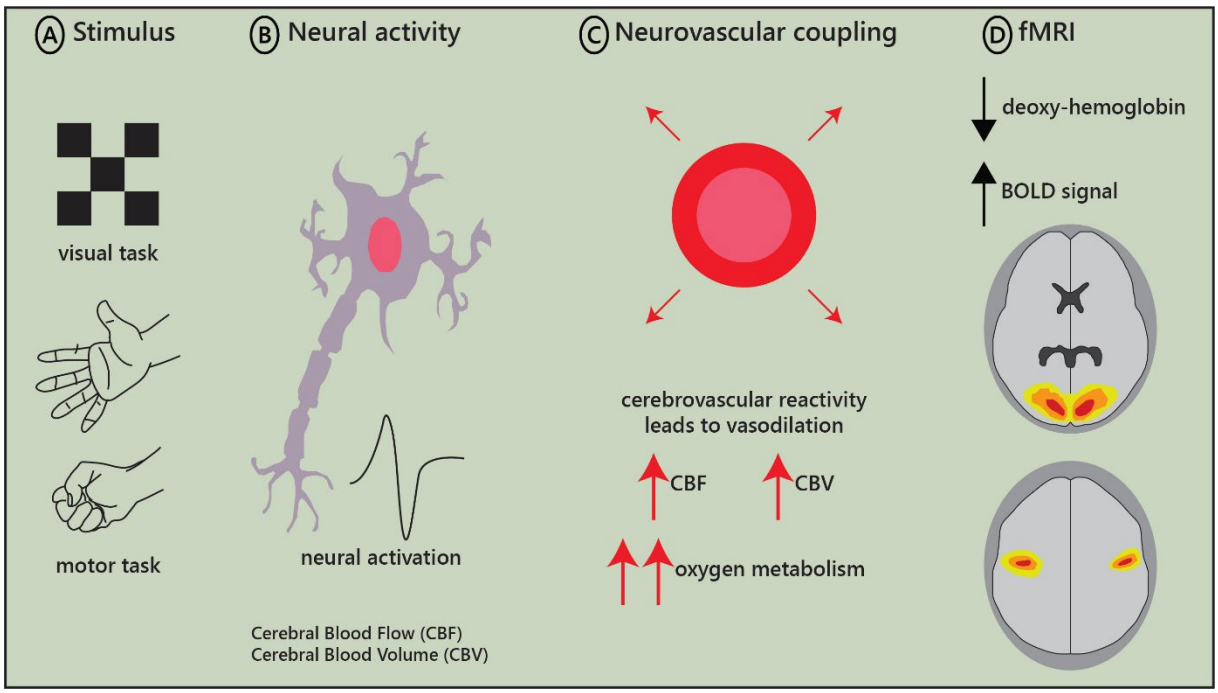

Fig.3. Illustration of the blood oxygenation level-dependent (BOLD) mechanism showing the transformation from stimulus to BOLD response. The BOLD signal reflects changes in deoxyhemoglobin driven by localized changes in brain blood flow and blood oxygenation, coupled to underlying neuronal activity by neurovascular coupling. The event starts in A) with stimulation, which can be a flickering checkerboard (visual task) or a hand movement task (motor task). The stimulus will induce an increase in neural activation B), which will trigger the neurovascular coupling C). The increase in neuronal activity induces vasodilatation, resulting in a significant increase in local cerebral blood flow (CBF) and increased cerebral blood volume (CBV). This process brings more oxygenated blood and thus washout the deoxyhemoglobin, resulting in a more homogeneous magnetic field in which the transverse magnetization occurs more slowly, and the BOLD fMRI signal increases D).

Thirty years later, fMRI is currently the mainstay of neuroimaging in neuroscience (Logothetis, 2008; Turner, 2016). Advances in scanner technology, image acquisition, and analysis improve the fMRI application in 7T (Ladd et al., 2018; Marques and Norris, 2018), with a significant increase in the number of publications in the past few years (van der Zwaag et al., 2016). As mentioned before, the UHF (≥ 7T) scanner's advantage is the increase in signal-to-noise ratio (SNR) which enables higher image quality and resolution also for fMRI applications (Pohmann et al., 2016; Setsompop et al., 2016). Additionally, UHF strengths enhance the magnetic susceptibility contrast, as is the case of the blood oxygenation level-dependent (BOLD) contrast, the most common contrast used for fMRI (van der Zwaag et al., 2009).

The higher BOLD sensitivity (fCNR, functional contrast-to-noise ratio) achieved at UHF has enabled studies of fine-scale functional architecture, such as cortical columns, layers, and subcortical nuclei (Dumoulin et al., 2017; Norris and Polimeni, 2019; Viessmann and Polimeni, 2021) and also increases the statistical power needed for single-subject analysis (Cai et al., 2021; Viessmann and Polimeni, 2021).

The gradient-echo EPI (GRE-EPI) is the typical method of choice for fMRI applications (Glover, 2011). Despite its high sensitivity to deoxyhemoglobin variations and widespread availability, the gradient-echo (GRE) BOLD signal is predominantly driven by the large draining vessels resulting in a biased measurement towards the superficial cortical layers. The increased sensitivity achieved with UHF can also be traded for specificity either by using Spin Echo based T2 contrast (Kemper et al., 2015; Siero et al., 2013) (EPI or GRASE readout) or by measuring different contrast mechanisms like cerebral blood flow (CBF) with Arterial Spin Labeling (Kashyap et al., 2021) (ASL) or cerebral blood volume (CBV) with Vascular Space Occupancy (VASO) (Huber et al., 2017) techniques.

Throughout the present thesis, we will explore and further investigate the advantages of the VASO fMRI sequence. Vascular space occupancy (VASO) is an fMRI alternative based on changes in CBV (Lu et al., 2013, 2003). The VASO sequence and its variants take advantage of the T1 differences between arterial blood and the surrounding tissue to null the blood signal and measure CBV changes (Lu et al., 2003). An inversion recovery pulse minimizes blood signals while a substantial part of the tissue signal remains available for detection. The increased cerebral blood volume results in a negative signal change during the neuronal activity, caused by the tissue signal reduction in the voxel. VASO-CBV contrast promises higher microvascular

specificity since it is sensitive to arteriole and post-arterial CBV changes, resulting in better spatial localization of the neuronal activity with reduced draining vein contamination than BOLD (Huber et al., 2014; Jin and Kim, 2008).

AIM

The overall aim of the present thesis is to investigate and develop advanced MRI techniques for UHF, targeting neuroscience applications. In ***chapter 2***, I first examined the universal pulses capabilities in combination with a more adiabatic inversion pulse (TR-FOCI) to mitigate the Ultra-high field (UHF) inhomogeneity problem, evaluating if the contrast enhancement of the T1-weighted image obtained with MPRAGE sequence could be comparable to the T1-weighted image obtained with the self-bias field corrected MP2RAGE sequence. For the approach outlined in ***chapters 3-5***, I explored the VASO-CBV specificity advantage targeting three different questions. First, in **chapter 3**, I hypothesized that the vascular source would explain part of the fMRI nonlinearity effect. Thus, the VASO-CBV signal would elicit a different response than BOLD regarding the movement rate. Similarly, in **chapter 5**, I hypothesized that the vascular component of the pRF size estimate would yield a smaller pRF size for the VASO-CBV. Nevertheless, for **chapter 4,** I hypothesized that the higher specificity of VASO-CBV would yield higher selectivity than BOLD.

Thesis outline

In **Chapter 2**, I propose a strategy to improve B1+ homogeneities on the T1-weighted MPRAGE sequence in direct comparison to the MP2RAGE. The strategy consisted of combining the adiabatic TR-FOCI pulse to invert the signal uniformly with the kt-point Universal Pulses approach for homogeneous excitation. In addition, to improve the scan time, the k-space shutter technique was employed.

In **Chapter 3,** I implement the Slab Selective Slab Inversion (SS-SI) VASO sequence to investigate the linearity of the VASO-CBV responses using a hand movement task. As the VASO-CBV and BOLD contrast are thought to have distinct weighting for microvascular compartments, a distinct response behavior with respect to an increased movement rate was anticipated. Thus, a comparison between BOLD and VASO-CBV was performed with respect to the hand movement rate in the motor cortex.

In **Chapter 4**, I investigate the cortical activation with sub-millimeter BOLD and VASO fMRI during individual finger movement in healthy participants using response selectivity measurements. I hypothesized that the assumed higher specificity of VASO-CBV imaging would translate to reduced overlap in fine-scale digit representation maps compared to BOLD-based digit maps.

In **Chapter 5**, to investigate how VASO-CBV compares to BOLD fMRI for cognitive neuroscience applications. I compared population receptive field (pRF) mapping estimates between VASO-CBV and BOLD. Because pRF size estimates also depend on the vascular sources, I hypothesized that VASO-CBV would elicit distinct pRF properties compared to BOLD.

Reference

Cai, Y., Hofstetter, S., van der Zwaag, W., Zuiderbaan, W., Dumoulin, S.O., 2021. Individualized cognitive neuroscience needs 7T: Comparing numerosity maps at 3T and 7T MRI. Neuroimage 237, 118184. https://doi.org/10.1016/j.neuroimage.2021.118184

Deniz, C.M., 2019. Parallel Transmission for Ultrahigh Field MRI. Top. Magn. Reson. Imaging 28, 159–171. https://doi.org/10.1097/RMR.0000000000000204

Dumoulin, S.O., Fracasso, A., van der Zwaag, W., Siero, J.C.W., Petridou, N., 2017. Ultra-high field MRI: Advancing systems neuroscience towards mesoscopic human brain function. Neuroimage 0–1. https://doi.org/10.1016/j.neuroimage.2017.01.028

Fracasso, A., Van Veluw, S.J., Visser, F., Luijten, P.R., Spliet, W., Zwanenburg, J.J.M., Dumoulin, S.O., Petridou, N., 2016. Lines of Baillarger in vivo and ex vivo: Myelin contrast across lamina at 7 T MRI and histology. Neuroimage 133, 163–175. https://doi.org/10.1016/j.neuroimage.2016.02.072

Garwood, M., DelaBarre, L., 2001. The Return of the Frequency Sweep: Designing Adiabatic Pulses for Contemporary NMR. J. Magn. Reson. 153, 155–177. https://doi.org/10.1006/jmre.2001.2340

Glover, G.H., 2011. Overview of Functional Magnetic Resonance Imaging. Neurosurg. Clin. N. Am. 22, 133–139. https://doi.org/10.1016/j.nec.2010.11.001

Gras, V., Boland, M., Vignaud, A., Ferrand, G., Amadon, A., Mauconduit, F., Le Bihan, D., Stöcker, T., Boulant, N., 2017a. Homogeneous non-selective and slice-selective parallel-transmit excitations at 7 Tesla with universal pulses: A validation study on two commercial RF coils. PLoS One 12, 1–16. https://doi.org/10.1371/journal.pone.0183562

Gras, V., Vignaud, A., Amadon, A., Le Bihan, D., Boulant, N., Bihan, D. Le, Boulant, N., Le Bihan, D., Boulant, N., 2017b. Universal pulses: A new concept for calibration-free parallel transmission. Magn. Reson. Med. 77, 635–643. https://doi.org/10.1002/mrm.26148

Gulban, O.F., Schneider, M., Marquardt, I., Haast, R.A.M., De Martino, F., 2018. A scalable method to improve gray matter segmentation at ultra high field MRI, PLoS ONE. https://doi.org/10.1371/journal.pone.0198335

Huber, L., Handwerker, D.A., Jangraw, D.C., Chen, G., Hall, A., Stüber, C., Gonzalez-Castillo, J., Ivanov, D., Marrett, S., Guidi, M., Goense, J., Poser, B.A., Bandettini, P.A., 2017. High-Resolution CBV-fMRI Allows Mapping of Laminar Activity and Connectivity of Cortical Input and Output in Human M1. Neuron 96, 1253-1263.e7. https://doi.org/10.1016/j.neuron.2017.11.005

Huber, L., Ivanov, D., Krieger, S.N., Streicher, M.N., Mildner, T., Poser, B.A., Möller, H.E., Turner, R., 2014. Slab-selective, BOLD-corrected VASO at 7 tesla provides measures of cerebral blood volume reactivity with high signal-to-noise ratio. Magn. Reson. Med. 72, 137–148. https://doi.org/10.1002/mrm.24916

Hurley, A.C., Al-radaideh, A., Bai, L., Aickelin, U., Coxon, R., Glover, P., Gowland, P.A., 2010. Tailored RF pulse for magnetization inversion at ultrahigh field. Magn. Reson. Med. 63, 51–58. https://doi.org/10.1002/mrm.22167

Ibrahim, T.S., Lee, R., Abduljalil, A.M., Baertlein, B.A., Robitaille, P.-M.L., 2001. Dielectric resonances and B1 field inhomogeneity in UHFMRI: computational analysis and experimental findings. Magn. Reson. Imaging 19, 219–226. https://doi.org/10.1016/S0730-725X(01)00300-9

Jin, T., Kim, S.-G., 2008. Cortical layer-dependent dynamic blood oxygenation, cerebral blood flow and cerebral blood volume responses during visual stimulation. Neuroimage 43, 1–9. https://doi.org/10.1016/j.neuroimage.2008.06.029

Kashya, S., Ivanov, D., Havlicek, M., Poser, B.A., Uluda, K., Kashyap, S., Ivanov, D., Havlicek, M., Sengupta, S., Poser, B.A., Uludağ, K., 2018. Resolving laminar activation in human V1 using ultra-high spatial resolution fMRI at 7T. Sci. Rep. 8, 1–11. https://doi.org/10.1038/s41598-018-35333-3

Kashyap, S., Ivanov, D., Havlicek, M., Huber, L., Poser, B.A., Uludağ, K., 2021. Sub-millimetre resolution laminar fMRI using Arterial Spin Labelling in humans at 7 T. PLoS One 16, e0250504. https://doi.org/10.1371/journal.pone.0250504

Kemper, V.G., De Martino, F., Vu, A.T., Poser, B.A., Feinberg, D.A., Goebel, R., Yacoub, E., 2015. Sub-millimeter T<inf>2</inf> weighted fMRI at 7 T: Comparison of 3D-GRASE and 2D SE-EPI. Front. Neurosci. 9, 1–14. https://doi.org/10.3389/fnins.2015.00163

Ladd, M.E., Bachert, P., Meyerspeer, M., Moser, E., Nagel, A.M., Norris, D.G., Schmitter, S., Speck, O., Straub, S., Zaiss, M., 2018. Pros and cons of ultra-high-field MRI/MRS for human application. Prog. Nucl. Magn. Reson. Spectrosc. 109, 1–50. https://doi.org/10.1016/j.pnmrs.2018.06.001

Ledig, C., Schuh, A., Guerrero, R., Heckemann, R.A., Rueckert, D., 2018. Structural brain imaging in Alzheimer's disease and mild cognitive impairment: biomarker analysis and shared morphometry database. Sci. Rep. 8, 1–16. https://doi.org/10.1038/s41598-018-29295-9

Logothetis, N.K., 2008. What we can do and what we cannot do with fMRI. Nature 453, 869–878. https://doi.org/10.1038/nature06976

Lu, H., Golay, X., Pekar, J.J., Zijl, P.C.M. Van, 2003. Functional Magnetic Resonance Imaging Based on Changes in Vascular Space Occupancy 274, 263–274. https://doi.org/10.1002/mrm.10519

Lu, H., Hua, J., van Zijl, P.C.M.M., 2013. Noninvasive functional imaging of cerebral blood volume with vascular-space-occupancy (VASO) MRI. NMR Biomed. 26, 932–948. https://doi.org/10.1002/nbm.2905

MacDonald, M.E., Frayne, R., 2015. Cerebrovascular MRI: a review of state-of-the-art approaches, methods and techniques. NMR Biomed. 28, 767–791. https://doi.org/10.1002/nbm.3322

Marques, J.P., Norris, D.G., 2018. How to choose the right MR sequence for your research question at 7 T and above? Neuroimage 168, 119–140. https://doi.org/10.1016/j.neuroimage.2017.04.044

Meijer, F.J.A., Goraj, B., Bloem, B.R., Esselink, R.A.J., 2017. How i do it: Clinical application of brain mri in the diagnostic work-up of parkinsonism. J. Parkinsons. Dis. 7, 211–217. https://doi.org/10.3233/JPD-150733

Norris, D.G., Polimeni, J.R., 2019. Laminar (f)MRI: A short history and future prospects. Neuroimage. https://doi.org/10.1016/j.neuroimage.2019.04.082

O'Brien, K.R., Kober, T., Hagmann, P., Maeder, P., Marques, J., Lazeyras, F., Krueger, G., Roche,

A., Brien, K.R.O., Kober, T., Hagmann, P., Maeder, P., Lazeyras, F., Krueger, G., Roche, A., 2014a. Robust T1-weighted structural brain imaging and morphometry at 7T using MP2RAGE. PLoS One 9. https://doi.org/10.1371/journal.pone.0099676

O'Brien, K.R., Magill, A.W., Delacoste, J., Marques, J.P., Kober, T., Fautz, H., Lazeyras, F., Krueger, G., 2014b. Dielectric pads and low- B1+ adiabatic pulses: Complementary techniques to optimize structural T 1 w whole-brain MP2RAGE scans at 7 tesla. J. Magn. Reson. Imaging 40, 804–812. https://doi.org/10.1002/jmri.24435

Ogawa, S., Lee, T.M., Kay, A.R., Tank, D.W., 1990. Brain magnetic resonance imaging with contrast dependent on blood oxygenation. Proc. Natl. Acad. Sci. U. S. A. 87, 9868–72. https://doi.org/10.1073/pnas.87.24.9868

Padormo, F., Beqiri, A., Hajnal, J. V., Malik, S.J., 2016. Parallel transmission for ultrahigh-field imaging. NMR Biomed. 29, 1145–1161. https://doi.org/10.1002/nbm.3313

Pohmann, R., Speck, O., Scheffler, K., 2016. Signal-to-noise ratio and MR tissue parameters in human brain imaging at 3, 7, and 9.4 tesla using current receive coil arrays. Magn. Reson. Med. 75, 801–809. https://doi.org/10.1002/mrm.25677

Rüber, T., David, B., Elger, C.E., 2018. MRI in epilepsy. Curr. Opin. Neurol. 31, 223–231. https://doi.org/10.1097/WCO.0000000000000539

Setsompop, K., Feinberg, D.A., Polimeni, J.R., 2016. Rapid brain MRI acquisition techniques at ultra-high fields. NMR Biomed. 29, 1198–1221. https://doi.org/10.1002/nbm.3478

Siero, J.C.W., Ramsey, N.F., Hoogduin, H., Klomp, D.W.J., Luijten, P.R., Petridou, N., 2013. BOLD Specificity and Dynamics Evaluated in Humans at 7 T: Comparing Gradient-Echo and Spin-Echo Hemodynamic Responses. PLoS One 8, 1–8. https://doi.org/10.1371/journal.pone.0054560

Turner, R., 2016. Uses, misuses, new uses and fundamental limitations of magnetic resonance imaging in cognitive science. Philos. Trans. R. Soc. B Biol. Sci. 371, 20150349. https://doi.org/10.1098/rstb.2015.0349

van der Zwaag, W., Francis, S., Head, K., Peters, A., Gowland, P., Morris, P., Bowtell, R., 2009. fMRI at 1.5, 3 and 7 T: Characterising BOLD signal changes. Neuroimage 47, 1425–1434.

https://doi.org/10.1016/j.neuroimage.2009.05.015

van der Zwaag, W., Schäfer, A., Marques, J.P., Turner, R., Trampel, R., 2016. Recent applications of UHF-MRI in the study of human brain function and structure: a review. NMR Biomed. 29, 1274–1288. https://doi.org/10.1002/nbm.3275

van Gemert, J., Brink, W., Webb, A., Remis, R., 2019. High-permittivity pad design tool for 7T neuroimaging and 3T body imaging. Magn. Reson. Med. 81, 3370–3378. https://doi.org/10.1002/mrm.27629

Viessmann, O., Polimeni, J.R., 2021. High-resolution fMRI at 7 Tesla: challenges, promises and recent developments for individual-focused fMRI studies. Curr. Opin. Behav. Sci. 40, 96–104. https://doi.org/10.1016/j.cobeha.2021.01.011

Wiggins, C.J., Schäfer, A., Dhital, B., Le Bihan, D., Turner, R., 2017. After over 200 years, 7T magnetic resonance imaging reveals the foliate structure of the human corpus callosum in vivo. Br. J. Radiol. 90, 1–9. https://doi.org/10.1259/bjr.20160906

Chapter 2

Can 7T MPRAGE match MP2RAGE for gray-white matter contrast?

Ícaro A.F de Oliveira,

Thomas Roos,

Serge O. Dumoulin,

Jeroen C.W. Siero,

Wietske van der Zwaag

Based on the publication: Oliveira, Í.A.F., Roos, T., Dumoulin, S.O., Siero, J.C.W., van der Zwaag, W., 2021. Can 7T MPRAGE match MP2RAGE for gray-white matter contrast? Neuroimage 240, 118384. https://doi.org/10.1016/j.neuroimage.2021.118384

Abstract

Ultra-high field (UHF) MRI provides a significant increase in signal-to-noise ratio (SNR) and gains in contrast weighting in several functional and structural acquisitions. Unfortunately, an increase in field strength also induces non-uniformities in the transmit field (B1+) that can compromise image contrast nonuniformly. The MPRAGE is one of the most common T1 weighted (T1w) image acquisitions for structural imaging. It provides excellent contrast between gray and white matter and is widely used for brain segmentation. At 7T, the signal non-uniformities tend to complicate this and therefore, the self-bias-field corrected MP2RAGE is often used there. In both MPRAGE and MP2RAGE, more homogeneous image contrast can be achieved with adiabatic pulses, like the TR-FOCI inversion pulse, or special pulse design on parallel transmission systems, like Universal Pulses (UP). In the present study, we investigate different strategies to improve the bias-field for MPRAGE at 7T, comparing the contrast and GM/WM segmentability against MP2RAGE. The higher temporal efficiency of MPRAGE combined with the potential of the user-friendly UPs was the primary motivation for this MPRAGE-MP2RAGE comparison. We acquired MPRAGE data in six volunteers, adding a k-space shutter to reduce scan time, a kt-point UP approach for homogeneous signal excitation, and a TR-FOCI pulse for homogeneous inversion. Our results show remarkable signal contrast improvement throughout the brain, including regions of low $B1^+$ such as the cerebellum. The improvements in the MPRAGE were largest following the introduction of the UPs. In addition to the CNR, both SNR and GM/WM segmentability were also assessed. Among the MPRAGEs, the combined strategy (UP + TR-FOCI) yielded highest SNR and showed highest spatial similarity between GM segments to the MP2RAGE. Interestingly, the distance between gray and white matter peaks in the intensity histograms did not increase, as better pulses and higher SNR especially benefitted the (cerebellar) gray matter. Overall, the gray-white matter contrast from MP2RAGE is higher, with higher CNR and higher intensity peak distances, even when scaled to scan time. Hence, the extra acquisition time for MP2RAGE is justified by the improved segmentability.

High-quality anatomical T1w images are essential for several MRI applications, notably to serve as an anatomical reference in fMRI and Gray Matter segmentation (Marques and Norris, 2018). Typically, 3D T1 weighted images are acquired with the Magnetization Prepared Rapid Gradient Echo (MPRAGE) sequence (Mugler and Brookeman, 1991, 1990). A 3D Gradient Echo (GRE) train is applied with short repetition times (TRs) and small flip angles (close to the Ernst angle), with the level of T1 weighting being predominantly controlled by the inversion time and the inversion efficiency of the applied inversion pulse (Mugler and Brookeman, 1991).

Anatomical, T1-weighted Magnetic Resonance Imaging (MRI) can benefit substantially from the use of Ultra-High Field (UHF, ≥ 7T). Compared to conventional, clinical, field strengths, imaging at 7T offers higher signal-to-noise ratio (SNR), which can be traded for an increased spatial resolution to reduce partial volume effects and more precise cortical measurements. Although T1 relaxation times at 7T are longer for both GM and WM, the difference is sufficient to result in significant gains in tissue contrast for structural MRI (Rooney et al., 2007; Wright et al., 2008). While there are benefits at ultra-high field (UHF), traditional MPRAGE data are also affected by transmit (B1+) and receive (B1-) radiofrequency field inhomogeneities. In addition, large static (B0) field variations in brain areas close to air-tissue boundaries also affect the inversion efficiency.

Hence, some measures have to be taken to make MPRAGE images B1+ insensitive at 7T. Several possibilities exist. A widely used approach is that of the adiabatic pulses for inversion. These adiabatic pulses have lower or no dependency on B1+. Examples of adiabatic pulses are the flattened hyperbolic secant pulse (HS8) (Garwood and DelaBarre, 2001), and time resampled frequency offset compensated inversion (TR-FOCI) pulse (Hurley et al., 2010). This is not sufficient to completely remove all B1+ contamination as it only improves the inversion homogeneity; the excitation homogeneity is still affected by B1+ variation.

In the MP2RAGE sequence (Marques et al., 2010), two 3D GRE trains are acquired at different inversion times (TI), producing a T1w, and an approximately proton density (PD) weighted image. The combination of both images results in a T1w and a T1 map, ideally both free of $B1^-$, PD and T2* contrast (Marques et al., 2010; Van de Moortele et al., 2009). Even in an MP2RAGE acquisition, very low local B1+ can cause a loss of SNR and contrast, usually in the cerebellum and temporal lobes (O'Brien et al., 2014b). If not adequately addressed, these non-uniformities can compromise the image quality, or even provide incorrect segmentation,

inappropriate diagnostic or poor co-registration (Haast et al., 2018; O'Brien et al., 2014a, 2014b). Also, in the MP2RAGE, more homogeneous contrast can be achieved by applying better and more efficient adiabatic inversion pulses (O'Brien et al., 2014b). Previous studies showed that image contrast uniformity from TR-FOCI is higher compared to HS8 (Hurley et al., 2010; O'Brien et al., 2014b).

A third alternative to improve contrast homogeneity is using multiple transmission channels, also known as parallel transmission (so-called pTx or Multix systems) (Padormo et al., 2016). Parallel transmission systems enable local decreases or compensation in B1+ inhomogeneity using multiple transmit RF coils which are independently driven and operating simultaneously (Deniz, 2019). Typically, pTx pulse design relies on calibration measurements performed before scanning subjects, which takes up valuable scan time. To address this issue, broadly-calibrated plug-and-play pulses were developed (Gras et al., 2017) for both inversion and excitation. This Universal Pulses approach involves first collecting the B1+ field information for several subjects, followed by calculating their optimal set of parameters. The resulting pulses are therefore computed to account for the average variations in B1+ field. Successful implementation in a variety of sequences has been demonstrated, including 3D T1 weighted MPRAGE (Gras et al., 2017), T2-weighted TSE, (Gras et al., 2018), fluid-attenuated inversion recovery (FLAIR) (Gras et al., 2019b), multi-band and 3D EPI for whole-brain fMRI (Gras et al., 2019a; Le Ster et al., 2019) and T2* weighted 2D Gradient echo (Gras et al., 2017).

Regarding temporal efficiency, high resolution isotropic T1w MPRAGE can be acquired in 5-7 minutes, whereas a T1w MP2RAGE with the same spatial resolution usually requires 10-14 minutes, in both cases using a two-dimensional (ky-kz) undersampling pattern with parallel imaging reconstruction. Various strategies have been employed to reduce scan time in both acquisitions. The most common approach is to skip and zero-fill parts of the k-space, whether applying partial Fourier or elliptical sampling schemes (k-space shutter).

The differences between both MPRAGE-like sequences has been studied before, although mainly for morphometric assessment (Fujimoto et al., 2014; Okubo et al., 2016; Seiger et al., 2015; Yan et al., 2020). To our knowledge, the influence of different bias-field correction strategies, specifically using UPs for whole-brain MPRAGE compared to MP2RAGE, has not been reported yet. Therefore, the present study compares different strategies to improve the homogeneity of contrast in whole-brain MPRAGE images. This comparison is motivated by

higher temporal efficiency of MPRAGE, combined with the great potential of UPs to make UHF more accessible. To acquire the best possible MPRAGE on a 7T scanner we acquired T1-weighted images with (1) a k-space shutter to reduce scan time; (2) Universal kt-point pulses to homogenize signal excitation and (3) a TR-FOCI to invert the signal uniformly. We expected that the combination of all advanced techniques would improve image SNR and CNR and improve the segmentation results. The MPRAGE data were compared to MP2RAGE data, which were acquired with a k-space shutter and a standard HS8 inversion pulse or a TR-FOCI.

Methods

Subjects

Six healthy volunteers (age 25-40 years, three women) participated in the present study. The local ethics committee approved the study, and all volunteers provided written consent after being informed of the experimental procedures.

MRI Sequences

All imaging measurements were performed on a 7T MRI scanner (Philips Healthcare, Best, The Netherlands) using an 8-channel transmit, 32-channel receive head coil (32Rx8Tx , Nova Medical Inc, Wilmington, United States) with a close to circularly polarized-mode achieved by B1-shimming over the entire brain of a separate group of volunteers.

The whole-brain T1-weighted MPRAGEs and MP2RAGEs were acquired within the same session with matched voxel sizes and acceleration factors for all six sequences to ensure a fair comparison between all sequences. The common set of parameters for both techniques were: matrix size = 288×288×232, Field of View (FOV) = 230×230×186mm^3, with isotropic voxel-size of 0.8 mm, with SENSE undersampling factor in two directions (Left-Right and Anterior-Posterior), 2D SENSE = 1.8(LR)×1.8(AP), a slice oversampling of 20% and sagittal orientation. All the MPRAGEs shared the same TR/TE= 12/3.3 ms, TI = 1000 ms, TR_{volume}=3000 ms, FA = 8° and $BW_{readout}$ = 235.2 Hz. This protocol was based on the ADNI T1-weighted anatomical (http://adni.loni.usc.edu/), albeit with longer TR to accommodate the longer T1 at 7T. For the MP2RAGE, Bloch simulations were used to optimize the inversion times, TR_{volume} and flip angles following (Marques et al., 2010), resulting in a TR/TE = 6.2/2.3 ms, TI_1 = 800 ms and TI_2 = 2700

ms, TR_{volume} = 5500 ms , FA = 7°/5° and $BW_{readout}$ = 401.9 Hz. The length of a readout block for the MPRAGE is 1996 ms and for the MP2RAGE 1016 ms. The total scan duration and the specific parameters for the individual scans are given in Table 1.

Table 1: Acquisition parameters for MPRAGE and MP2RAGE acquisitions.

Parameters	*MPRAGE1*	*MPRAGE2*	*MPRAGE3*	*MPRAGE4*	*MP2RAGE5*	*MP2RAGE6*
TR/TE (ms)	12/3.3	12/3.3	12/3.3	12/3.3	6.2/2.3	6.2/2.3
FA (degree)	8	8	8	8	7/5	7/5
TI_1/TI_2 (ms)	1000	1000	1000	1000	800/2700	800/2700
Inversion Pulse	HS8	HS8	HS8	TR-FOCI	HS8	TR-FOCI
k-space shutter		YES	YES	YES	YES	YES
Readout lines	159	164	164	164	164	164
Universal Pulses			YES	YES		
TR_{volume} (ms)	3000	3000	3000	3000	5500	5500
Duration (s)	467	350	350	350	638	638

Duration refers to the total scan duration

The standard MPRAGE was defined with an HS8 inversion pulse, standard excitation pulse (no UPs), a fully sampled matrix (without the k-space shutter), and called MPRAGE1. The 159 readout lines correspond to a single plane in k-space for MPRAGE1. For all other scans, a vendor-supplied elliptical k-space shutter was added. With the k-space shutter the edges of the k-space are skipped in an ellipsoidal fashion, reducing scan time by ~25%. A similar number of lines per gradient echoes (GRE) readout block was used (164) as for the MPRAGE1 (159). For MPRAGE3 the standard excitation pulses were additionally replaced by the UPs. For the UPs, the kt-point method (Cloos et al., 2012) was used to generate the appropriate pulse shapes. A small tip angle pulse with 1ms of duration with five kt-points was designed on 16 subjects with an interleaved greedy-local optimization (Grissom et al., 2012) as in (Roos et al., 2019). And finally, for MPRAGE4 the HS8 adiabatic inversion pulse was replaced by the TR-FOCI pulse, with

an amplitude adjusted to have a minimum of 15μT and inversion pulse duration of 13ms. The MP2RAGEs were acquired with the standard HS8 and with a TR-FOCI. Both MP2RAGEs were acquired solely with k-space shutter and standard excitation pulses, to keep the scan session reasonably short. The vendor-supplied bias-field removal correction CLEAR (Constant Level Appearance) (Harvey et al., 2015) was used for both MPRAGE and MP2RAGE data, though this is cancelled out again in the MP2RAGE T1-weighted images.

MP2RAGE reconstruction

In the MP2RAGE sequence, after the simultaneous acquisition of the first inversion (GRE_{TI1}) and the second inversion (GRE_{TI2}), a uniform T1-weighted image is obtained by computing the real component of the normalized complex ratio from both volumes (Marques et al., 2010), where GRE^*_{TI1} stands for the complex conjugate of GRE_{TI1}. Once the T1-weighted image was generated, a background noise removal was applied using LaYNii toolbox (Huber et al., 2021).

$$S = \frac{Re(GRE^*_{TI1} GRE_{TI2})}{|GRE_{TI1}|^2 + |GRE_{TI2}|^2} \qquad [1]$$

Registration and Segmentation

All T1w data were registered to the MPRAGE1 space using the six degrees of freedom rigid body co-registration of SPM12 (www.fil.ion.ucl.ac.uk/spm/software/spm12/) to allow further comparisons. Segmentation of gray matter (GM), white matter (WM), and cerebrospinal fluid (CSF) were performed for each subject separately using the computational anatomy toolbox CAT12 (www.neuro.uni-jena.de/cat/) for SPM with bias field correction in medium level (0.5). The segmentation procedures resulted in 6 different GM and WM segmentation volumes, which were combined, resulting in a single GM and WM combined ROI for each subject and later used to define the regions of interest's (ROI's). Voxels were assigned GM if they were GM in at least two datasets, the same approach was used for the WM, and overlapping voxels were excluded from the final combined ROI. A cerebellum mask was created using the Nighres brain region extraction function (Huntenburg et al., 2018) and further separated into GM and WM cerebellum masks using the GM and WM mask from the unified segmentation. Another two

cubic ROIs (50×50×50 mm) in the right temporal lobe and centred on the PCC (Posterior Cingulate Cortex) were assessed as additional examples of low (temporal) and high (PCC)-B1+ areas.

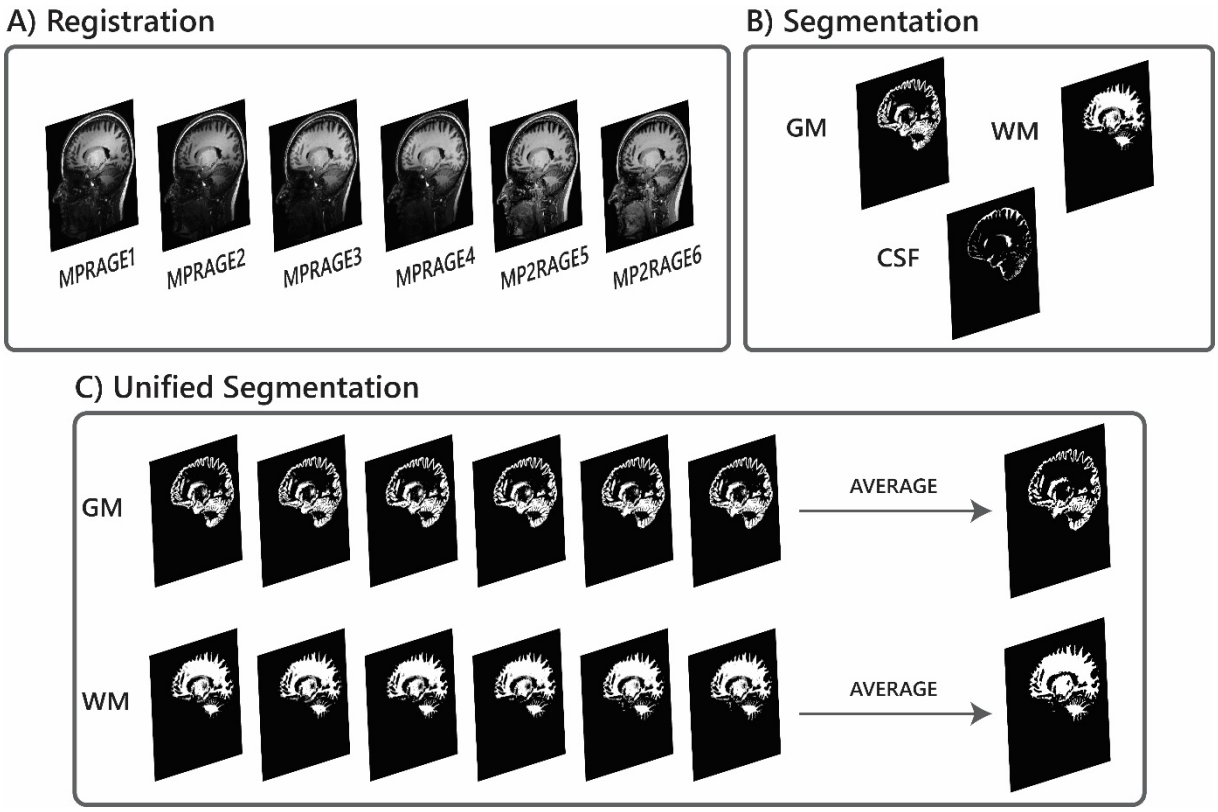

Fig. 1. Flowchart representation of the registration and segmentation used to create the unified GM and WM mask. A) Registration performed in SPM12. The panel B) shows the output of CAT12 segmentation, for a single sequence; after performing the segmentation in all six sequences, the GM and WM probability tissue maps were averaged, resulting in a single GM and WM masks. The voxels were assigned GM if they were GM in at least two datasets the same approach was used for the WM, and overlapped voxels were excluded from the final combined ROI.

Data Analysis

The k-space shutter blurriness evaluation metric was the local point spread function (PSF). A signal profile was taken along the LR axis through the ventricles for both MPRAGE1 and MPRAGE2. The Full width half maximum (FWHM) of the ventricles along this line was calculated. The FWHM estimation was performed for both MPRAGEs, per subject, and the differences were assessed using a paired t-test. Additionally, a sigmoid function, equation [2],

was fitted to part of the profiles covering the ventricle wall, and the slope parameter 'd' was taken as a measure of the steepness of the slope (Bazin et al., 2020).

$$y = a + \frac{b}{1 + e^{-\frac{x-c}{d}}} \qquad [2]$$

The quantitative assessment was based on Signal-to-Noise ratio (SNR) and Contrast-to-Noise ratio (CNR) measurements. The SNR was calculated using equation [3], where $\mu_{foreground}$ is the mean and $\sigma_{foreground}$ is the standard deviation of the signal over the foreground mask, with n equal to the number of voxels within the mask. The foreground mask corresponds to the combination of GM and WM masks. The CNR was calculated using equation [4], where μ_{GM} and μ_{WM} are the mean over GM and WM, respectively and σ_{GM} (standard deviation of GM) and σ_{WM} (standard deviation of WM). One-way ANOVAs with Tukey *post-hoc* analyses were used to assess the SNR and CNR differences between all the six sequences. All generated boxplots, and the repeated measures ANOVA estimation with Bonferroni Pairwise correction was performed using R (R Core Team, 2020), where *p*-values < 0.05 were considered statistically significant.

$$SNR = \mu_{(foreground)}/\sigma_{(foreground)} * \sqrt{n/(n-1)} \qquad [3]$$

$$CNR = abs(\mu_{WM} - \mu_{GM})/\sqrt{(\sigma_{WM}^2 + \sigma_{GM}^2)} \qquad [4]$$

The GM and WM ROI masks were used to assess the histograms of image intensity. Receiver operating characteristic (ROC) curves and area under the curve (AUC) were used to evaluate the robustness of separation from the GM and WM histogram intensity (GM and WM tissue fraction) peaks, reflecting which sequence yielded better segmentation. Both alternative metrics were calculated per subject.

We calculated the Dice Similarity Coefficient (DSC) (Dice, 1945) of the GM probability tissue mask (with threshold = 0.59) to compare the segmentation's spatial similarity among all six sequences. DSC is an overlap-based metric commonly used to validate segmentation boundaries, and in the present study, the DSC was used to verify that the segmentation is consistent.

Results

Fig. 2 shows the sagittal, coronal and axial views of all six T1-w images of a single representative subject (subject #2). Visual inspection suggests that there are no significant differences between MPRAGE1 and MPRAGE2. However, a less intense central brightening and more signal in the cerebellar cortex can be seen in MPRAGE3&4 compared to MPRAGE1&2 (Fig. 2, white arrow). Generally, the UPs recovered the signal in the low-B1 regions. Another observation was the more homogenous WM signal throughout the brain in MPRAGE3&4. The MP2RAGEs (Fig. 2, right column) were likewise visibly more homogeneous than MPRAGE1&2 (Fig. 2, left column). Example slices of T1w images from all six subjects can be seen in the supplementary material (Supplementary Fig. 1.). Noteworthy, the bias field gradually reduced from MPRAGE1/2 to MPRAGE3/4 and the MP2RAGEs (Supplementary Table. 2). With the used parameters, all protocols are expected to have some B1+ dependent spatial variation, even the MP2RAGEs (Haast et al., 2018; Marques et al., 2010). In addition, a residual B1- variation is expected in the MPRAGE data, even with the vendor-supplied CLEAR correction (Harvey et al., 2015).

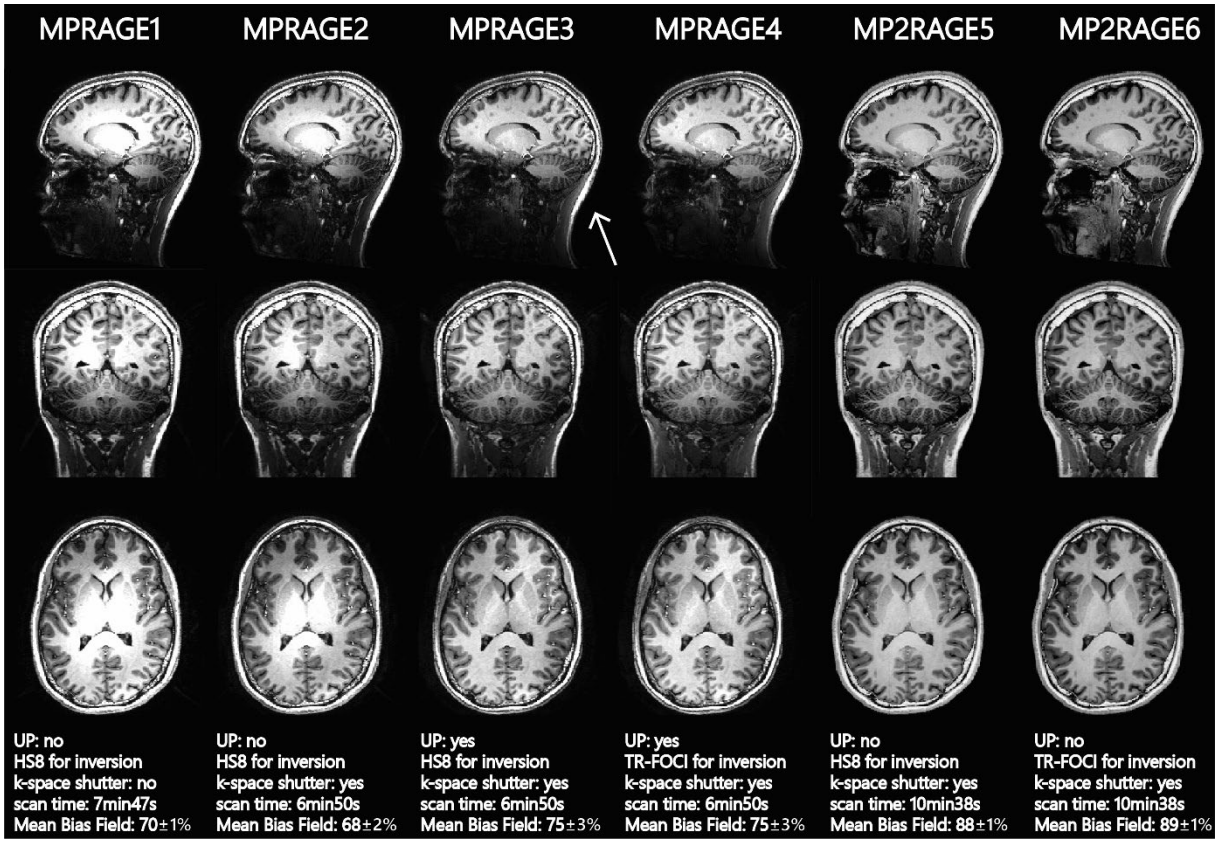

Fig.2. Sagittal, coronal and axial T1w example slices of subject #2 for all six acquisition protocols. The cerebellar area of low B1+ yields low signal in MPRAGE1 and MPRAGE2. A signal

increase is seen in the same regions by introducing the UP in MPRAGE3 (white arrow), where the central brightness also appears less intense. The bias field gradually reduced from MPRAGE1/2 to MPRAGE3/4 and the MP2RAGEs (Mean Percentage Bias Field gradually increases from MPRAGE1 to MP2RAGE6). Note that Mean Bias Field percentage is the estimated intensity effect (Bias Field) averaged across subjects. The percentage values represent the data quality estimated before the bias field correction in CAT12 (higher is better, representing the data quality).

Fig. 3a and b show the sampling pattern of the k-space shutter and the resulting point spread function (PSF). The observed profiles (Fig. 3B-G) show minimal changes; the most noticeable is the signal intensity reduction in MPRAGE2, related to the reduced scan time. We calculated the FWHM and the steepness of the slope for both MPRAGEs. No differences in FWHM in these profiles were observed (21.2+/- 1.0 and 21.3 +/- 1.0, Paired two-sided t-test p=0.36) and the slope parameter of the sigmoid fit was also stable (0.46 +/-0.04 and 0.45 +/- 0.04, Paired two-sided t-test p=0.52), suggesting that the edges were preserved with the application of the k-space shutter.

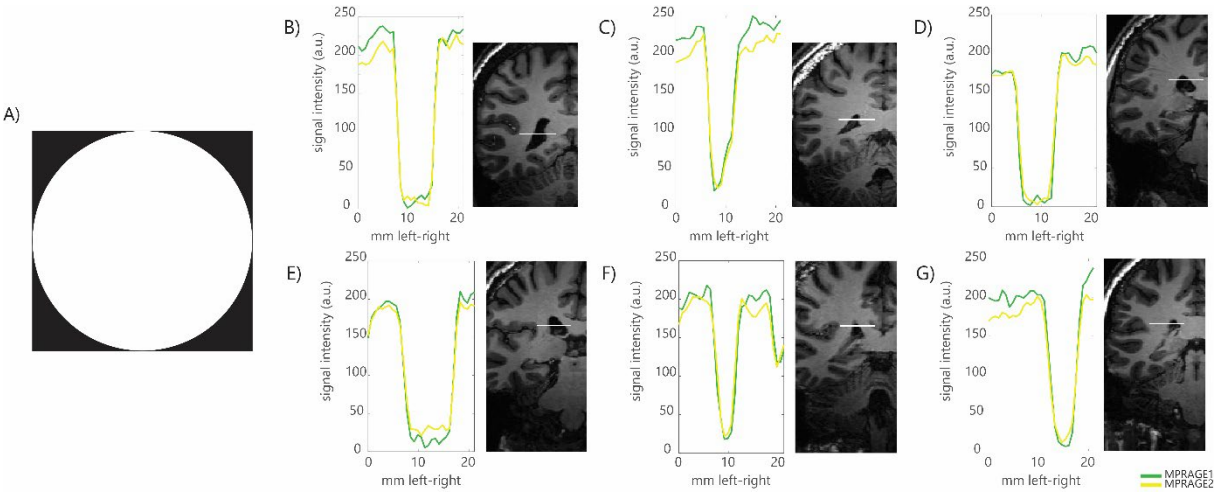

Fig.3. Panel A) shows the sampling pattern in k-space of the k-space shutter used on the k-space coverage for MPRAGE2-4 & MP2RAGE5 and 6. From B) to G) we show the signal profile along the Left-Right axis through the ventricles in individual subjects, the green signal profile represents MPRAGE1 signal profile, in which no elliptical shutter was employed and the yellow signal profile representing the MPRAGE2 signal, with k-space shutter yielding 25% scan time reduction. There was no difference in the estimated sharpness of the PSF.

The SNR and CNR assessment results of all sequences are shown in the boxplots in Fig. 4. Four distinct regions were assessed; a whole-brain ROI (including the cerebellum), a

cerebellum ROI, a right temporal lobe and a PCC, as example regions affected by B1+ inhomogeneities. For all ROIs, the UPs yielded higher SNR (all ROIs with $p < 0.05$), and when combined with TR-FOCI pulse, the SNR was even higher, notably for whole-brain and cerebellum (higher median, dark orange boxes). MP2RAGE also showed similar results; the introduction of the TR-FOCI pulse also led to a higher median SNR than the HS8 pulse in the whole-brain and cerebellum masks. It is worth mentioning that the low SNR values found here are also related to the contrast contributions to the signal variation, as the CNR of the gray/white matter difference showed a somewhat different pattern. CNR was higher for MP2RAGEs than the MPRAGEs, for both whole-brain and the cerebellum masks (both with $p < 0.05$), with the TR-FOCI in MP2RAGE6 leading to a slightly higher CNR (higher median) than the HS8 inversion in MP2RAGE5, though this difference was not statistically significant. Among the MPRAGEs, the measured CNR was similar, with only a slightly higher value for MPRAGE 3&4 (higher median) than MPRAGE 1&2, although also with higher variability between volunteers. It is also important to mention that the higher inter-subject variability in the right temporal and PCC masks are most likely due to differences in anatomy (gray/white matter ratio) across the subjects; an example of the positioning of both ROIs can be seen in the supplementary Fig.5. The SNR ($SNR/\sqrt{T_{acq}}$) and the CNR ($CNR/\sqrt{T_{acq}}$) per unit of time were also assessed to compensate for differences in acquisition time. For the SNR, a significant difference was observed ($p<0.05$) for the UPs (MPRAGE 3&4) when compared with other MPRAGEs and MP2RAGEs for all masks. As expected, the CNR increased when UPs were employed, however, with no significant differences to the MP2RAGEs, although it is worth mentioning that the CNR values are higher for MPRAGE3 in the right temporal and both MPRAGE3 & MPRAGE4 in the PCC mask. A detailed description of the SNR and CNR per unit of time can be seen in Supplementary Fig. 2.

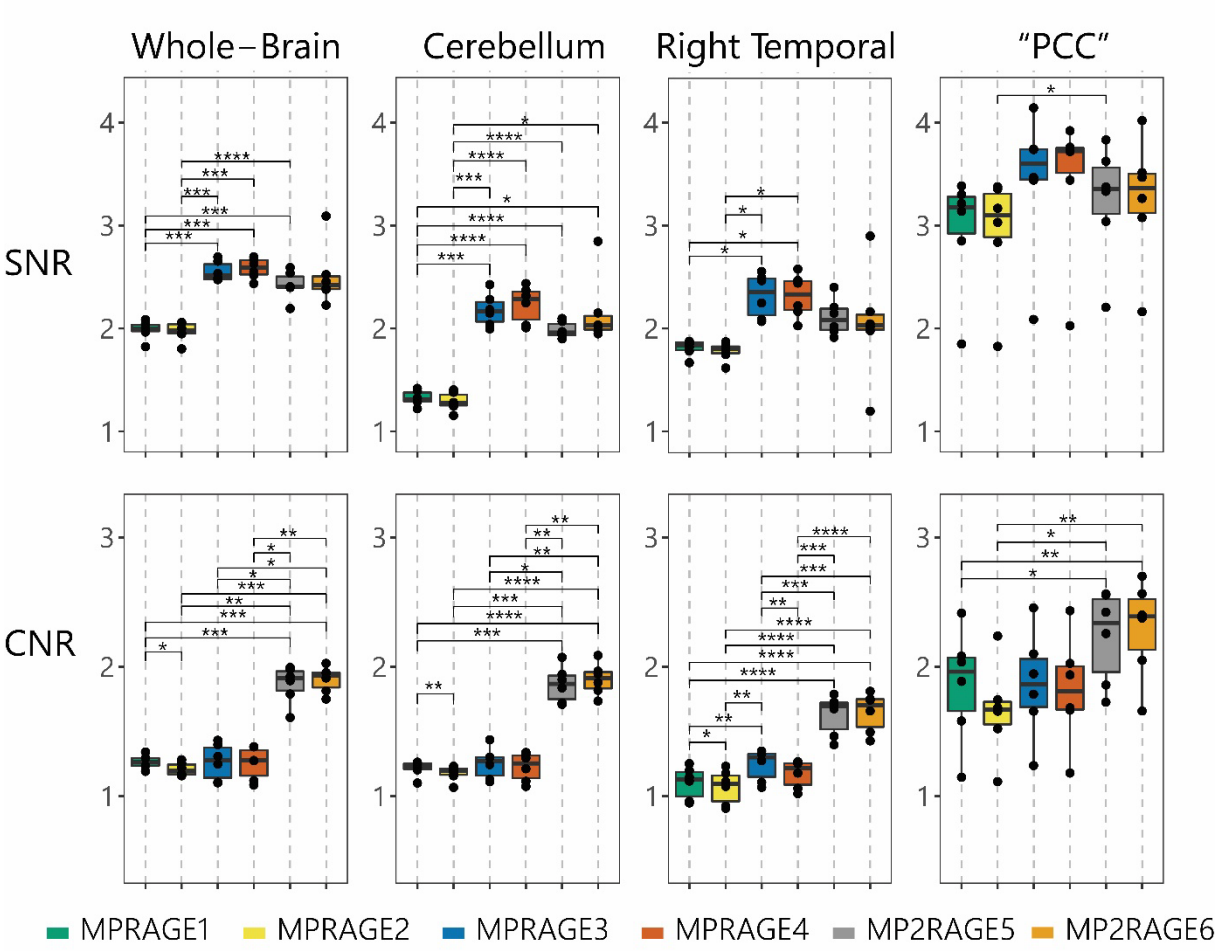

Fig.4. Boxplots for each sequence showing the SNR and CNR (between Gray and White matter) in the whole brain, cerebellum, the right temporal area and the 'PCC' (a cube centred on the posterior cingulate cortex). In all cases, the SNR was higher after introducing Universal pulses, MPRAGE3 (blue box) and MPRAGE4 (dark orange box) and higher after combining with the TR-FOCI (MPRAGE4, dark orange). In contrast, the CNR was higher for MP2RAGEs for all example areas. 'PCC' area resulted in higher inter-subject variability due to anatomy differences (gray/white matter ratio) across subjects.

Fig. 5 (Panels A and B) shows the histograms of the signal distributions in MPRAGE and MP2RAGE acquisitions. The gray matter (~100 and ~130) and white matter (~200 and ~300) signal intensities for the whole-brain (Fig. 5 Panel A) underwent a substantial shift after the introduction of the UPs for all subjects, relatively higher in the gray matter than in white matter. For the cerebellum (Fig. 5 Panel B) the same behaviour was observed, it also presented a shift towards higher intensities values after introducing the UPs. Note that the MP2RAGE intensities were put on a scale of 0-409.6 here, rather than the usual 0-4096. The intensity histograms for all six subjects are depicted in the supplementary material (Supplementary Fig. 3).

ROC curves and, subsequently, the AUC were calculated per scan and per subject to quantify the gray-white matter separability since the GM and WM intensity peaks are not entirely separated in the histograms. Fig. 5 (Panels C and D) shows the GM and WM fraction's ROC curves for one representative subject. The ROC curves from all six subjects are depicted in supplementary Fig.4. For the example subject, as for the other individuals, the ROC curves were higher for the MP2RAGE than for the MPRAGEs, with only small differences between MPRAGE acquisitions. To summarise the segmentability in a single number, the area under the curve, or AUCs, for the whole brain ROI and the cerebellum were generated and shown in violin/boxplot format (Fig. 5, Panels E and F). AUCs were consistently higher for the MP2RAGEs. Among the MPRAGEs acquisitions, MPRAGE3&4 showed slightly higher values than MPRAGE1&2 for the whole-brain ROI (Fig.5 Panel E) while, on the other hand, for the cerebellum ROI (Fig.5 Panel F) the MPRAGE 1&2 show higher values than MPRAGE3&4.

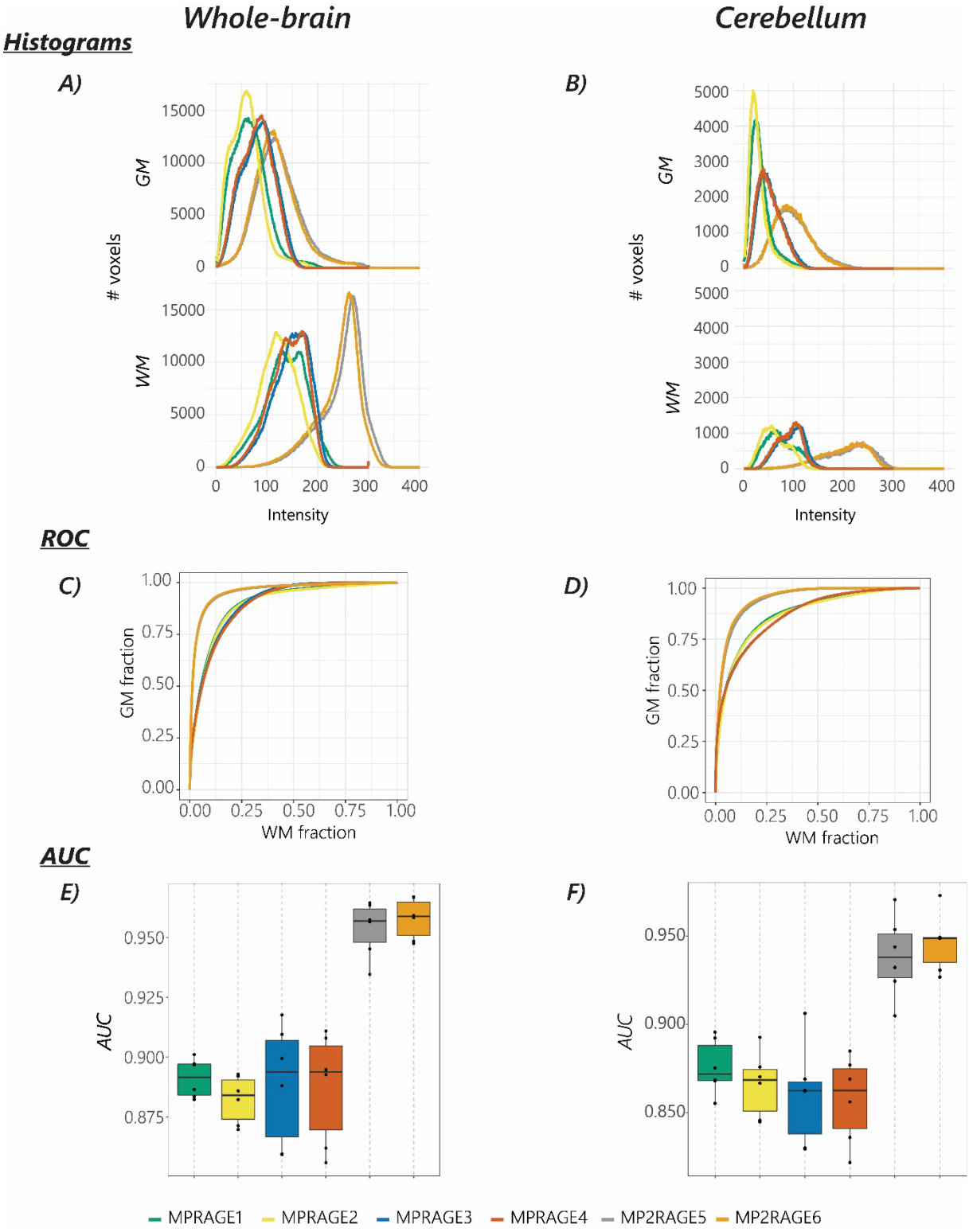

Fig.5. Signal distribution in MPRAGE and MP2RAGE acquisitions for both GM and WM tissues. In A) Whole-brain and B) cerebellum ROIs for one representative subject. The Gray matter peaks are the first ones (upper part, graphics A and B), while below is the White matter. Note that the MP2RAGE intensities are divided by a factor of 10 to match the x-axis. Panel C and D are the ROC curves of the same representative subject for whole-brain and cerebellum, respectively. The curves show better separability of GM and WM for MP2RAGE compared with

MPRAGE for both masks. Areas under the curve (AUC) for whole-brain (Panel E) and cerebellum (Panel F). MP2RAGE shows better GM/WM segmentability.

Fig. 6 shows the Dice coefficients of the GM probability tissue, averaged over all six subjects. (Panel A for whole-brain and Panel B for cerebellum). The DSC per subject can be seen in supplementary material (Supplementary Table 1.a-b). The purpose of this metric is to verify how similar the segmentations are. DSC coefficient shows that the segmentation results from MPRAGE1 and MPRAGE2 were highly similar. Even higher similarity was observed between MPRAGE 3&4 and between MP2RAGE 5&6. It is worth pointing out that the segmentation performance of MPRAGE3&4 scored higher values than the MPRAGE1&2 when the reference was the MP2RAGE5 or MP2RAGE6.

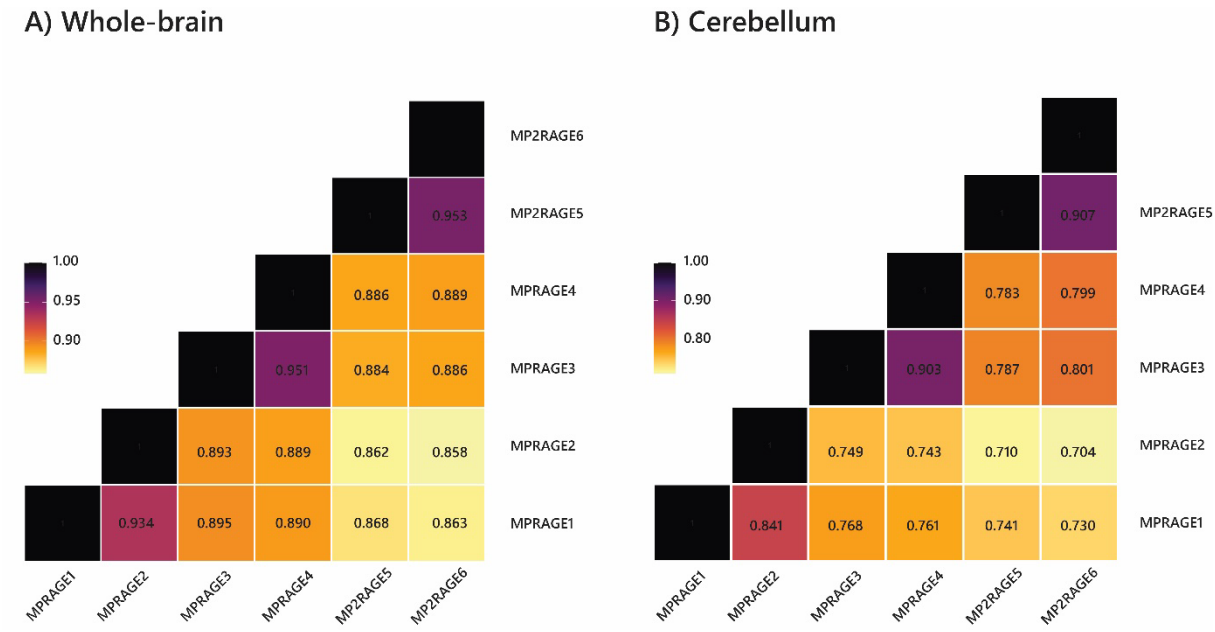

Fig.6. Dice Similarity Coefficient (DSC) of GM probability tissue averaged over all six subjects. Panel A) whole-brain mask and Panel B) cerebellum mask. Dice similarity coefficient evaluates the segmentation's performance by measuring their spatial overlapping (higher is better). The present study highlights which sequence offers the best segmentation or approximates from the ideal. The Dice coefficient shows that the MPRAGE 1&2 were highly similar. Another high similarity was observed between MPRAGE 3&4 and between MP2RAGE 5&6. The MPRAGE 3&4 scored higher values than the MPRAGE 1&2 when the reference was one of the MP2RAGEs.

Discussion

In this study, we compared different strategies to improve whole-brain MPRAGE acquisitions at 7T. A k-space shutter was used to reduce the scan time further, Universal kt-point pulses were used to homogenize signal excitation, and the TR-FOCI was used to invert the signal more uniformly. All these MPRAGE variations were compared to MP2RAGE data acquired with two different inversion pulses (HS8 and TR-FOCI). We anticipated that combining all advanced techniques would yield higher SNR and CNR, resulting in a better separability of Gray and White Matter for MPRAGE with comparable results with the MP2RAGE acquisition which is now very widely used at 7T. Interestingly, we found that the UPs and the TR-FOCI pulse provide a robust uniformity and an increase in SNR; however, it does not translate into better segmentability than MP2RAGE.

The use of a k-space shutter did not significantly affect the MPRAGE in terms of SNR (Fig. 2), and no difference in blurring at the high contrast edge of the ventricles was found (Fig. 3). These results were expected since the outer regions of the k-space only have small signal amplitude compared with the amount of noise; removing the corners of k-space results in a minimal loss of spatial resolution and considerable time saving for MPRAGE (~25%, here approximately two minutes). It seems safe to use a k-space shutter to save scan time where the loss in SNR because of the reduced scan time is not harmful. For these medium-resolution anatomical images, the loss in SNR does not affect the segmentation quality (Fig. 6).

Quantitative assessment was performed using SNR and CNR as metrics over the different acquisitions. The increased SNR offered by introducing the UPs (MPRAGE 3&4) shows a remarkable improvement compared to the other sequences used, including the MP2RAGE, for both whole-brain and cerebellum. The TR-FOCI pulse introduction resulted in a higher inversion efficiency and SNR, especially in the cerebellum, as expected (O'Brien et al., 2014b). However, the difference was not as large as in the O'Brien study, which used a single-channel transmit coil. A possible explanation might thus be the TX8 Nova coil's performance, which already provides good B1+ coverage over the brain. However, without a direct hardware comparison, this remains speculation. The increase in SNR achieved in MPRAGE3&4 did not translate to higher CNR values than MP2RAGEs (Fig.4). This result is most likely due to the balance of tissue types in the areas most affected by the B1+-inhomogeneity. These contain

mainly gray matter, and with increasing brightness becomes closer in intensity to the overall white matter peak.

Regarding the signal distribution (Fig. 5), both GM and WM signal increased with the introduction of the UPs; the dark orange/blue curves are moving to the right in the histogram for all subjects in the supplementary material (Supplementary Fig. 3). Similar behaviour was observed in previous work when UPs also induced a signal increase compared with CP mode (Gras et al., 2017). Again, as the gray matter peak moved more than the WM peak, the signal intensity distribution of gray and white matter did not become better separable in MPRAGE3 or MPRAGE4 (Fig.5A-B). This effect is especially clear in Fig.5E-F, where the AUC improved a bit in the whole brain acquisition, probably because of the higher SNR, but decreased for MPRAGE3&4 compared to MPRAGE1&2 in the cerebellum, where the increase in GM signal intensities was largest. With the two signal compartments closer together in the image intensity histogram, they overlapped more. Nevertheless, the (cerebellar) segmentations in MPRAGE3&4 were more consistent than in MPRAGE1&2, as shown by the off-diagonal values in Fig. 6.B.

We also compared the segmentation of gray and white matter, using the Dice coefficient to measure the segmentation stability. A high overlap was observed between MPRAGE 1 (no shutter) &2 (shutter), meaning that the k-space shutter's introduction does not compromise the MPRAGE contrast. Even higher dice coefficients were observed between MPRAGE 3&4 and between MP2RAGE 5&6, which means that these pairs of acquisitions yielded very consistent segmentation of GM/WM. Interestingly, the segmentation performance of MPRAGE 3&4 scored higher values than the MPRAGE 1&2 when the reference was one of the MP2RAGEs, which means that the introduction of the UPs and the TR-FOCI pulse lead to better segmentation than a standard MPRAGE.

Nevertheless, all our results and extracted image quality metrics show that the MPRAGE does not yet match the MP2RAGE for gray and white matter contrast or segmentability. We achieved higher signal homogeneity using Universal Pulses (UPs) and TR-FOCI inversion and shorter scan time with k-space shutter. However, the increase in SNR obtained for MPRAGE was insufficient to translate directly into better CNR values or better separability of GM and WM than MP2RAGE. Hence, in their current implementation, MP2RAGE still merits the additional scan time for a T1-weighted 7T anatomical scan. A further advantage from MP2RAGE

acquisitions is that a T_1-map can be obtained from the data at no extra scan time (Marques et al., 2010), but as these are not relevant when the images are only used as anatomical background, this has not been further considered here. Nevertheless, for applications where scan time is limited and segmentation not the primary objective, such as for fMRI anatomical reference data, an MPRAGE with UPs and TR-FOCI is a very good alternative.

A higher variability in CNR and AUC was observed for MPRAGEs 3&4. In line with (Gras et al., 2017), we speculate that the higher variation in flip angle maps was most likely due to variations in the head position. Several parameters in these protocols affect the expected SNR and contrast beyond the inclusion of a second readout. Here, we selected the acquisition parameters based on two 'standard' protocols (the proposed MP2RAGE and the ADNI protocol), while adapting for the inclusion of a k-space shutter and the field strength and fixing the spatial coverage, voxel size and undersampling factors. Moreover, the use of universal pulses in the MP2RAGE would strengthen even further the MP2RAGE dataset, as we can see from (Mauconduit et al., 2020). The addition of the UPs brings the advantage of intrinsically correcting for flip angle variations throughout the brain. Another possibility is the use of post-hoc correction based on Sa2RAGE to remove residual $B1^+$ effects (Haast et al., 2021, 2018). Besides B1 inhomogeneities solutions, fat navigators (fatNavs) for retrospective motion correction could also improve image quality even further (Federau and Gallichan, 2016; Gallichan et al., 2016).

Finally, it is worth pointing out that although UPs for excitation and TR-FOCI pulse for inversion did not allow the MPRAGE to match MP2RAGE for gray-white matter contrast, the SNR, CNR and segmentability were much improved compared with the standard MPRAGE sequence and their use is highly recommended. A k-space shutter was also introduced without detrimental effects and seems an excellent way of saving scan time without a loss in image PSF.

Conclusion

Higher signal homogeneity was achieved in MPRAGE data using Universal Pulses (UPs) and TR FOCI inversion; however, the higher SNR obtained for MPRAGE did not translate directly into better separability of GM-WM. A possible explanation is that the signal increase is more

pronounced in GM than in WM. Our results show that the MPRAGE does not yet match MP2RAGE for gray- white matter contrast, even after a robust SNR increase using sophisticated alternative pulses. The additional scan time of an MP2RAGE acquisition seems merited. Nevertheless, for applications where scan time is limited and segmentation not the primary objective, an MPRAGE with UPs and TR-FOCI is a good alternative.

Supplementary material

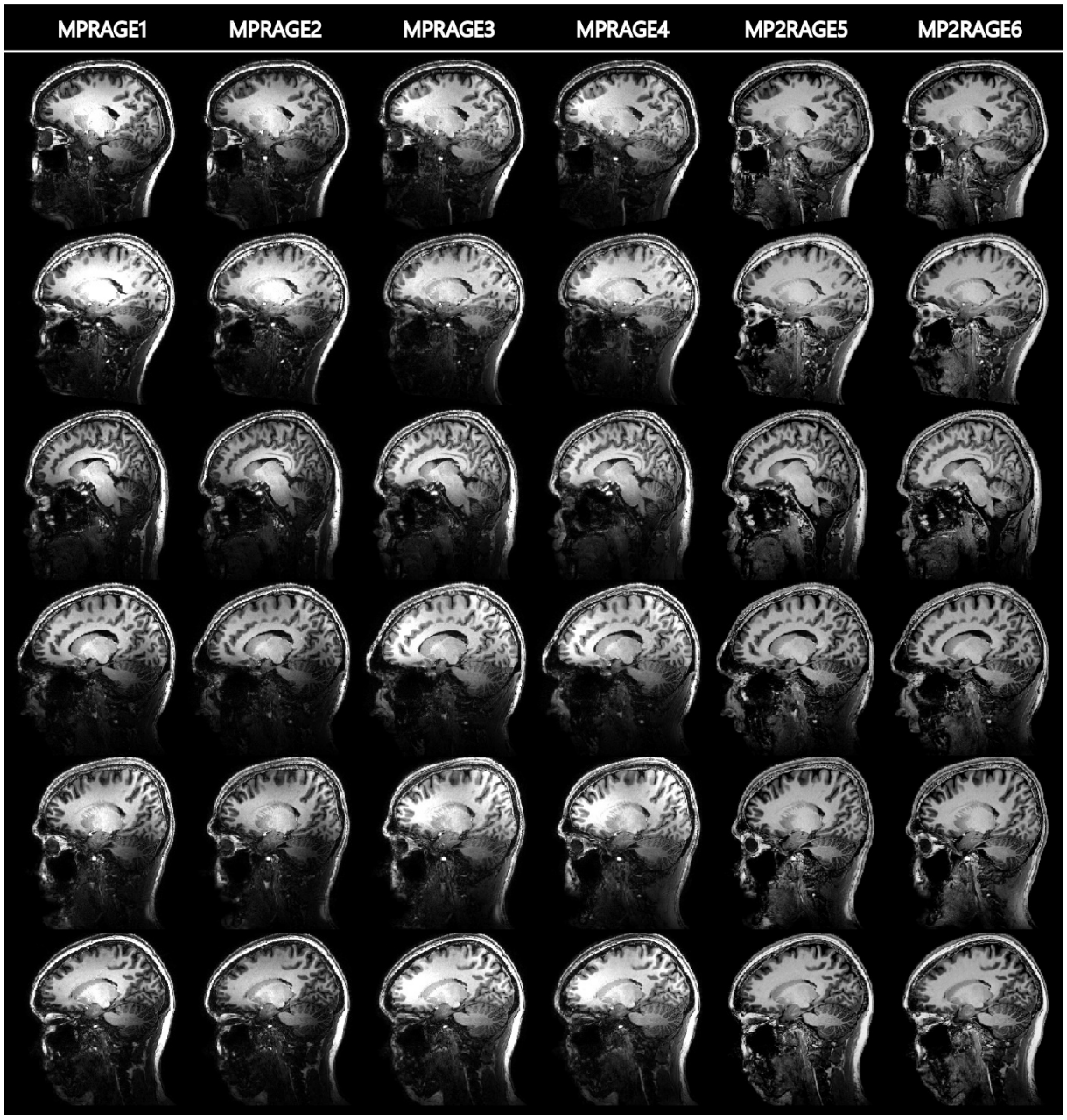

Supplementary Fig. 1. Sagittal T1w for all six subjects and acquisition protocols. From left to right: MPRAGE1 (no shutter + HS8), MPRAGE2 (shutter + HS8), MPRAGE3 (shutter + HS8 + UPs), MPRAGE4 (shutter + TR-FOCI + UPs), MP2RAGE5 (shutter + HS8) and MP2RAGE6 (shutter + TR-FOCI). A signal increase is specially seen in the cerebellar areas after the introduction of the Universal Pulses (MPRAGE3 & MPRAGE4) in all six subjects.

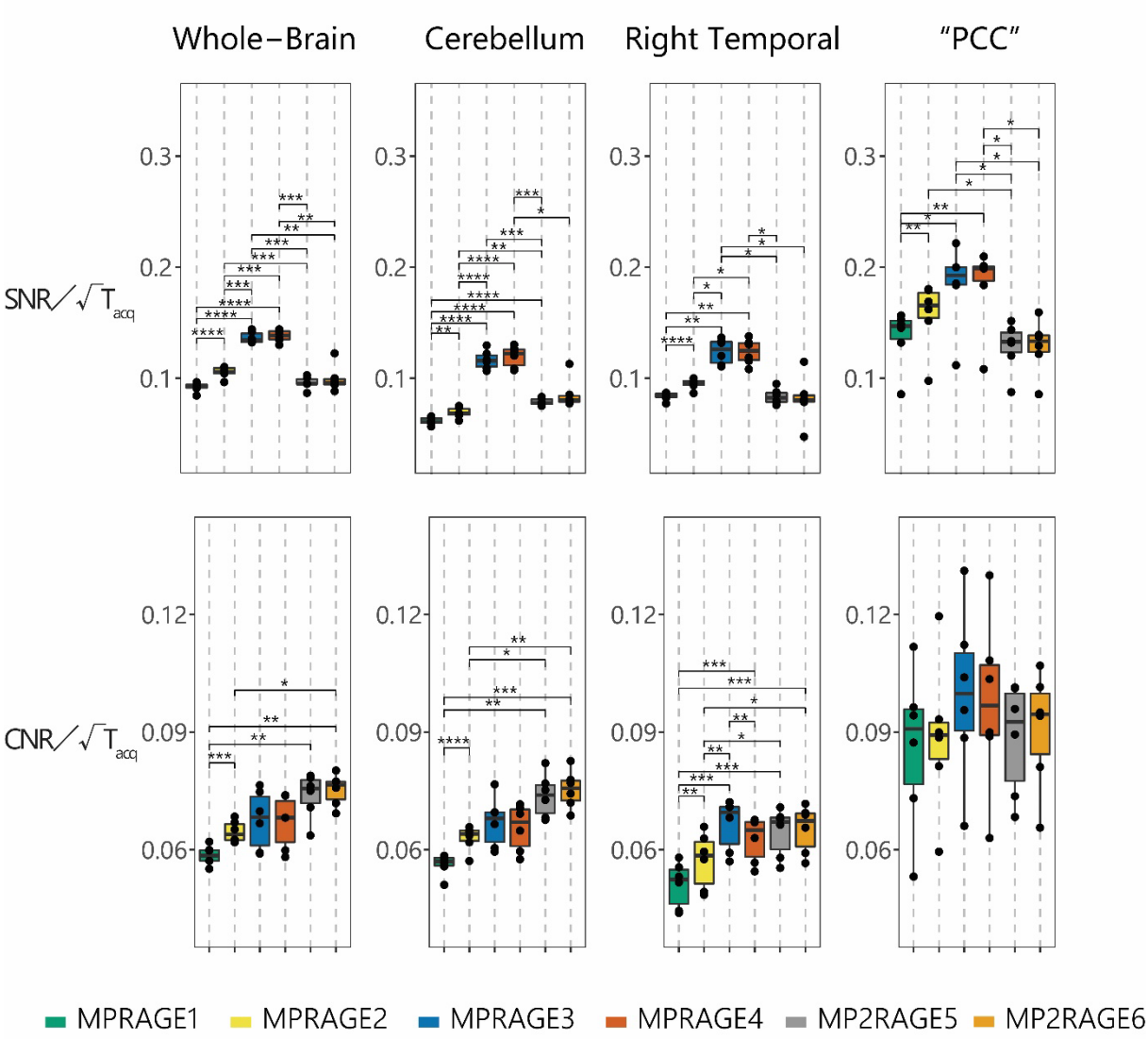

Supplementary Fig.2: Boxplots for each sequence showing the SNR ($SNR/\sqrt{T_{acq}}$) and the CNR ($CNR/\sqrt{T_{acq}}$) per time unit (between Gray and White matter). Whole-brain, cerebellum, the right temporal area and the 'PCC' (a cube centred on the posterior cingulate cortex) were assessed. In all cases, the SNR was higher after introducing Universal pulses, MPRAGE3 (blue box) and MPRAGE4 (dark orange box), and higher after combining with the TR-FOCI (MPRAGE4, dark orange). As expected, the CNR increased when UPs were employed (MPRAGE3 and MPRAGE4), however, with no significant differences to the MP2RAGEs. A repeated measure ANOVA with Bonferroni Pairwise correction (pwc) was performed to allow comparisons within the subject's means.

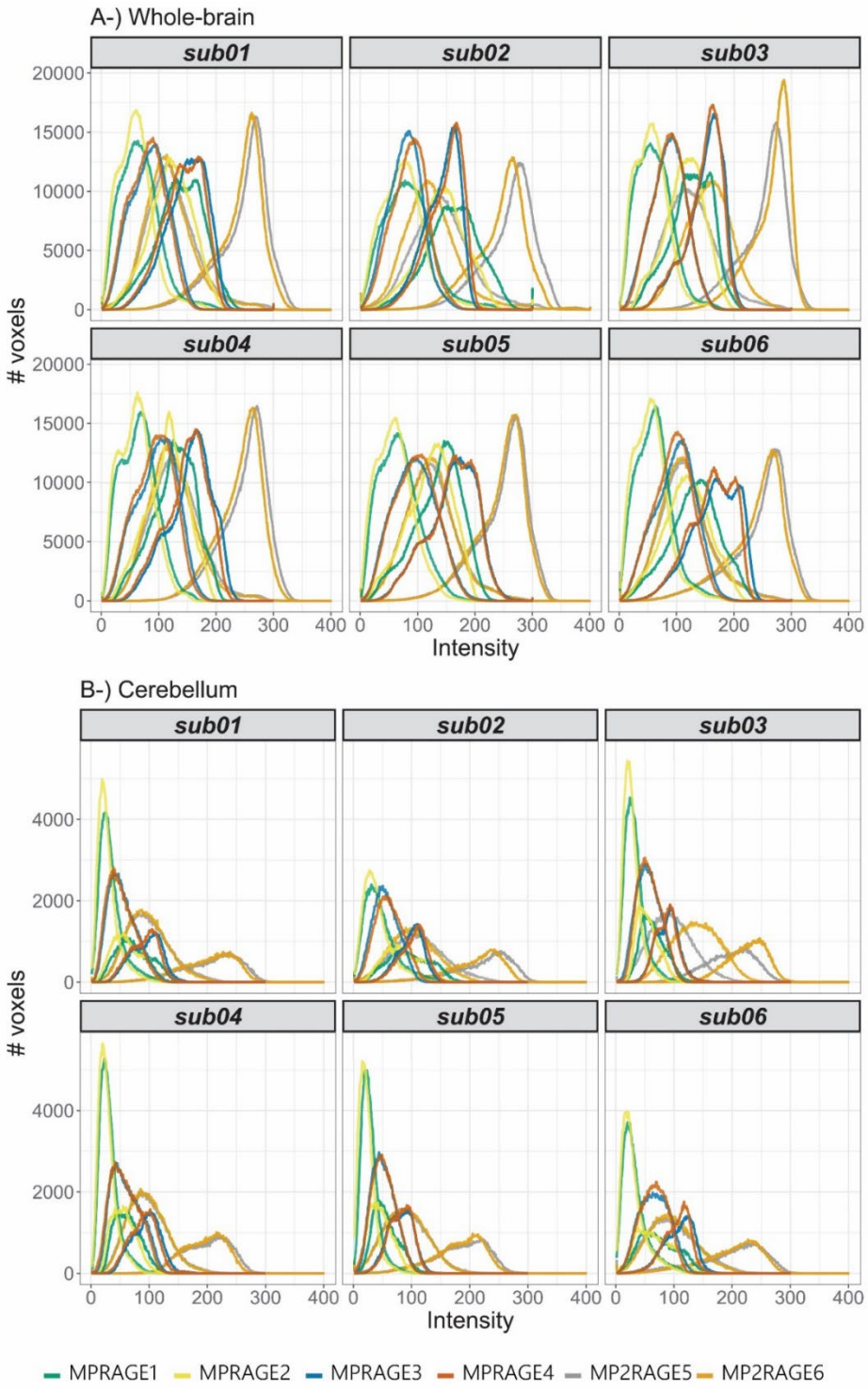

Supplementary Fig. 3. Signal distribution in MPRAGE and MP2RAGE acquisition for GM and WM matter tissues. A) Whole-brain and B) Cerebellum ROIs, for all six subjects. Note that the MP2RAGE intensities are divided by a factor of 10.

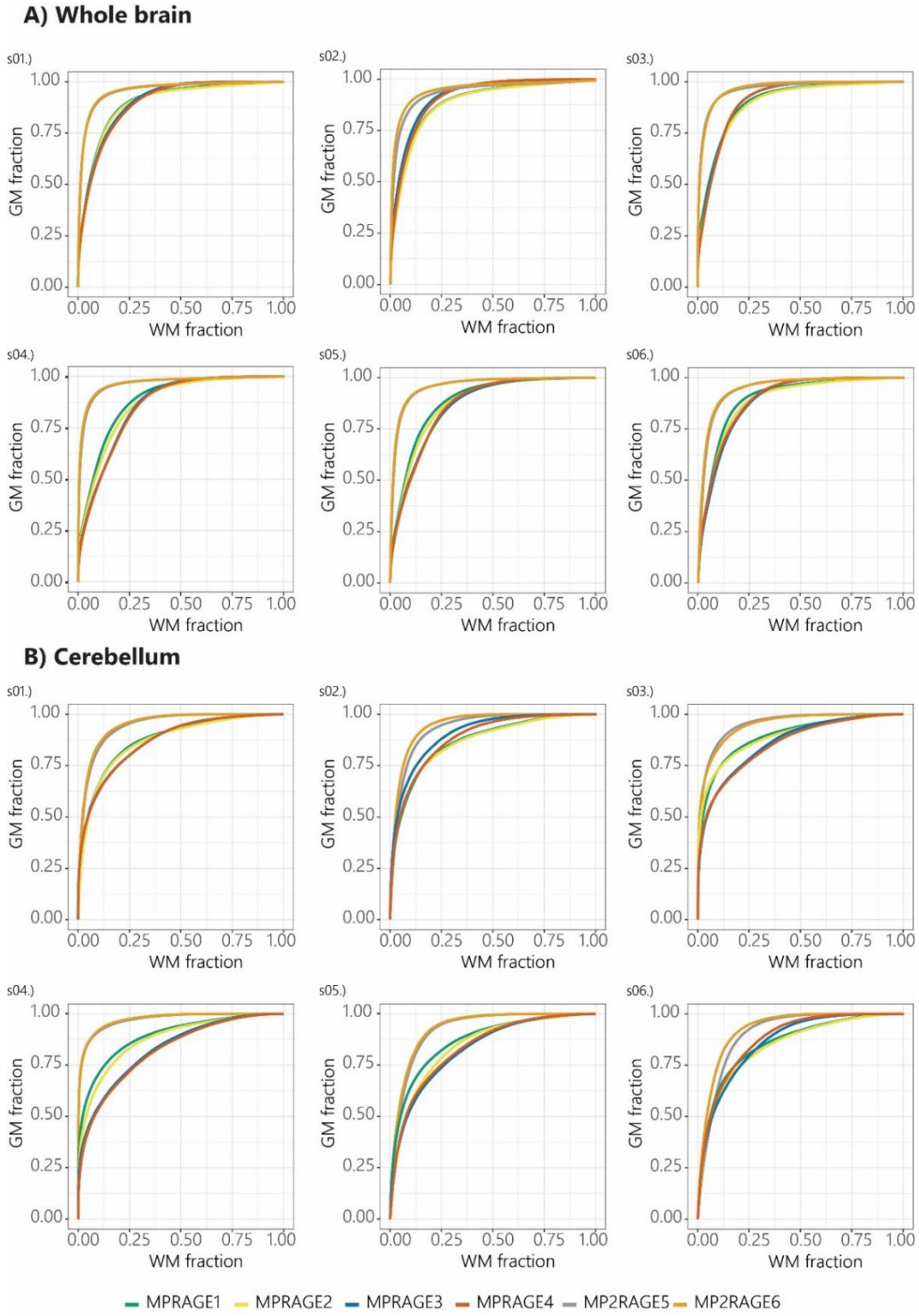

Supplementary Fig. 4. ROC curves of all six subjects for whole-brain and Cerebellum. For all subjects, the curves show better separability of GM and WM for MP2RAGE compared with MPRAGE for both masks.

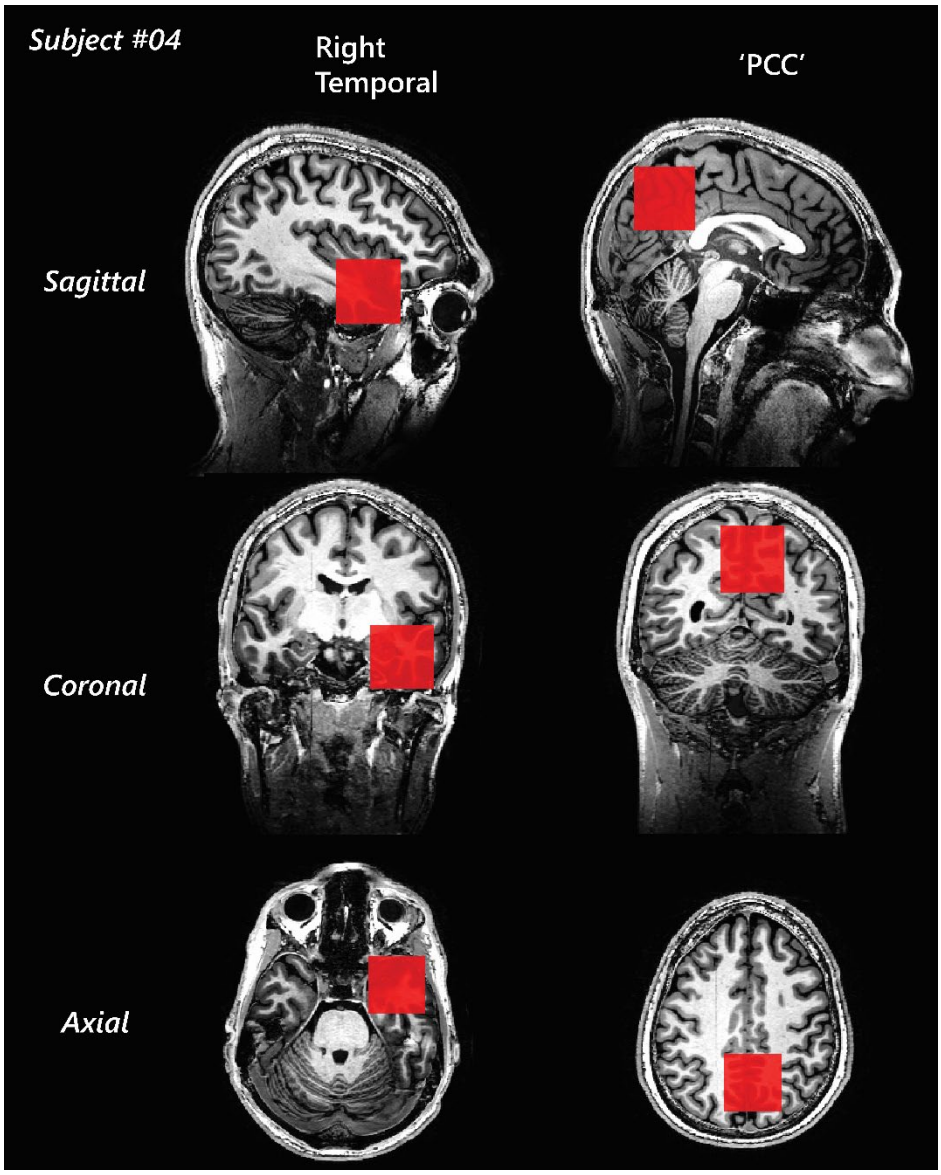

Supplementary Fig. 5. Example data from the ROI position in one subject (subject #4). Two cubic ROIs were added as low (Temporal area) and high (PCC)-$B1^+$ areas. On the left, the Right temporal ROI, and the right the 'PCC' (a cube centred on the posterior cingulate cortex).

DICE Coefficient	*sub 1*	*sub 2*	*sub 3*	*sub 4*	*sub 5*	*sub 6*	*MEAN*	*SD*
MPRAGE 1 & 2	*0.95*	*0.94*	*0.93*	*0.94*	*0.91*	*0.93*	*0.93*	*0.02*
MPRAGE 1 & 3	*0.90*	*0.91*	*0.90*	*0.90*	*0.87*	*0.89*	*0.89*	*0.01*
MPRAGE 1 & 4	*0.89*	*0.90*	*0.89*	*0.88*	*0.88*	*0.89*	*0.89*	*0.01*
MPRAGE 1 & 5	*0.87*	*0.87*	*0.88*	*0.89*	*0.88*	*0.83*	*0.87*	*0.02*
MPRAGE 1 & 6	*0.86*	*0.87*	*0.86*	*0.89*	*0.87*	*0.83*	*0.86*	*0.02*
MPRAGE 2 & 3	*0.90*	*0.90*	*0.91*	*0.90*	*0.87*	*0.88*	*0.89*	*0.01*
MPRAGE 2 & 4	*0.89*	*0.90*	*0.90*	*0.88*	*0.88*	*0.88*	*0.89*	*0.01*
MPRAGE 2 & 5	*0.86*	*0.87*	*0.87*	*0.89*	*0.87*	*0.82*	*0.86*	*0.02*
MPRAGE 2 & 6	*0.86*	*0.87*	*0.86*	*0.88*	*0.87*	*0.82*	*0.86*	*0.02*
MPRAGE 3 & 4	*0.95*	*0.95*	*0.96*	*0.96*	*0.92*	*0.96*	*0.95*	*0.02*
MPRAGE 3 & 5	*0.90*	*0.87*	*0.89*	*0.90*	*0.88*	*0.86*	*0.88*	*0.02*
MPRAGE 3 & 6	*0.89*	*0.88*	*0.90*	*0.90*	*0.88*	*0.86*	*0.89*	*0.01*
MPRAGE 4 & 5	*0.90*	*0.87*	*0.90*	*0.89*	*0.88*	*0.87*	*0.89*	*0.01*
MPRAGE 4 & 6	*0.90*	*0.88*	*0.91*	*0.89*	*0.89*	*0.87*	*0.89*	*0.01*
MP2RAGE 5 & 6	*0.97*	*0.96*	*0.93*	*0.95*	*0.96*	*0.95*	*0.95*	*0.01*

Supplementary Table 1.a. The table shows the Dice Similarity Coefficient in the Gray matter probability tissue for all subjects and sequences, with their respective mean and standard deviation for the whole-brain.

DICE Coefficient	*Sub 1*	*Sub 2*	*Sub 3*	*Sub 4*	*Sub 5*	*Sub 6*	*MEAN*	*SD*
MPRAGE 1 & 2	*0.87*	*0.89*	*0.81*	*0.86*	*0.77*	*0.85*	*0.84*	*0.04*
MPRAGE 1 & 3	*0.80*	*0.81*	*0.76*	*0.78*	*0.71*	*0.74*	*0.77*	*0.04*
MPRAGE 1 & 4	*0.79*	*0.80*	*0.73*	*0.77*	*0.73*	*0.74*	*0.76*	*0.03*
MPRAGE 1 & 5	*0.75*	*0.73*	*0.79*	*0.81*	*0.72*	*0.67*	*0.74*	*0.05*
MPRAGE 1 & 6	*0.74*	*0.74*	*0.70*	*0.80*	*0.72*	*0.68*	*0.73*	*0.04*
MPRAGE 2 & 3	*0.78*	*0.80*	*0.75*	*0.78*	*0.67*	*0.72*	*0.75*	*0.05*
MPRAGE 2 & 4	*0.78*	*0.79*	*0.72*	*0.77*	*0.70*	*0.71*	*0.74*	*0.04*
MPRAGE 2 & 5	*0.72*	*0.73*	*0.74*	*0.78*	*0.66*	*0.64*	*0.71*	*0.05*
MPRAGE 2 & 6	*0.71*	*0.74*	*0.68*	*0.78*	*0.65*	*0.66*	*0.70*	*0.05*
MPRAGE 3 & 4	*0.91*	*0.93*	*0.92*	*0.90*	*0.83*	*0.92*	*0.90*	*0.03*
MPRAGE 3 & 5	*0.81*	*0.79*	*0.82*	*0.81*	*0.75*	*0.75*	*0.79*	*0.03*
MPRAGE 3 & 6	*0.81*	*0.80*	*0.85*	*0.82*	*0.76*	*0.77*	*0.80*	*0.03*
MPRAGE 4 & 5	*0.80*	*0.78*	*0.82*	*0.78*	*0.76*	*0.75*	*0.78*	*0.03*
MPRAGE 4 & 6	*0.80*	*0.79*	*0.86*	*0.80*	*0.77*	*0.77*	*0.80*	*0.03*
MP2RAGE 5 & 6	*0.94*	*0.94*	*0.84*	*0.92*	*0.91*	*0.91*	*0.91*	*0.04*

Supplementary Table 1.b. The table shows the Dice Similarity Coefficient in the Gray matter probability tissue for all subjects and sequences, with their respective mean and standard deviation for the Cerebellum.

Bias	*s01*	*s02*	*s03*	*s04*	*s05*	*s06*	*MEAN*	*SD*
MPRAGE 1	*70.43%*	*71.94%*	*70.83%*	*67.91%*	*70.58%*	*68.26%*	*69.99%*	*1.44%*
MPRAGE 2	*69.54%*	*71.99%*	*69.73%*	*66.07%*	*67.63%*	*66.33%*	*68.55%*	*2.09%*
MPRAGE 3	*76.13%*	*79.57%*	*77.39%*	*72.13%*	*71.51%*	*74.73%*	*75.24%*	*2.83%*
MPRAGE 4	*75.38%*	*80.05%*	*77.23%*	*71.94%*	*71.26%*	*74.98%*	*75.14%*	*3.00%*
MP2RAGE 5	*89.48%*	*88.96%*	*88.93%*	*88.11%*	*88.16%*	*88.82%*	*88.74%*	*0.48%*
MP2RAGE 6	*89.65%*	*88.57%*	*91.87%*	*88.08%*	*87.87%*	*90.15%*	*89.37%*	*1.38%*

Supplementary table 2: The estimated intensity effects (Bias Field) in percentage (higher is better) calculated by the CAT12 algorithm prior to applying the bias field correction during the segmentation procedure.

References

Bazin, P.-L., Nijsse, H.E., van der Zwaag, W., Gallichan, D., Alkemade, A., Vos, F.M., Forstmann, B.U., Caan, M.W.A., 2020. Sharpness in motion corrected quantitative imaging at 7T. Neuroimage 222, 117227. https://doi.org/10.1016/j.neuroimage.2020.117227

Cloos, M.A., Boulant, N., Luong, M., Ferrand, G., Giacomini, E., Le Bihan, D., Amadon, A., 2012. KT-points: Short three-dimensional tailored RF pulses for flip-angle homogenization over an extended volume. Magn. Reson. Med. 67, 72–80. https://doi.org/10.1002/mrm.22978

Deniz, C.M., 2019. Parallel Transmission for Ultrahigh Field MRI. Top. Magn. Reson. Imaging 28, 159–171. https://doi.org/10.1097/RMR.0000000000000204

Dice, L.R., 1945. Measures of the amount of ecologic association between species. Ecology 26, 297–302. https://doi.org/10.2307/1932409

Federau, C., Gallichan, D., 2016. Motion-correction enabled ultra-high resolution in-vivo 7T-MRI of the brain. PLoS One 11, 1–12. https://doi.org/10.1371/journal.pone.0154974

Fujimoto, K., Polimeni, J.R., van der Kouwe, A.J.W., Reuter, M., Kober, T., Benner, T., Fischl, B., Wald, L.L., 2014. Quantitative comparison of cortical surface reconstructions from MP2RAGE and multi-echo MPRAGE data at 3 and 7T. Neuroimage 90, 60–73. https://doi.org/10.1016/j.neuroimage.2013.12.012

Gallichan, D., Marques, J.P., Gruetter, R., 2016. Retrospective correction of involuntary microscopic head movement using highly accelerated fat image navigators (3D FatNavs) at 7T. Magn. Reson. Med. 75, 1030–1039. https://doi.org/10.1002/mrm.25670

Garwood, M., DelaBarre, L., 2001. The Return of the Frequency Sweep: Designing Adiabatic Pulses for Contemporary NMR. J. Magn. Reson. 153, 155–177. https://doi.org/10.1006/jmre.2001.2340

Gras, V., Mauconduit, F., Vignaud, A., Amadon, A., Le Bihan, D., Stöcker, T., Boulant, N., 2018. Design of universal parallel-transmit refocusing k T -point pulses and application to 3D T 2 -weighted imaging at 7T. Magn. Reson. Med. 80, 53–65. https://doi.org/10.1002/mrm.27001

Gras, V., Poser, B.A., Wu, X., Tomi-Tricot, R., Boulant, N., 2019a. Optimizing BOLD sensitivity in the 7T Human Connectome Project resting-state fMRI protocol using plug-and-play parallel transmission. Neuroimage 195, 1–10. https://doi.org/10.1016/j.neuroimage.2019.03.040

Gras, V., Pracht, E.D., Mauconduit, F., Le Bihan, D., Stöcker, T., Boulant, N., 2019b. Robust nonadiabatic T2 preparation using universal parallel-transmit kT-point pulses for 3D FLAIR imaging at 7 T. Magn. Reson. Med. 81, 3202–3208. https://doi.org/10.1002/mrm.27645

Gras, V., Vignaud, A., Amadon, A., Le Bihan, D., Boulant, N., Bihan, D. Le, Boulant, N., Le Bihan, D., Boulant, N., 2017. Universal pulses: A new concept for calibration-free parallel transmission. Magn. Reson. Med. 77, 635–643. https://doi.org/10.1002/mrm.26148

Grissom, W.A., Khalighi, M.M., Sacolick, L.I., Rutt, B.K., Vogel, M.W., 2012. Small-tip-angle spokes pulse design using interleaved greedy and local optimization methods. Magn. Reson. Med. 68, 1553–1562. https://doi.org/10.1002/mrm.24165

Haast, R.A.M., Ivanov, D., Uludağ, K., 2018. The impact of B1+ correction on MP2RAGE cortical T 1 and apparent cortical thickness at 7T. Hum. Brain Mapp. 39, 2412–2425. https://doi.org/10.1002/hbm.24011

Haast, R.A.M., Lau, J.C., Ivanov, D., Menon, R.S., Uludağ, K., Khan, A.R., 2021. Effects of MP2RAGE B1+ sensitivity on inter-site T1 reproducibility and hippocampal morphometry at 7T. Neuroimage 224, 117373. https://doi.org/10.1016/j.neuroimage.2020.117373

Harvey, P.R., Rozijn, T.H., Ijperen, G.H., Prins, W.M., Mens, Wilhelmus R. M. Benschop, F.J.M., 2015. Image intensity correction for magnetic resonance imaging. 9036884.

Huber, L. (Renzo), Poser, B.A., Bandettini, P.A., Arora, K., Wagstyl, K., Cho, S., Goense, J., Nothnagel, N., Morgan, A.T., van den Hurk, J., Müller, A.K., Reynolds, R.C., Glen, D.R., Goebel, R., Gulban, O.F., 2021. LayNii: A software suite for layer-fMRI. Neuroimage 237, 118091. https://doi.org/10.1016/j.neuroimage.2021.118091

Huntenburg, J.M., Steele, C.J., Bazin, P.L., 2018. Nighres: processing tools for high-resolution neuroimaging. Gigascience 7, 1–9. https://doi.org/10.1093/gigascience/giy082

Hurley, A.C., Al-radaideh, A., Bai, L., Aickelin, U., Coxon, R., Glover, P., Gowland, P.A., 2010. Tailored RF pulse for magnetization inversion at ultrahigh field. Magn. Reson. Med. 63, 51–58. https://doi.org/10.1002/mrm.22167

Le Ster, C., Moreno, A., Mauconduit, F., Gras, V., Stirnberg, R., Poser, B.A., Vignaud, A., Eger, E., Dehaene, S., Meyniel, F., Boulant, N., 2019. Comparison of SMS-EPI and 3D-EPI at 7T in an fMRI localizer study with matched spatiotemporal resolution and homogenized excitation profiles. PLoS One 14, 1–17. https://doi.org/10.1371/journal.pone.0225286

Marques, J.P., Kober, T., Krueger, G., van der Zwaag, W., Van de Moortele, P.F., Gruetter, R., 2010. MP2RAGE, a self bias-field corrected sequence for improved segmentation and T1-mapping at high field. Neuroimage 49, 1271–1281. https://doi.org/10.1016/j.neuroimage.2009.10.002

Marques, J.P., Norris, D.G., 2018. How to choose the right MR sequence for your research question at 7 T and above? Neuroimage 168, 119–140. https://doi.org/10.1016/j.neuroimage.2017.04.044

Mauconduit, F., Massire, A., Gras, V., Amadon, A., Vignaud, A., Boulant, N., 2020. PASTeUR package extension with MP2RAGE for robust T1 mapping technique in parallel transmit at 7T, in: 2020 ISMRM & SMRT Virtual Conference & Exhibition.

Mugler, J.P., Brookeman, J.R., 1991. Rapid three-dimensional T1-weighted MR imaging with the MP-RAGE sequence. J. Magn. Reson. Imaging 1, 561–567. https://doi.org/10.1002/jmri.1880010509

Mugler, J.P., Brookeman, J.R., 1990. Three-dimensional magnetization-prepared rapid gradient-echo imaging (3D MP RAGE). Magn. Reson. Med. 15, 152–157. https://doi.org/10.1002/mrm.1910150117

O'Brien, K.R., Kober, T., Hagmann, P., Maeder, P., Marques, J., Lazeyras, F., Krueger, G., Roche, A., Brien, K.R.O., Kober, T., Hagmann, P., Maeder, P., Lazeyras, F., Krueger, G., Roche, A., 2014a. Robust T1-weighted structural brain imaging and morphometry at 7T using MP2RAGE. PLoS One 9. https://doi.org/10.1371/journal.pone.0099676

O'Brien, K.R., Magill, A.W., Delacoste, J., Marques, J.P., Kober, T., Fautz, H.P., Lazeyras, F., Krueger, G., Brien, K.R.O., Magill, A.W., Delacoste, J., Marques, J.P., Kober, T., Fautz, H.P.,

Lazeyras, F., Krueger, G., 2014b. Dielectric Pads and Low-B1+ Adiabatic Pulses: Complementary Techniques to Optimize Structural T1w Whole-Brain MP2RAGE Scans at 7 Tesla. J. Magn. Reson. Imaging 40, 804–812. https://doi.org/10.1002/jmri.24435

Okubo, G., Okada, Tomohisa, Yamamoto, A., Kanagaki, M., Fushimi, Y., Okada, Tsutomu, Murata, K., Togashi, K., 2016. MP2RAGE for deep gray matter measurement of the brain: A comparative study with MPRAGE. J. Magn. Reson. Imaging 43, 55–62. https://doi.org/10.1002/jmri.24960

Padormo, F., Beqiri, A., Hajnal, J. V., Malik, S.J., 2016. Parallel transmission for ultrahigh-field imaging. NMR Biomed. 29, 1145–1161. https://doi.org/10.1002/nbm.3313

R Core Team, 2020. A Language and Environment for Statistical Computing. R Found. Stat. Comput.

Rooney, W.D., Johnson, G., Li, X., Cohen, E.R., Kim, S.G., Ugurbil, K., Springer, C.S., 2007. Magnetic field and tissue dependencies of human brain longitudinal 1H2O relaxation in vivo. Magn. Reson. Med. 57, 308–318. https://doi.org/10.1002/mrm.21122

Roos, T., Knapen, T., van der Zwaag, W., 2019. Improving 7T brain scans for anatomical and functional modalities by reducing B1+ inhomogeneity; Pads or Universal Pulses? Proc. 36th Sci. Meet. Eur. Soc. Magn. Reson. Med. Biol.

Seiger, R., Hahn, A., Hummer, A., Kranz, G.S., Ganger, S., Küblböck, M., Kraus, C., Sladky, R., Kasper, S., Windischberger, C., Lanzenberger, R., 2015. Voxel-based morphometry at ultra-high fields. A comparison of 7T and 3T MRI data. Neuroimage 113, 207–216. https://doi.org/10.1016/j.neuroimage.2015.03.019

Van de Moortele, P.-F., Auerbach, E.J., Olman, C., Yacoub, E., Uğurbil, K., Moeller, S., 2009. T1 weighted brain images at 7 Tesla unbiased for Proton Density, T2□contrast and RF coil receive B1 sensitivity with simultaneous vessel visualization. Neuroimage 46, 432–446. https://doi.org/10.1016/j.neuroimage.2009.02.009

Wright, P.J., Mougin, O.E., Totman, J.J., Peters, A.M., Brookes, M.J., Coxon, R., Morris, P.E., Clemence, M., Francis, S.T., Bowtell, R.W., Gowland, P.A., Coxon, M.J.B.R., Clemence, P.E.M.M., Gowland, S.T.F.R.W.B.P.A., Wright, P.J., Mougin, O.E., Totman, J.J., Peters, A.M., Brookes, M.J., Coxon, R., Morris, P.E., Clemence, M., Francis, S.T., Bowtell, R.W., Gowland,

P.A., 2008. Water proton T1 measurements in brain tissue at 7, 3, and 1.5T using IR-EPI, IR-TSE, and MPRAGE: Results and optimization. Magn. Reson. Mater. Physics, Biol. Med. 21, 121–130. https://doi.org/10.1007/s10334-008-0104-8

Yan, S., Qian, T., Maréchal, B., Kober, T., Zhang, X., Zhu, J., Lei, J., Li, M., Jin, Z., 2020. Test-retest variability of brain morphometry analysis: an investigation of sequence and coil effects. Ann. Transl. Med. 8, 12–12. https://doi.org/10.21037/atm.2019.11.149

Chapter 3

Comparing hand movement rate dependence of cerebral blood volume and BOLD responses at 7T

Ícaro A.F. de Oliveira,

Wietske van der Zwaag,

Luisa Raimondo,

Serge O. Dumoulin,

Jeroen C.W. Siero

Based on the publication: Oliveira, Í.A.F., van der Zwaag, W., Raimondo, L., Dumoulin, S.O., Siero, J.C.W., 2021. Comparing hand movement rate dependence of cerebral blood volume and BOLD responses at 7T. Neuroimage 226, 117623. https://doi.org/10.1016/j.neuroimage.2020.117623

Abstract

Functional magnetic resonance imaging (fMRI) based on the Blood Oxygenation Level Dependent (BOLD) contrast takes advantage of the coupling between neuronal activity and the hemodynamics to allow a non-invasive localization of the neuronal activity. In general, fMRI experiments assume a linear relationship between neuronal activation and the observed hemodynamics. However, the relationship between BOLD responses, neuronal activity, and behaviour are often nonlinear. In addition, the nonlinearity between BOLD responses and behaviour may be related to neuronal process rather than a neurovascular uncoupling. Further, part of the nonlinearity may be driven by vascular nonlinearity effects in particular from large vessel contributions. fMRI based on cerebral blood volume (CBV), promises a higher microvascular specificity, potentially without vascular nonlinearity effects and reduced contamination of the large draining vessels compared to BOLD. In this study, we aimed to investigate differences in BOLD and VASO-CBV signal changes during a hand movement task over a broad range of movement rates. We used a double readout 3D-EPI sequence at 7T to simultaneously measure VASO-CBV and BOLD responses in the sensorimotor cortex. The measured BOLD and VASO-CBV responses increased very similarly in a nonlinear fashion, plateauing for movement rates larger than 1 Hz. Our findings show a tight relationship between BOLD and VASO-CBV responses, indicating that the overall interplay of CBV and BOLD responses are similar for the assessed range of movement rates. These results suggest that the observed nonlinearity of neuronal origin is already present in VASO-CBV measurements, and consequently shows relatively unchanged BOLD responses.

Introduction

Functional Magnetic Resonance Imaging (fMRI) is the most popular means of probing neuronal activity in living humans, with blood oxygenation level-dependent (BOLD) the most common non-invasive contrast used to detect brain function. The BOLD signal relies on T2 or T2* relaxation, which is sensitive to local concentrations of paramagnetic deoxyhemoglobin (dHb), which leads to alterations in MRI signal intensity (Kim and Ogawa, 2012).

The measured BOLD signal during functional activation depends predominantly on the changes in venous blood oxygenation, which in turn depends on the induced neurovascular, hemodynamic, and metabolic changes. When interpreting functional MRI signals, we generally assume a linear coupling between neuronal activation and the observed vascular signals (neurovascular coupling)(Boynton et al., 2012, 1996; Cohen, 1997; Friston et al., 1994; Heeger et al., 2000; Miezin et al., 2000). However, BOLD responses, neuronal activity, and behaviour are often nonlinearly coupled (Buxton et al., 2014; Friston et al., 2000; Hermes et al., 2012; Logothetis, 2008; Logothetis et al., 2001; Siero et al., 2013; Soltysik et al., 2004; Yeşilyurt et al., 2008).

Although the BOLD signal mechanism is complex, previous studies demonstrated the presence of both linear and nonlinear behaviour of the BOLD signal with task variations. For the visual cortex, it has been shown that the amplitude and duration of the BOLD response can be assumed to be linear for stimulus duration longer than 4 seconds (Boynton et al., 1996; Liu and Gao, 2000; Soltysik et al., 2004; Vazquez and Noll, 1998; Yeşilyurt et al., 2008). In contrast, a nonlinear scaling in amplitude and duration between stimulus and the BOLD signal has been observed, for example, in visual stimuli with a short duration (< 3-4 seconds). Here, BOLD response amplitude was larger than the prediction as expected from a linear system (Birn and Bandettini, 2005; Liu et al., 2010; Logothetis et al., 2001; Miller et al., 2001; Yeşilyurt et al., 2008; Zhang et al., 2009, 2008). Nonlinear behaviour was also observed for the BOLD response amplitude for a range of other fMRI experimental paradigms; word presentation rates (Büchel et al., 1998; Friston et al., 1998; Rees et al., 1997), visual stimuli with different frequency contrasts (Gaglianese et al., 2017). In the motor fMRI literature too, plateauing at high movement rates has been observed for different hand motor tasks (Jäncke et al., 1998; Khushu et al., 2001; Riecker et al., 2003; Sadato et al., 1997; Siero et al., 2013).

Several studies combined electrocorticography (ECoG) with BOLD fMRI showing a close to linear relationship between neuronal population activity measured by electrocorticography (ECoG) and BOLD responses with respect to different stimulus rates (Gaglianese et al., 2017; Siero et al., 2013). Specifically, in the sensorimotor cortex, Siero et al. showed that both the BOLD and neuronal ECoG responses plateau at high movement rates (≥ 1Hz). These findings corroborate to the suggestion that a significant part of the BOLD nonlinearity, i.e. plateauing of the response amplitude at high movement rates, has a neuronal origin (Birn and Bandettini, 2005; Zhang et al., 2009). The remaining part is likely due to vascular nonlinear effects such as vascular refractory effects where the response to a repeated stimulus can be diminished (Zhang et al., 2008). These effects are thought to occur in larger vessels that can exhibit inconsistent response delays due to pooling of upstream microvascular blood with different transit times (Zhang et al., 2009). Another potential source of vascular nonlinearities is the BOLD ceiling effect, where the maximum amount of BOLD signal is reached when the blood flow is increased to the point that all the deoxyhemoglobin (dHb) in the venous vasculature is washed out (Buxton et al., 2014).

Cerebral blood volume (CBV) measurements provide an alternative fMRI contrast mechanism to BOLD. The Vascular Space Occupancy (VASO) contrast is sensitive to arteriole and post-arterial CBV changes and promises higher microvascular specificity, thus better spatial localization of the neuronal activity with reduced draining vein contamination compared to BOLD (Hua et al., 2018; Huber et al., 2014; Jin and Kim, 2008; Lu et al., 2013, 2003). In VASO, the contrast is based on the differences between the longitudinal relaxation times (T1) of blood and tissue, and it is generated by nulling the blood signal using an inversion pulse while maintaining part of the tissue signal.

Although the linearity of the CBV response has, to date, not yet been investigated, the CBV responses are not expected to behave in the same fashion as the BOLD response to repeated stimuli and stimulus rate. Since VASO-CBV responses promise higher microvascular specificity, we might expect reduced vascular nonlinear effects as previously observed in BOLD fMRI experiments. Simultaneous assessment of CBV and BOLD responses can shed light on the extent of vascular nonlinear effects observed in the BOLD signal.

In this study, we measured simultaneously BOLD and VASO-CBV responses, using a double readout 3D-EPI VASO sequence, during the execution of hand digit movements at

several movement rates. The goal was to evaluate and compare the BOLD and VASO-CBV response behaviour with respect to movement rate in sensorimotor cortex.

Materials and methods

Subjects

Five healthy volunteers (age 25-40 years, two women and three men) without hand movement impairments participated in the study. The local ethics committee approved this study, and all volunteers provided written consent prior to participating after being informed of the experimental procedures.

Stimulus

Each subject repeated the experiment twice in two separate sessions, where the subjects performed the same motor task. The task consisted of moving the right hand periodically following a visual cue, from a rest position to a loosely clenched fist, at five different movement rates: ~0.33, 0.5, 1, 1.5, and 2 Hz. The visual cue was projected on a screen at the end of the bore of the scanner, which the subjects viewed using a mirror. The visual cue consisted of two different coloured squares (with the green square meaning move, and red indicating rest) alternating at the appropriate clenching rate and was generated in 'Matlab' (The MathWorks, Natick, United States) using the 'Psychophysics Toolbox Version 3'. Both task and movement rates have previously been shown to yield robust BOLD responses and nonlinearity with the stimulus rate (Siero et al., 2013).

The task paradigm consisted of a 30 second baseline, then alternating between 12 seconds of movement, and 24 seconds of rest. In total, 12 trials were performed per movement rate in a pseudo-randomized order across subjects and sessions. All subjects were briefly trained outside the scanner and instructed to use a constant force across movement rates. The hand movements were recorded using a DataGlove 5 Ultra MRI (Fifth Dimension Technologies 5DT, www.5dt.com) with a sampling rate of 120Hz. The right-hand dataglove is metal-free and consists of five fiber-optical sensors in total (one sensor per finger), placed on the back of each digit. These fiber-optical sensors provide an average measurement of the finger flexure for

each of the five fingers by measuring the optical fiber path length. Hence, with these sensors, fist-clenching can be observed clearly, but not the movement of individual phalanges or wrist rotations. The traces from the index, middle, ring and little fingers were averaged to verify the subject's movement rate and task performance. For an example recording, see Fig. 1. One subject's session was removed after the detection of motion-related artifacts, and the remaining 45 runs were included in the final analysis.

In order to eliminate bias in the comparison analysis between different movement rates we obtained the region of interest (ROI) from an additional stimulus run using the same paradigm described above, with 1.0 Hz and eight trials, the same processing steps were performed for all datasets including the functional localizer run.

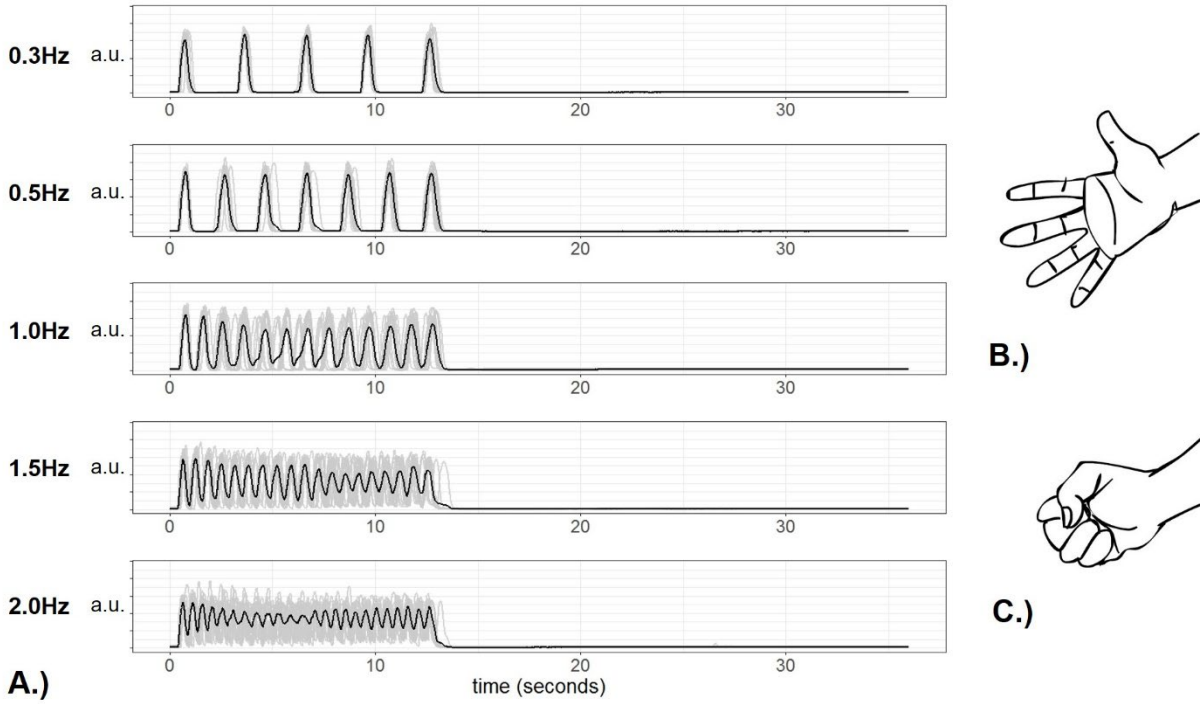

Fig. 1. A) Single-subject dataglove traces across 12 trials shown in gray with the average response in black. The subplots illustrate the functional paradigm and task performance. From top to bottom, hand movement rates ~0.33, 0.5, 1.0, 1.5, and 2 Hz, the hand movements were performed for 12 seconds, followed by 24 seconds of rest (baseline). The task consisted of moving the right hand from a rest position (B) to a loosely clenched fist position (C). The dataglove data was used to check for task performance and to calculate an accurate movement rate for each subject. Note that, for the highest movement rates (greater than 1.0Hz), the subjects accrued timing deviations in the executed movement onset with respect to the visual cue resulting in a reduced amplitude for the average movement trace (black).

MR sequences

Imaging was performed on a 7T MRI scanner (Philips Healthcare, Best, The Netherlands) using an 8 channel transmit coil and a 32 channel receive coil (Nova Medical Inc, Wilmington, United States) with a close to circularly polarized-mode achieved by B1-shimming of the entire brain of a group of volunteers. A Slice-Saturation Slab-Inversion (SS-SI) VASO scheme was used to simultaneously acquire CBV and BOLD weighted images using interleaved pair-wise 3D-EPI readouts (Huber et al., 2014) (Fig. 2). The timing parameters for the interleaved acquisition were based on previous 7T findings, taking into account gray matter (GM) and blood T_1 values, arterial arrival time in the sensorimotor cortex, and an additional margin as previously proposed (Huber et al., 2018). Combining these, we used $TI_1/TI_2/TE/TR$ = 1100/2600/17/3000 ms. For the magnetization inversion, we implemented an adiabatic inversion TR-FOCI pulse, which ensures an effective inversion with reduced B1+ inhomogeneity dependency compared to a more conventional hyperbolic secant adiabatic inversion pulse (Hurley et al., 2010). Data were acquired with an isotropic voxelsize of 1.5 mm, FOV = 192×192×21 mm^3, matrix size = 128×128, 14 slices, partial Fourier factor = 0.78 in the phase encoding direction and $SENSE_{inplane}$ factor = 2.5. 154 volumes were acquired per run, leading to a total scan time (per movement rate) of 7 minutes and 42 seconds.

In addition, a higher resolution T2*-weighted scan was acquired to identify the veins in the imaging area. A 3D multishot gradient-echo EPI was acquired with the following parameters: TR/TE = 67/29 ms, flip angle = 20°, averages = 2, SENSE factor = 2, isotropic voxelsize = 0.6 mm, and FOV = 215×160×75 mm^3, matrix size = 360×342. 100 slices were acquired to cover the sensorimotor cortex, with a total scan time of 2 minutes and 35 seconds.

Flip angle sweep

A 3D-EPI readout not only results in higher image SNR compared a 2D-EPI readout (Van Der Zwaag et al., 2012) but also leads to a reduced power deposition as typically smaller flip angles are used. In SS-SI VASO, longitudinal magnetization recovery during the 3D-EPI readouts leads to different T1-weightings along the k_z-direction, which can result in blurring across slices. To reduce this blurring, we modulated the flip angle train, such that the

magnetization in the gray matter remains approximately constant (Gai et al., 2011). The nominal flip angles in the optimal sweep were: 14.4°, 14.9°, 15.4°, 15.9°, 16.5°, 17.2°, 17.9°, 18.7°, 19.6°, 20.6°, 21.8°, 23.2°, 25.0°, 27.1°, 30.0° (Fig. 2). The SAR values never exceeded 2 W/kg (or 20% of the local SAR limit), according to the SAR estimation of the vendor.

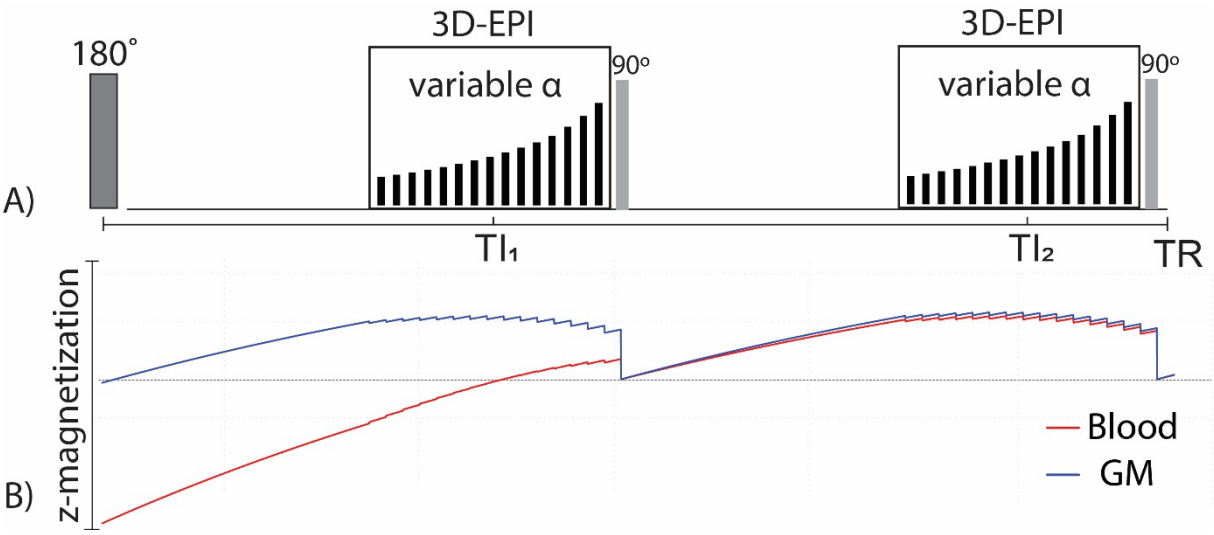

Fig. 2. Depicted pulse sequence (sequence diagram) combined with the z-magnetization during a 3D-EPI Slice-Selective Slab-Inversion (SS-SI) VASO acquisition. A) An adiabatic inversion (180°) pulse (TR-FOCI) followed by two acquisition modules with 3D-EPI readout with a variable flip angle (α). Inversion times TI_1, TI_2, and volume repetition time TR were 1100, 2600, and 3000 ms, respectively. B) In SS-SI VASO, an increase in tissue signal is realized by manipulating the longitudinal magnetization of the stationary gray matter (GM) tissue separately from the inflowing blood. Here, a 90° magnetization reset pulse is applied in the imaging slab after both readout modules, resulting in an increased available tissue signal.

Data analysis

All data pre-processing was performed using the SPM12 (Statistical Parametric Mapping) software package. We first performed a motion correction for BOLD and VASO images separately, followed by a BOLD correction used to minimize the extravascular BOLD signal contamination present in the VASO images (Huber et al., 2014). No additional spatial smoothing or temporal filtering was applied to minimize loss in specificity. T2*-weighted images were registered to the same space as the functional data, and all movement rate data sets were registered to the same common space, per subject using the functional localizer as reference.

The ROI definitions were based on VASO-CBV and BOLD activated voxels from the localizer run. After a GLM (FEAT in FSL, v.6.0) analysis, the VASO-CBV and BOLD Z-statistic activation maps were thresholded at a Z-statistic value = 2.5. To assess signals originating from draining veins, we created a "vessel ROI" based on the high-resolution T2*-weighted image, where low signal intensity spots indicate the larger draining veins, and the overlap with the BOLD activation map. To account for the extravascular BOLD signal extent of the draining vein, voxels adjacent to the large vessels were also included in the ROI (Fig. 3C, D in red) (Siero et al., 2011). A second ROI was created based on the BOLD activation map, but excluding the overlapped voxels from the vessel ROI, resulting in a "BOLD non-Vessel ROI" (BnV ROI, Fig. 3C, D in blue). The final ROI was defined as the common set of CBV and BOLD activated voxels, also excluding voxels from the vessel ROI, which we will dub "CBV BOLD Combined non-Vessel ROI" (CBnV ROI). (Fig. 3C, D in green).

To investigate the response linearity with respect to the movement rate, we first averaged the time courses of all voxels within each ROI. Next, we obtained CBV and BOLD percentage signal changes for all subjects and movement rates. To evaluate the relationship between VASO-CBV and BOLD responses in the different ROIs, we ran a linear regression on the percent signal changes per session and movement rates; five CBV-BOLD pairs of data points (per session, at five movement rates) were entered into the regression model, in total, nine slopes and intercepts were generated and further averaged. This procedure followed what was proposed in (Makin and De Xivry, 2019). One-way ANOVAs with Tukey *post-hoc* analyses were used to assess the slope and intercept differences between ROIs. All generated plots, linear regression and ANOVA estimation, were performed using R (R Development Core, 2008), where p-values < 0.05 were considered statistically significant.

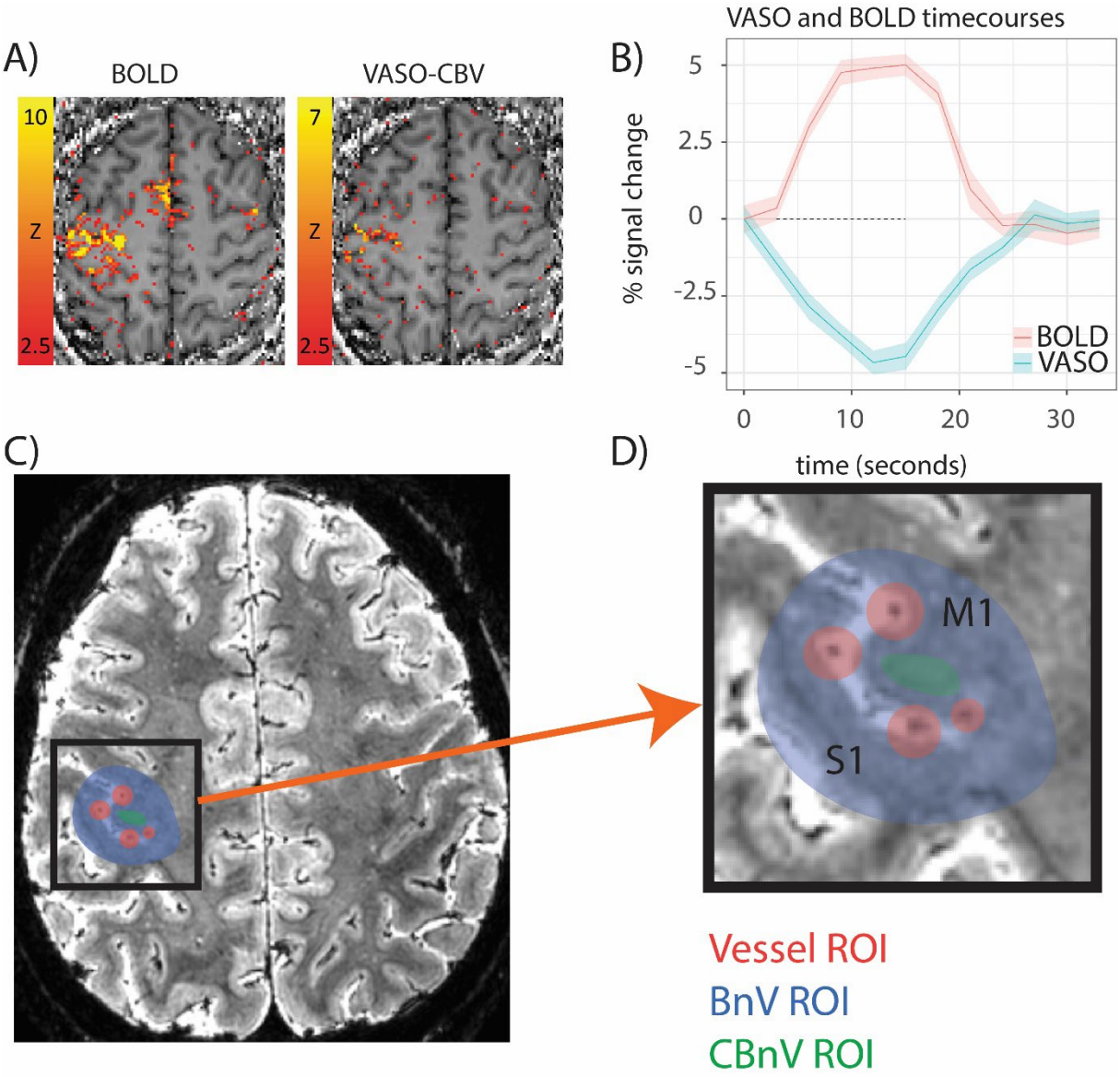

Fig. 3. Example BOLD and VASO-CBV-weighted activation maps with their respective signal amplitudes, followed by the ROI selection outline. A) shows BOLD and VASO-CBV activation maps from the functional localizer run for a representative subject, and B) signal timecourses averaged across all subjects, extracted from the ROIs used in the analysis (e.g. BnV for BOLD timecourse and CBnV for VASO timecourse). The dashed line represents the stimulation period, and the transparent shaded area represents the standard error across subjects. In C) and D), a T2*-weighted image is shown with a schematic of the three different ROIs. In red, delineation of draining veins incorporating a BOLD extravascular signal extent (Vessel ROI). In blue, the "BOLD non-Vessel" (BnV ROI), based on BOLD activated voxels, excluding the voxels from the vessel ROI. In green, the "CBV BOLD Combined non-Vessel" (CBnV ROI), i.e. a common set of BOLD and CBV activated voxels, also excluding Vessel ROI voxels.

Results

Fig. 1 shows the averaged dataglove response of one representative subject and illustrates the functional paradigm and associated task performance. We assessed the dataglove responses and calculated the execute movement rate for all runs. The dataglove shows that the subjects' performance was similar between the movement rates, even for higher movement rates (> 1 Hz), where the responses start to reduce in amplitude, but the movement rate still matches with those introduced by the stimuli. Hand movements were executed within 0.337 ± 0.002 Hz, 0.505 ± 0.030 Hz, 1.002 ± 0.026 Hz, 1.523 ± 0.025 Hz, and 1.978 ± 0.114 Hz.

Robust BOLD and VASO-CBV responses in the sensorimotor cortex were detected in all participant sessions for all five different movement rates. Fig. 3A shows exemplar BOLD and VASO-CBV activation maps for a representative subject, and Fig. 3B the signal timecourses averaged across subjects. Fig. 4 shows the average VASO-CBV and BOLD percentage signal changes with respect to movement rate for the different ROIs. Both the BOLD and VASO-CBV response amplitude show an increase for movement rates till 1 Hz and plateaus for higher movement rates ≥ 1 Hz. As expected, the BOLD response amplitude was much higher in the vessel ROI than in the other two ROIs. VASO-CBV response amplitudes were higher in the combined ROI (CBnV ROI) than in the BnV ROI because of the way both ROIs had been defined. Interestingly, VASO-CBV responses were also significant in the vessel ROI, albeit more modest than the increase in BOLD compared to the BnV and CBnV ROIs. In addition, the VASO-CBV contrast-to-noise ratio (CNR) was approximately 56% of BOLD CNR for the CBnV ROI, calculated using the average percentage signal change across all subjects.

In Fig. 5, a linear regression was used to assess the linearity of the relationship between VASO-CBV and BOLD responses in the three different ROIs. For all ROIs and subjects, a significant linear relationship was found between the movement rate dependent BOLD and VASO-CBV responses. The following results are the average slopes, intercepts and the Pearson's correlations across subjects and movement rates. For the vessel ROI, slope = 0.95 ± 0.10 %BOLD/%VASO-CBV, intercept = 2.20 ± 0.12 %BOLD and the R = 0.77, for the BnV ROI, slope = 1.18 ± 0.05 %BOLD/%VASO-CBV, intercept = 1.13 ± 0.07 %BOLD and the R = 0.89, and finally for the CBnV ROI, slope = 0.90 ± 0.12 %BOLD/%VASO-CBV, intercept = 1.10 ± 0.28

%BOLD and R = 0.80. The fitted linear curves are depicted in Fig. 5 for all ROIs per session; the dashed line represents the average of all nine sessions. Note that all the fitted slopes are relatively close to 1 and did not significantly differ between ROIs, as the one-way ANOVA with Tukey post-hoc analysis revealed, $ROI_{vessel\text{-}BnV}$, p=0.26, $ROI_{vessel\text{-}CBnV}$, p=0.93 and $ROI_{BnV\text{-}CBnV}$, p=0.14. Interestingly, there is a significant offset, i.e. a non-zero BOLD-intercept, at VASO CBV (%) = 0, for all ROIs. The intercept value was significantly higher for the Vessel ROI compared to both the BnV and CBnV ROIs (both p=0.001), while the BnV and CBnV ROIs had a similar intercept value (p=0.9).

We also investigated the cerebrospinal fluid (CSF) contribution in the Vessel ROI. We correlated the brightness of the mean EPI from each subject, with the percentage signal change in the vessel ROI to investigate the relationship between CSF and VASO-CBV signal. The brightest voxels in the mean EPI indicates the presence of a high voxel CSF content due to the long T1 and T2* of CSF. Lower intensity voxels generally indicate larger venous content (shorter T1 and T2* for venous blood). A positive correlation would indicate that voxels with a high percentage of VASO-CBV signal change are related to the voxels with a large partial volume contribution of CSF. We found that the correlation for the VASO-CBV signal changes are much closer to 0 and not consistently negative or positive (i.e. non-significantly different from 0, $p = 0.44$), suggesting that the impact of the draining veins and CSF content is on the response amplitude is small. The results for the BOLD response amplitude, however, showed a significant negative correlation ($p = 7.71 \times 10^{-8}$) for all movement rates, indicating higher BOLD signal changes for voxels with higher venous blood content, as expected.

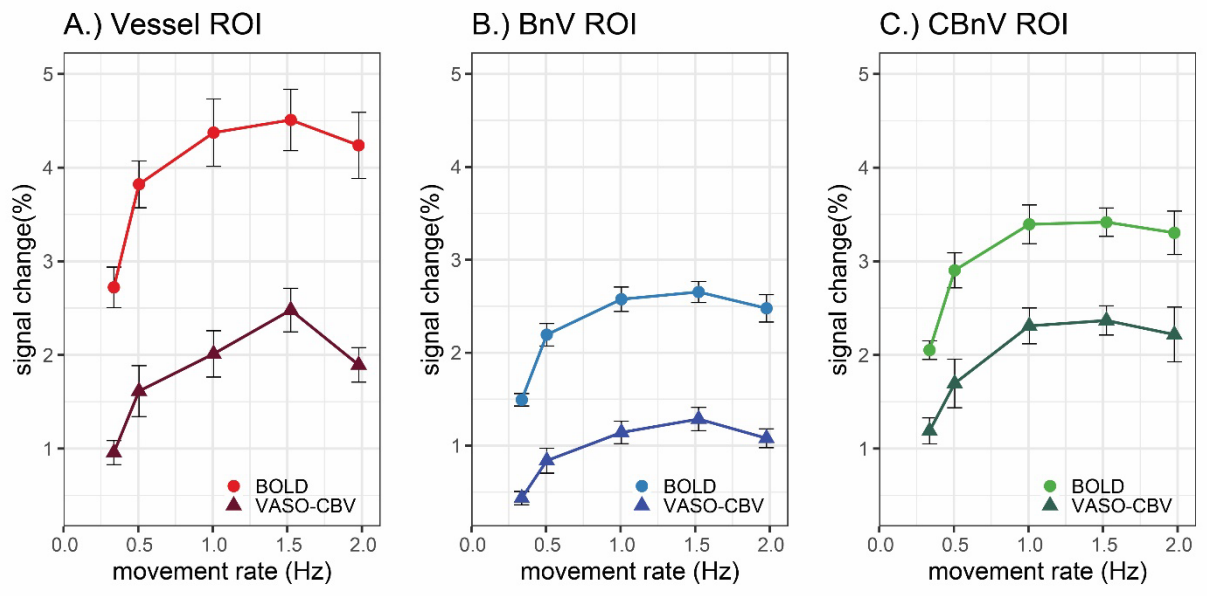

Fig. 4. The BOLD and VASO-CBV percent signal change with respect to movement rate for the different ROIs, averaged across subjects. A.) Vessel ROI, B.) The "BOLD non-Vessel" (BnV ROI), and C.) The "CBV BOLD Combined non-Vessel" (CBnV ROI, i.e. common CBV and BOLD activated voxels). The higher sensitivity of BOLD compared with VASO-CBV is reflected in the higher percentage signal change. The error bars are the standard error. Regardless of the ROI, both BOLD and VASO-CBV percentage signal change show similar behaviour, with both increasing in a linear fashion for movement rates < 1 Hz and saturating for movement rates ≥ 1 Hz.

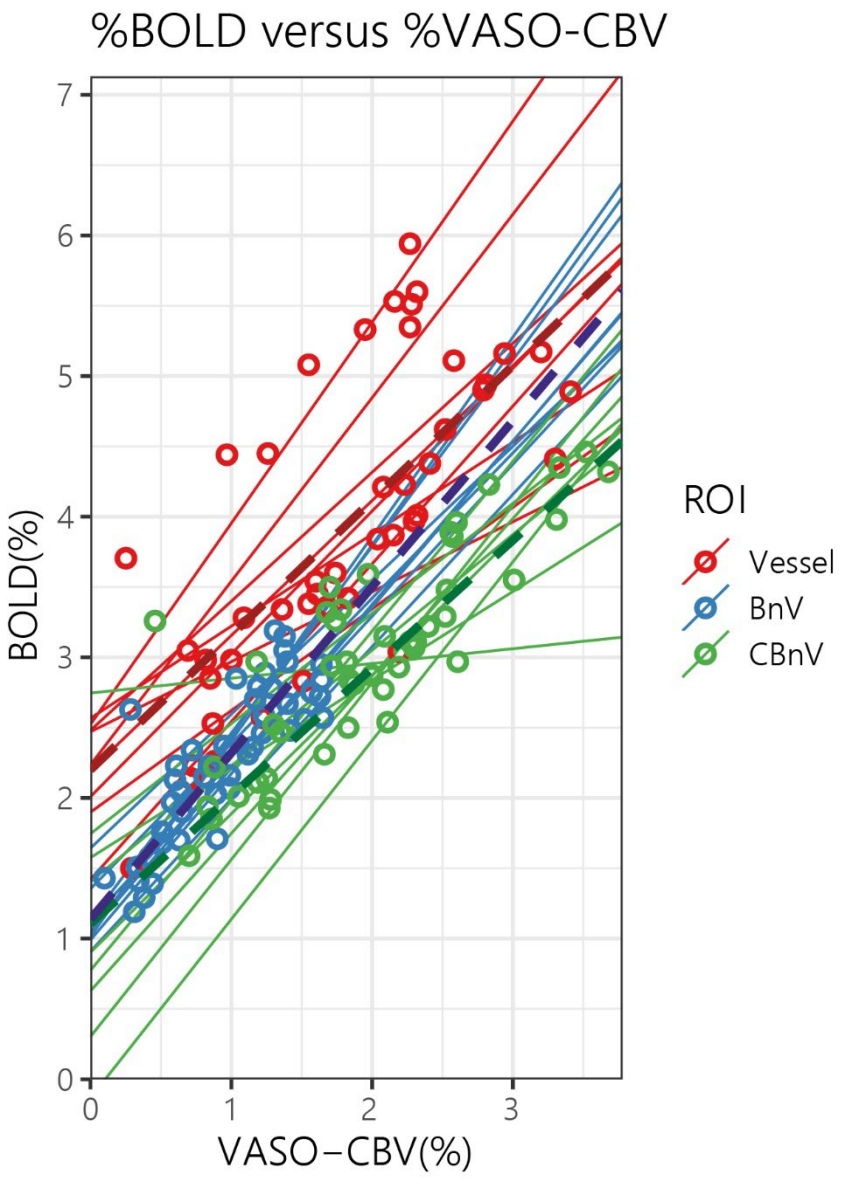

Fig. 5. %BOLD versus %VASO-CBV for different ROIs, showing the linear trend in the relationship between both measured responses for all movement rates. Each line represents the slope of %BOLD versus %VASO-CBV for all movement rates (open circles) of a single session, and the dashed lines represent the average slope across all sessions. In red, the draining vein or "vessel" ROI. In blue, the "BOLD non-Vessel" (BnV) ROI; based on BOLD activated voxels, excluding the voxels contained in the vessel ROI. In green, the "CBV BOLD Combined non-Vessel" ROI (CBnV ROI), i.e. the common set of BOLD and VASO-CBV activated voxels excluding vessels.

Discussion

In the present study, we evaluated the relationship between 7T BOLD and VASO-CBV fMRI responses for a simple motor task with five different hand movement rates. A double

readout 3D-EPI VASO sequence enabled us to acquire BOLD and CBV responses rates in sensorimotor cortex simultaneously. As the CBV and BOLD contrast are thought to have distinct weighting for (micro)vascular compartments, we anticipated distinct response behaviour with respect to movement rate. Interestingly, we found a high degree of similarity between BOLD and CBV response behaviour regarding movement rate.

Observed VASO-CBV activation patterns (Fig. 3A) are similar in magnitude and spatial extent to previous studies using the same spatial resolution in sensorimotor cortex, showing reduced large draining vessel activations compared to the BOLD activation patterns (Huber et al., 2018, 2014). The relative sensitivity differences between VASO-CBV and BOLD was also in agreement with previous work (Huber et al., 2014). For the CBV BOLD Combined non-Vessel ROI (CBnV ROI), the VASO CBV contrast-to-noise ratio (CNR) was approximately 56% of BOLD CNR.

We found that the BOLD response first increases and then plateaus for movement rates ≥ 1 Hz. Interestingly, the CBV response showed a markedly similar response behaviour as the BOLD response for all ROIs (Fig. 4). Several fMRI studies have described movement frequency dependency in sensorimotor areas and other areas such as basal ganglia, cerebellum and spinal cord (Agnew et al., 2004; Jäncke et al., 1998; Maieron et al., 2007; Rao et al., 1996). In addition, electrophysiology studies have shown evidence for a negative relationship between motor cortex neuronal firing rate and movement frequency: greater speed of movement was associated with a reduced number of spikes/second in primates (Aflalo and Graziano, 2007). This notion is in agreement with human electrophysiology (ECoG) studies which observed that the plateauing could be associated with strongly reduced neuronal population activity (high-frequency gamma-band power) for fast movement rates after the very first movement. Moreover, the beta-band power remained suppressed, indicating a release of motor cortex inhibition, in a sense facilitating movement initiation for these fast movement rates (Hermes et al., 2012; Siero et al., 2013).

Plateauing of the BOLD response has been observed in sensorimotor cortex using a range of task designs such as finger tapping, button-pressing or hand movements (Jäncke et al., 1998; Khushu et al., 2001; Riecker et al., 2003; Sadato et al., 1997; Siero et al., 2013). In all cases, response plateauing was observed at high movement rates with a variation in the exact range of frequencies, differences that are likely related to the different experimental designs.

Interestingly, the observed VASO-CBV signal changes in the vessel ROI were comparable to the VASO-CBV signal changes in the CBnV ROI and higher than the BnV ROI. A possible explanation could be a partial volume effect from cerebrospinal fluid (CSF) (Donahue et al., 2006; Huber et al., 2015). The CSF signal is much higher than the gray matter signal for the used SS-SI-VASO scan parameters. Thus, for a similar displacement of the voxel's content by vascular dilation and/or adjacent tissue swelling, the signal intensity is reduced much more for high CSF content voxel than for low CSF content voxel. We investigated the CSF contamination by performing a voxelwise correlation between the mean EPI signal intensity and %VASO-CBV and %BOLD signal changes. While we found a negative correlation in the BOLD data confirming the importance of veins in this ROI, no such correlation was found for the VASO-CBV contrast, indicating minimal CSF contamination in the vessel ROI. The result of the correlation analysis are shown in the supplementary material (Suppl. Fig. 1.). However, other potential confounders could also explain the unexpected vessel ROI VASO CBV signal change. Previous studies reported that VASO fMRI is expected to capture CBV changes in small pial arteries (Donahue et al., 2006; Huber et al., 2015). Small pial arteries are most likely present in the vessel ROI but exhibit no image contrast, as the pial veins do, with respect to the CSF and gray matter signal. We also checked the VASO-CBV percentage signal change in the vessel ROI and the CBnV ROI when omitting the BOLD contamination correction. The results are shown in the supplementary material (Suppl. Fig 2.). As expected, the VASO-CBV responses are reduced when omitting the BOLD contamination correction. The amplitude for the non-BOLD corrected vessel ROI responses are comparable to the non-BOLD corrected CBnV ROI responses for all frequencies besides 1.5Hz, similar to the corrected data. Hence, any BOLD contamination is not likely to be the cause of the comparable response amplitude for the vessel ROI with respect to the CBnV ROI.

The observed tight relationship between BOLD and VASO-CBV responses for all ROIs indicates that blood volume changes are strongly associated to changes in deoxyhemoglobin, at least over the range of examined movement rates. This can also be seen in the scatter plot and fitted linear equations depicted in Fig. 5, showing a high correlation between %BOLD and %VASO-CBV changes and an almost one-to-one relationship as seen from the fitted slopes for all ROIs. Interestingly, we observed a non-zero intercept for the fitted linear equations describing the %BOLD versus %VASO-CBV all ROIs. At first instance, a zero-intercept would be expected, meaning that in the absence of a notable CBV change, a zero % BOLD signal change

would be observed. The observed non-zero BOLD intercept, though, could be remaining extravascular BOLD signal in the VASO-CBV data, i.e. residual BOLD contamination. Both BOLD and VASO-CBV readouts have similar T2* weighting, in this case, the positive BOLD signal changes cancel some of the negative VASO-CBV signal changes during activation. Most of this T2* or BOLD contamination is expected to be removed from the generated VASO-CBV images using a BOLD correction scheme (Huber et al., 2014); however, remaining contamination cannot be fully ruled out. It is worth pointing out that the BOLD correction scheme has been validated by at least two different designs, in both cases, correcting major part of the BOLD contamination with minimal overestimation of VASO-CBV signal changes (Huber, 2015). Another possibility is that the BOLD intercept reflects an (intracortical) draining vein effect, which is presumably not present in the VASO-CBV data but likely is present in the BOLD data, even after masking out the largest vessels visible on the high-resolution T2* anatomy image. Note that the intercept was the highest for the Vessel ROI.

The nonlinear behaviour observed in both the BOLD and VASO-CBV responses regarding movement rate is most likely, and for the most part, explained by the neuronal source (Hermes et al., 2012; Siero et al., 2013). The remaining part is probably of vascular origin and caused by vascular nonlinearity effects such as vascular refractory effects and the ceiling phenomenon. The ceiling effect could potentially be the cause of the BOLD nonlinearity, as suggested previously (Birn and Bandettini, 2005; Bruhn et al., 1994; Buxton et al., 2004). However, other fMRI modalities such as CBF mapping using Arterial Spin Labelling (ASL) have found a comparable nonlinear response with respect to different stimulus duration, and a linear relationship between CBF and BOLD (Miller et al., 2001), which are also similar to previous PET studies (Blinkenberg et al., 1996; Dettmers et al., 1996; Sadato et al., 1997). Our CBV findings complement these previous findings, and together they suggest that there is a minimal contribution of the ceiling effect in the BOLD nonlinearity since BOLD response is driven by CBF and CBV changes (Buxton et al., 2014). A plausible explanation for the VASO-CBV nonlinearities is that the CBV measurements reflect the nonlinear transformation from the stimulus to the neural response since CBV are closely related to the underlying neuronal activity. Consequently, the BOLD nonlinearities could be an extension of that, as the CBV nonlinearities are also part of the BOLD responses.

We observed a lower sensitivity for VASO-CBV responses, VASO-CBV CNR was about 56% compared to the BOLD CNR. The higher sensitivity is expected for GE-BOLD due to the nature of the contrast mechanism. In addition, residual signals from macrovessels or signals from non-specific large draining veins, can increase the observed BOLD CNR (Huber et al., 2017; Uludağ and Blinder, 2016). With respect to the sequence used here, the SS-SI 3D-EPI sequence provides simultaneous acquisition of VASO-CBV and BOLD fMRI measurements, however, care should be taken regarding the comparison and interpretation. An optimal VASO sequence requires careful adjustment of timing parameters; an appropriate inversion time that is not too long to avoid inflow effects, and a long TR to satisfy the VASO blood refilling conditions; usually TR = 3 s or longer to allow blood to refill the vasculature in the imaging volume but also to allow leaving the imaging volume before the next inversion pulse (Huber et al., 2014; Jin and Kim, 2008). In addition, a short TE is required to minimize BOLD contamination. In contrast, an optimal GE-BOLD sequence requires a relatively longer TE, and the TR is usually limited by the coverage of the field of view. Thus, the current TR restriction of the optimal SS-SI 3D-EPI VASO limits a more thorough investigation of the temporal features of the hemodynamic response and the neurovascular coupling. Methods like Multiple Acquisitions with Global Inversion Cycling (MAGIC) (Lu et al., 2004; Scouten and Constable, 2007) and the more recently Multiple Acquisitions with Global Excitation Cycling (MAGEC) (Huber et al., 2020) can achieve whole-brain coverage and, therefore, be used to increase the temporal resolution in future VASO studies.

Conclusion

We observed a strong linear relationship between VASO-CBV and BOLD responses, both similarly increasing with increasing hand movement rate and plateauing at high movement rates ≥ 1 Hz. The presumed higher microvascular specificity of VASO-CBV compared to BOLD does not directly result in a more linear response behaviour at high hand movement rates. The observed plateau behaviour, i.e. nonlinear effects, regarding movement rate, are likely predominantly of neuronal origin and therefore present in both the VASO-CBV and BOLD response.

Supplementary material

The VASO-CBV percentage signal changes in the vessel ROI were comparable to the "CBV BOLD Combined non-Vessel" ROI (CBnV ROI) and higher than the "BOLD non-Vessel" ROI (BnV ROI). To investigate the potential cause of the comparable VASO-CBV response amplitude in the vessel ROI, we assessed 1) a partial volume effect caused by cerebrospinal fluid (CSF) in voxels in the vessel ROI as these are predominantly located near the pial surface. And 2) the non-BOLD corrected VASO-CBV responses in the vessel ROI and the CBnV ROI.

1.) CSF partial volume effect

We also investigated the cerebrospinal fluid (CSF) contribution. We correlated the brightness of the mean EPI image of the second inversion time from each subject, with the percentage signal change for the voxels in the vessel ROI to investigate the relationship between CSF content and the VASO-CBV signal. The results (correlations over all subjects and movement rates) are summarized below in the boxplot for both the VASO-CBV and BOLD percentage signal change. The brightest voxels in the mean EPI indicates the presence of a high voxel CSF content due to the long T1 and T2* of CSF. Low-intensity voxels generally indicate larger venous content (shorter T1 and T2* for venous blood). A positive correlation would indicate that voxels with a high percentage of VASO-CBV signal change are related to the voxels with a large partial volume contribution of CSF. However, we found that the correlation for the VASO-CBV signal changes are much closer to 0 and not consistently negative or positive (i.e. non-significantly different from 0, ($p = 0.44$), suggesting that the impact of the draining veins and CSF content is on the response amplitude is small. The results for the BOLD response amplitude, however, showed a significant negative correlation ($p = 7.71 \times 10^{-8}$) for all movement rates, indicating higher BOLD signal changes for voxels with higher venous content, as expected.

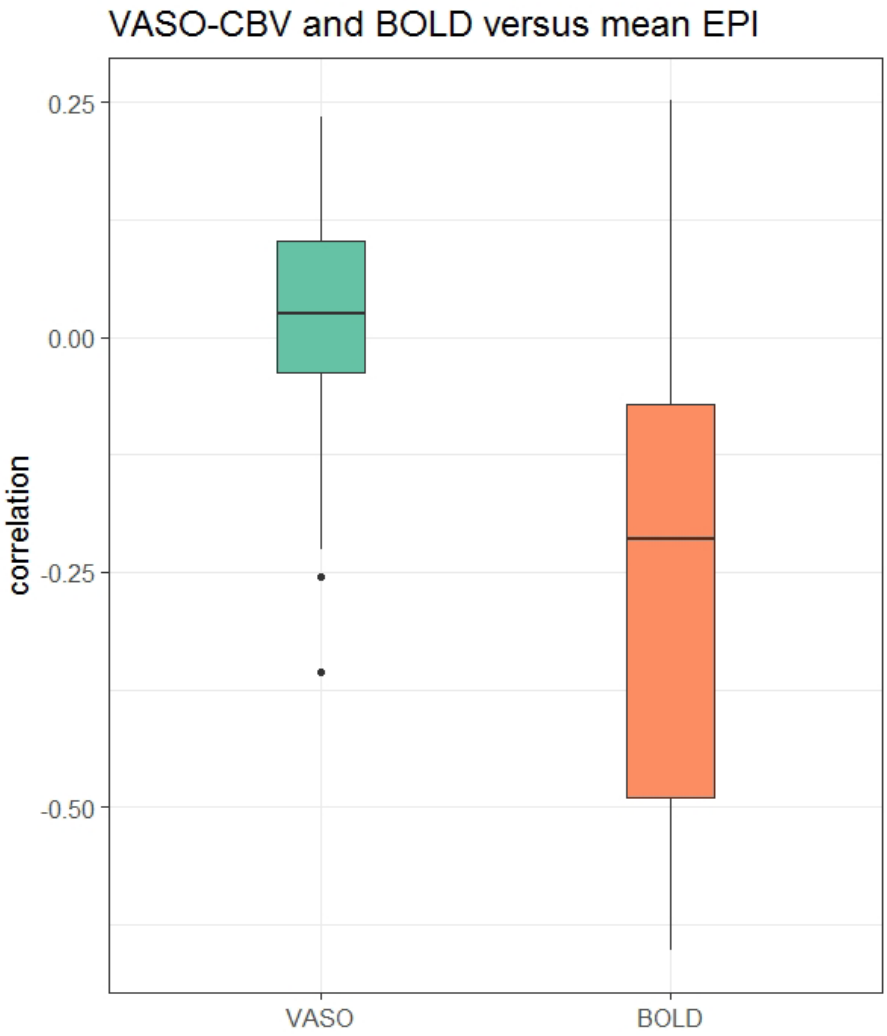

Supplemental Fig. 1. Boxplot showing the voxelwise correlations (over all subjects and movement rates) between the mean EPI image signal intensity and the VASO-CBV percentage signal change (in green) and the BOLD percentage signal change (in orange), respectively. The VASO-CBV correlations are not significantly different from 0 ($p = 0.44$), suggesting that there is no clear tendency for the CSF-rich voxels to drive the responses and that the influence of pial veins is small. For the BOLD data, we observed a significant negative correlation ($p = 7.71 \times 10^{-8}$) for all movement rates, indicating higher BOLD signal changes for voxels with higher venous blood content.

2.) BOLD correction scheme

To investigate the effect made by the BOLD correction step, we assessed the non-BOLD corrected VASO-CBV responses in the vessel ROI and the CBnV ROI (see Supplemental Figure 2 below). As expected, the VASO-CBV responses are reduced when omitting the BOLD

contamination correction. The amplitude for the non-BOLD corrected vessel ROI responses is comparable to the non-BOLD corrected CBnV ROI responses for all frequencies besides 1.5Hz, similar to the corrected data. Hence, any BOLD contamination is not likely to be the cause of the comparable response amplitude for the vessel ROI with respect to the CBnV ROI.

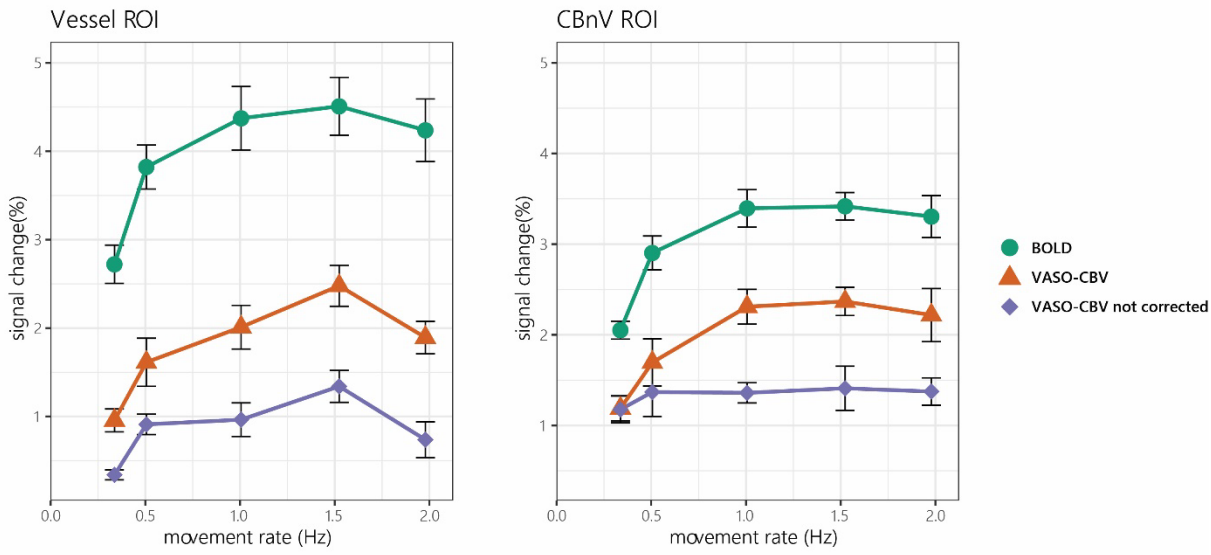

Supplemental Fig. 2. BOLD and VASO-CBV percentage signal change with respect to the movement rate for two ROIs; the "Vessel ROI" and the "CBV BOLD Combined non-Vessel" ROI (CBnV ROI), averaged across subjects. As expected, omitting the BOLD contamination correction scheme reduced the VASO-CBV response amplitude. The non-BOLD corrected VASO-CBV signal changes are comparable to the non-BOLD corrected CBnV ROI signal changes for all frequencies besides 1.5Hz, similar to the corrected data. In the figure legend, "VASO-CBV not corrected" correspond to the VASO-CBV data when the BOLD contamination correction scheme is omitted.

References

Aflalo, T.N., Graziano, M.S.A., 2007. Relationship between Unconstrained Arm Movements and Single-Neuron Firing in the Macaque Motor Cortex. J. Neurosci. 27, 2760–2780. https://doi.org/10.1523/JNEUROSCI.3147-06.2007

Agnew, J.A., Zeffiro, T.A., Eden, G.F., 2004. Left hemisphere specialization for the control of voluntary movement rate. Neuroimage 22, 289–303. https://doi.org/10.1016/j.neuroimage.2003.12.038

Birn, R.M., Bandettini, P.A., 2005. The effect of stimulus duty cycle and "off" duration on BOLD response linearity. Neuroimage 27, 70–82. https://doi.org/10.1016/j.neuroimage.2005.03.040

Blinkenberg, M., Bonde, C., Holm, S., Svarer, C., Andersen, J., Paulson, O.B., Law, I., 1996. Rate dependence of regional cerebral activation during performance of a repetitive motor task: A PET study. J. Cereb. Blood Flow Metab. 16, 794–803. https://doi.org/10.1097/00004647-199609000-00004

Boynton, G.M., Engel, S.A., Glover, G.H., Heeger, D.J., 1996. Linear systems analysis of functional magnetic resonance imaging in human V1. J. Neurosci. 16, 4207–4221. https://doi.org/10.1523/jneurosci.16-13-04207.1996

Boynton, G.M., Engel, S.A., Heeger, D.J., 2012. Linear systems analysis of the fMRI signal. Neuroimage 62, 975–984. https://doi.org/10.1016/j.neuroimage.2012.01.082

Bruhn, H., Kleinschmidt, A., Boecker, H., Merboldt, K.-D., Hänicke, W., Frahm, J., 1994. The Effect of Acetazolamide on Regional Cerebral Blood Oxygenation at Rest and under Stimulation as Assessed by MRI. J. Cereb. Blood Flow Metab. 14, 742–748. https://doi.org/10.1038/jcbfm.1994.95

Büchel, C., Holmes, A.P., Rees, G., Friston, K.J., 1998. Characterizing Stimulus–Response Functions Using Nonlinear Regressors in Parametric fMRI Experiments. Neuroimage 8, 140–148. https://doi.org/10.1006/nimg.1998.0351

Buxton, R.B., Griffeth, V.E.M.M., Simon, A.B., Moradi, F., 2014. Variability of the coupling of blood flow and oxygen metabolism responses in the brain: A problem for interpreting BOLD

studies but potentially a new window on the underlying neural activity. Front. Neurosci. 8, 1–6. https://doi.org/10.3389/fnins.2014.00139

Buxton, R.B., Uludağ, K., Dubowitz, D.J., Liu, T.T., 2004. Modeling the hemodynamic response to brain activation. Neuroimage 23, S220–S233. https://doi.org/10.1016/j.neuroimage.2004.07.013

Cohen, M.S., 1997. Parametric Analysis of fMRI Data Using Linear Systems Methods. Neuroimage 6, 93–103. https://doi.org/10.1006/nimg.1997.0278

Dettmers, C., Connelly, A., Stephan, K.M., Turner, R., Friston, K.J., Frackowiak, R.S.J., Gadian, D.G., 1996. Quantitative comparison of functional magnetic resonance imaging with positron emission tomography using a force-related paradigm. Neuroimage 4, 201–209. https://doi.org/10.1006/nimg.1996.0071

Donahue, M.J., Lu, H., Jones, C.K., Edden, R.A.E., Pekar, J.J., Van Zijl, P.C.M., Zijl, P.C.M. Van, Van Zijl, P.C.M., 2006. Theoretical and experimental investigation of the VASO contrast mechanism. Magn. Reson. Med. 56, 1261–1273. https://doi.org/10.1002/mrm.21072

Friston, K.J., Jezzard, P., Turner, R., 1994. Analysis of functional MRI time-series. Hum. Brain Mapp. 1, 153–171. https://doi.org/10.1002/hbm.460010207

Friston, K.J., Josephs, O., Rees, G., Turner, R., 1998. Nonlinear event-related responses in fMRI. Magn. Reson. Med. 39, 41–52. https://doi.org/10.1002/mrm.1910390109

Friston, K.J., Mechelli, A., Turner, R., Price, C.J., 2000. Nonlinear Responses in fMRI: The Balloon Model, Volterra Kernels, and Other Hemodynamics. Neuroimage 12, 466–477. https://doi.org/10.1006/nimg.2000.0630

Gaglianese, A., Vansteensel, M.J., Harvey, B.M., Dumoulin, S.O., Petridou, N., Ramsey, N.F., 2017. Correspondence between fMRI and electrophysiology during visual motion processing in human MT+. Neuroimage 155, 480–489. https://doi.org/10.1016/j.neuroimage.2017.04.007

Gai, N.D., Talagala, S.L., Butman, J.A., 2011. Whole-brain cerebral blood flow mapping using 3D echo planar imaging and pulsed arterial tagging. J. Magn. Reson. Imaging 33, 287–295. https://doi.org/10.1002/jmri.22437

Heeger, D.J., Huk, A.C., Geisler, W.S., Albrecht, D.G., 2000. Spikes versus BOLD: what does neuroimaging tell us about neuronal activity? Nat. Neurosci. 3, 631–633. https://doi.org/10.1038/76572

Hermes, D., Siero, J.C.W., Aarnoutse, E.J., Leijten, F.S.S., Petridou, N., Ramsey, N.F., 2012. Dissociation between Neuronal Activity in Sensorimotor Cortex and Hand Movement Revealed as a Function of Movement Rate. J. Neurosci. 32, 9736–9744. https://doi.org/10.1523/JNEUROSCI.0357-12.2012

Hua, J., Liu, P., Kim, T., Donahue, M., Rane, S., Chen, J.J., Qin, Q., Kim, S.G., 2018. MRI techniques to measure arterial and venous cerebral blood volume. Neuroimage 1–15. https://doi.org/10.1016/j.neuroimage.2018.02.027

Huber, L., 2015. Mapping human brain activity by functional magnetic resonance imaging of blood volume. PhD thesis. University of Leipzig.

Huber, L., Finn, E.S., Chai, Y., Goebel, R., Stirnberg, R., Stöcker, T., Marrett, S., Uludag, K., Kim, S.G., Han, S., Bandettini, P.A., Poser, B.A., 2020. Layer-dependent functional connectivity methods. Prog. Neurobiol. 101835. https://doi.org/10.1016/j.pneurobio.2020.101835

Huber, L., Goense, J., Kennerley, A.J., Trampel, R., Guidi, M., Reimer, E., Ivanov, D., Neef, N., Gauthier, C.J., Turner, R., Möller, H.E., 2015. Cortical lamina-dependent blood volume changes in human brain at 7T. Neuroimage 107, 23–33. https://doi.org/10.1016/j.neuroimage.2014.11.046

Huber, L., Handwerker, D.A., Jangraw, D.C., Chen, G., Hall, A., Stüber, C., Gonzalez-Castillo, J., Ivanov, D., Marrett, S., Guidi, M., Goense, J.B.M., Poser, B.A., Bandettini, P.A., 2017. High-resolution CBV-fMRI allows mapping of laminar activity and connectivity of cortical input and output in human M1. Neuron 96, 1–11. https://doi.org/10.1016/j.neuron.2017.11.005

Huber, L., Ivanov, D., Handwerker, D.A., Marrett, S., Guidi, M., Uludağ, K., Bandettini, P.A., Poser, B.A., 2018. Techniques for blood volume fMRI with VASO: From low-resolution mapping towards sub-millimeter layer-dependent applications. Neuroimage 164, 131–143. https://doi.org/10.1016/j.neuroimage.2016.11.039

Huber, L., Ivanov, D., Krieger, S.N., Streicher, M.N., Mildner, T., Poser, B.A., Möller, H.E., Turner, R., 2014. Slab-selective, BOLD-corrected VASO at 7 tesla provides measures of cerebral

blood volume reactivity with high signal-to-noise ratio. Magn. Reson. Med. 72, 137–148. https://doi.org/10.1002/mrm.24916

Hurley, A.C., Al-radaideh, A., Bai, L., Aickelin, U., Coxon, R., Glover, P., Gowland, P.A., 2010. Tailored RF pulse for magnetization inversion at ultrahigh field. Magn. Reson. Med. 63, 51–58. https://doi.org/10.1002/mrm.22167

Jäncke, L., Mirzazade, S., Specht, K., Loose, R., Himmelbach, M., Müller-Gärtner, H.W., 1998. A parametric analysis of the "rate effect" in the sensorimotor cortex: A fMRI analysis. Neuroimage 7, 37–40. https://doi.org/10.1016/s1053-8119(18)31771-3

Jin, T., Kim, S.G., 2008. Improved cortical-layer specificity of vascular space occupancy fMRI with slab inversion relative to spin-echo BOLD at 9.4 T. Neuroimage 40, 59–67. https://doi.org/10.1016/j.neuroimage.2007.11.045

Khushu, S., Kumaran, S.S., Tripathi, R.P., Gupta, A., Jain, P.C., Jain, V., 2001. Functional magnetic resonance imaging of the primary motor cortex in humans: Response to increased functional demands. J. Biosci. 26, 205–215. https://doi.org/10.1007/BF02703644

Kim, S.-G., Ogawa, S., 2012. Biophysical and physiological origins of blood oxygenation level-dependent fMRI signals. J. Cereb. Blood Flow Metab. 32, 1188–206. https://doi.org/10.1038/jcbfm.2012.23

Liu, H.L., Gao, J.H., 2000. An investigation of the impulse functions for the nonlinear BOLD response in functional MRI. Magn. Reson. Imaging 18, 931–938. https://doi.org/10.1016/S0730-725X(00)00214-9

Liu, Z., Rios, C., Zhang, N., Yang, L., Chen, W., He, B., 2010. Linear and nonlinear relationships between visual stimuli, EEG and BOLD fMRI signals. Neuroimage 50, 1054–1066. https://doi.org/10.1016/j.neuroimage.2010.01.017

Logothetis, N.K., 2008. What we can do and what we cannot do with fMRI. Nature 453, 869–878. https://doi.org/10.1038/nature06976

Logothetis, N.K., Pauls, J., Augath, M., Trinath, T., Oeltermann, A., 2001. Neurophysiological investigation of the basis of the fMRI signal. Nature 412, 150–157. https://doi.org/10.1038/35084005

Lu, H., Golay, X., Pekar, J.J., van Zijl, P.C.M., 2003. Functional magnetic resonance imaging based on changes in vascular space occupancy. Magn. Reson. Med. 50, 263–274. https://doi.org/10.1002/mrm.10519

Lu, H., Hua, J., van Zijl, P.C.M.M., 2013. Noninvasive functional imaging of cerebral blood volume with vascular-space-occupancy (VASO) MRI. NMR Biomed. 26, 932–948. https://doi.org/10.1002/nbm.2905

Lu, H., Van Zijl, P.C.M., Hendrikse, J., Golay, X., 2004. Multiple Acquisitions with Global Inversion Cycling (MAGIC): A Multislice Technique for Vascular-Space-Occupancy Dependent fMRI. Magn. Reson. Med. 51, 9–15. https://doi.org/10.1002/mrm.10659

Maieron, M., Iannetti, G.D., Bodurka, J., Tracey, I., Bandettini, P.A., Porro, C.A., 2007. Functional responses in the human spinal cord during willed motor actions: Evidence for side- and rate-dependent activity. J. Neurosci. 27, 4182–4190. https://doi.org/10.1523/JNEUROSCI.3910-06.2007

Makin, T.R., De Xivry, J.J.O., 2019. Ten common statistical mistakes to watch out for when writing or reviewing a manuscript. Elife 8, 1–13. https://doi.org/10.7554/eLife.48175

Miezin, F.M., Maccotta, L., Ollinger, J.M., Petersen, S.E., Buckner, R.L., 2000. Characterizing the hemodynamic response: Effects of presentation rate, sampling procedure, and the possibility of ordering brain activity based on relative timing. Neuroimage 11, 735–759. https://doi.org/10.1006/nimg.2000.0568

Miller, K.L., Luh, W.M., Liu, T.T., Martinez, A., Obata, T., Wong, E.C., Frank, L.R., Buxton, R.B., 2001. Nonlinear temporal dynamics of the cerebral blood flow response. Hum. Brain Mapp. 13, 1–12. https://doi.org/10.1002/hbm.1020

R Development Core, T., 2008. Computational Many-Particle Physics. https://doi.org/10.1007/978-3-540-74686-7

Rao, S.M., Bandettini, P.A., Binder, J.R., Bobholz, J.A., Hammeke, T.A., Stein, E.A., Hyde, J.S., 1996. Relationship between finger movement rate and functional magnetic resonance signal change in human primary motor cortex. J. Cereb. Blood Flow Metab. 16, 1250–1254. https://doi.org/10.1097/00004647-199611000-00020

Rees, G., Howseman, A., Josephs, O., Frith, C.D., Friston, K.J., Frackowiak, R.S.J.J., Turner, R., 1997. Characterizing the relationship between BOLD contrast and regional cerebral blood flow measurements by varying the stimulus presentation rate. Neuroimage 6, 270–278. https://doi.org/10.1006/nimg.1997.0300

Riecker, A., Wildgruber, D., Mathiak, K., Grodd, W., Ackermann, H., 2003. Parametric analysis of rate-dependent hemodynamic response functions of cortical and subcortical brain structures during auditorily cued finger tapping: A fMRI study. Neuroimage 18, 731–739. https://doi.org/10.1016/S1053-8119(03)00003-X

Sadato, N., Ibañez, V., Campbell, G., Deiber, M.P., Le Bihan, D., Hallett, M., 1997. Frequency-dependent changes of regional cerebral blood flow during finger movements: Functional MRI compared to pet. J. Cereb. Blood Flow Metab. 17, 670–679. https://doi.org/10.1097/00004647-199706000-00008

Scouten, A., Constable, R.T., 2007. Applications and limitations of whole-brain MAGIC VASO functional imaging. Magn. Reson. Med. 58, 306–315. https://doi.org/10.1002/mrm.21273

Siero, J.C.W., Hermes, D., Hoogduin, H., Luijten, P.R., Petridou, N., Ramsey, N.F., 2013. BOLD consistently matches electrophysiology in human sensorimotor cortex at increasing movement rates: A combined 7T fMRI and ECoG study on neurovascular coupling. J. Cereb. Blood Flow Metab. 33, 1448–1456. https://doi.org/10.1038/jcbfm.2013.97

Siero, J.C.W., Petridou, N., Hoogduin, H., Luijten, P.R., Ramsey, N.F., 2011. Cortical depth-dependent temporal dynamics of the BOLD response in the human brain. J. Cereb. Blood Flow Metab. 31, 1999–2008. https://doi.org/10.1038/jcbfm.2011.57

Soltysik, D.A., Peck, K.K., White, K.D., Crosson, B., Briggs, R.W., 2004. Comparison of hemodynamic response nonlinearity across primary cortical areas. Neuroimage 22, 1117–1127. https://doi.org/10.1016/j.neuroimage.2004.03.024

Uludağ, K., Blinder, P., 2016. Linking brain vascular physiology to hemodynamic response in ultra-high field MRI. Neuroimage 168, 279–295. https://doi.org/10.1016/j.neuroimage.2017.02.063

Van Der Zwaag, W., Marques, J.P., Kober, T., Glover, G., Gruetter, R., Krueger, G., 2012. Temporal SNR characteristics in segmented 3D-EPI at 7T. Magn. Reson. Med. 67, 344–352.

https://doi.org/10.1002/mrm.23007

Vazquez, A.L., Noll, D.C., 1998. Nonlinear aspects of the BOLD response in functional MRI. Neuroimage 7, 108–118. https://doi.org/10.1006/nimg.1997.0316

Yeşilyurt, B., Uğurbil, K., Uludağ, K., 2008. Dynamics and nonlinearities of the BOLD response at very short stimulus durations. Magn. Reson. Imaging 26, 853–862. https://doi.org/10.1016/j.mri.2008.01.008

Zhang, N., Yacoub, E., Zhu, X.-H., Ugurbil, K., Chen, W., 2009. Linearity of blood-oxygenation-level dependent signal at microvasculature. Neuroimage 48, 313–318. https://doi.org/10.1016/j.neuroimage.2009.06.071

Zhang, N., Zhu, X.H., Chen, W., 2008. Investigating the source of BOLD nonlinearity in human visual cortex in response to paired visual stimuli. Neuroimage 43, 204–212. https://doi.org/10.1016/j.neuroimage.2008.06.033

Chapter 4

Improved selectivity in 7T digit mapping using VASO-CBV

Ícaro A.F. de Oliveira,
Jeroen C.W. Siero,
Serge O. Dumoulin,
Wietske van der Zwaag

Submitted

Abstract

Functional magnetic resonance imaging (fMRI) at Ultra-high field (UHF, ≥ 7T) benefits from significant gains in the BOLD contrast-to-noise ratio (CNR) and temporal signal-to-noise ratio (tSNR) compared to conventional field strengths (3T). Although these improvements enabled researchers to study the human brain to unprecedented spatial resolution, the blood pooling effect reduces the spatial specificity of the widely-used gradient-echo BOLD acquisitions. In this context, vascular space occupancy (VASO-CBV) imaging may be advantageous since it is proposed to have a higher spatial specificity than BOLD. We hypothesized that the assumed higher specificity of VASO-CBV imaging would translate to reduced overlap in fine-scale digit representation maps compared to BOLD-based digit maps. We used sub-millimeter resolution VASO fMRI at 7T to map VASO-CBV and BOLD responses simultaneously in the motor and somatosensory cortices during individual finger movement tasks. We assessed the cortical overlap in different ways, first by calculating similarity coefficient metrics (DICE and Jaccard) and second by calculating selectivity measures. In addition, we demonstrate a consistent topographical organization of the targeted digit representations (thumb-index-little finger) in the motor areas. In terms of specificity, we show that the VASO-CBV responses yielded less overlap between the digit clusters than BOLD, and specificity measures were higher for VASO-CBV too. In summary, these results were consistent across metrics and participants, confirming the higher spatial specificity of VASO-CBV compared to BOLD.

Introduction

Functional MRI (fMRI), based on the blood oxygenation level-dependent (BOLD) effect, is the most popular tool for mapping brain activity (Kim and Ogawa, 2012). Recent advanced scanner technology, including ultra-high field (UHF) magnetic field strengths, improved image acquisition techniques and advanced analysis tools have enabled researchers to investigate the human brain at a sub-millimeter scales (Dumoulin et al., 2017; Norris and Polimeni, 2019; Uğurbil, 2021; Uludağ and Blinder, 2016). In UHF-fMRI, there are two crucial gains for fMRI, the increased temporal SNR and the functional BOLD contrast that increases supra-linearly with field strength (Cai et al., 2021; van der Zwaag et al., 2009). Because of its high sensitivity to deoxyhemoglobin variations and widespread availability, gradient-echo (GRE) BOLD remains the most widely used contrast in fMRI. Unfortunately, the GRE BOLD signal is predominantly driven by the (large) draining vessels, resulting in a biased measurement towards the superficial cortical layers (Markuerkiaga et al., 2016; Uludağ et al., 2009; Yacoub and Wald, 2018). Nevertheless, different MRI contrasts are sensitive to other physiological variables that can be used to study brain function, like cerebral blood flow (CBF) with Arterial Spin Labeling (ASL) (Kashyap et al., 2021) or cerebral blood volume (CBV) with Vascular Space Occupancy (VASO) techniques (Huber et al., 2017).

The human brain contains multiple homunculi, or orderly body representations, in the sensory and motor cortices (Penfield and Boldrey, 1937). The individual body parts within these somatotopic maps occupy small parts of the cortex, integrating signal from a variable number of neurons (Gardner and Costanzo, 1980). Visualizing somatotopic maps in humans with fMRI has benefited from the advent of UHF fMRI. The higher SNR at UHF can be used to acquire images with higher spatial and temporal resolution. Higher spatial resolution (smaller voxel sizes) reduces partial volume effects (PVE), enabling researchers to more accurately map the human somatotopic organization. Recent studies demonstrated individual finger movements in the primary motor (M1) and primary somatosensory (S1) areas, notably at the individual level (Besle et al., 2014; Kolasinski et al., 2016; Sanchez-Panchuelo et al., 2010; Schellekens et al., 2018; Stringer et al., 2011). In addition, some studies have focused on showing that the spatial pattern of BOLD activation at 7T reflects the patterns of underlying neural activity (Martuzzi et al., 2014), with a direct comparison with electrocorticography (ECoG) (Siero et al., 2014). More recently, Huber and colleagues used the higher specificity of VASO-CBV to distinguish two

mirrored topographical representations of digits in the primary motor cortex (Huber et al., 2020).

These studies show that high-resolution fMRI is a useful tool to study the somatotopic organization. The investigation of pathological conditions such as movement disorders or any disturbed sensory representation in neurological disorders like dystonia (Butterworth et al., 2003) also benefits from these methodological advances to map and quantify the organization of motor function (Marquis et al., 2017). Moreover, a qualitative and quantitative assessment of the changes in the cortical organization induced by these pathological conditions and the brain plasticity is essential to understanding the underlying mechanisms of brain disease. It may be relevant for developing or evaluating novel therapeutics or intervention strategies (Olman et al., 2012; Serino et al., 2017).

Because individual digit movements selectively activate distinct patches of the cortex, it is possible to quantify the degree of selectivity to one digit movement and the relationship of the cortical region to the movement of other digits (Akselrod et al., 2017; Martuzzi et al., 2014; Olman et al., 2012). This measurement is called selectivity (or response selectivity), and it can therefore be used to quantify the cortical overlap between adjacent digit clusters. There are, however, different contributions to the overlap, which can be separated in 'neural', 'vascular', and 'methodology' related overlap. For example, the methodological aspects, such as the partial volume effect (PVE), head motion, and smoothing, are image acquisition-related and contribute to the measured overlap. The vascular overlap contribution arises from the blood pooling effect, which limits the spatial specificity of the BOLD response (Menon, 2002; Turner, 2002). The neuronal overlap contribution arises from the notion that a specific neuronal population distributed in a part of the motor cortex, for example, does not encode a single finger's movement. Instead, they may contribute to the movement of several fingers (Gardner and Costanzo, 1980; Georgopoulos et al., 1999).

The Vascular Space Occupancy (VASO) method is advantageous since it promises higher specificity than BOLD due to reduced draining vein contamination (Huber et al., 2014; Jin and Kim, 2008; Lu et al., 2013), especially for high spatial resolutions (Huber et al., 2020, 2017). The fine-scaled digit representation maps in the somatosensory cortex will likely benefit significantly from more spatially specific measurements. Here, we simultaneously measured VASO-CBV and BOLD responses at sub-millimeter resolution using a double 3D-EPI VASO

sequence (Huber et al., 2014; Oliveira et al., 2021) during the execution of individual finger movements using block-designed stimuli. We hypothesize that the higher specificity of VASO-CBV images will result in higher response selectivity due to reduced vascular overlap.

Materials and Methods

Participants

Six healthy individuals (4 females mean age 30 ± 4 years) with no history of neurologic or orthopedic conditions participated in the study. All participants provided written informed consent before participating after being informed of the experimental procedures, and the local Medical Ethical Committee approved the study.

Stimulus

The functional study was conducted in a single session. The participants performed the same task three times, once for each digit (thumb (D1), index (D2), and little (D5)) of the right hand. The task consisted of flexing one finger from an extended position periodically following a visual cue. The visual cue was projected on a screen at the end of the scanner's bore, which the participants viewed using a mirror. The visual cue was generated in 'Matlab' (The MathWorks, Natick, United States) using the 'Psychophysics Toolbox Version 3' (Brainard, 1997; Kleiner et al., 2007). The task paradigm consisted of 30 seconds of baseline with one-minute blocks: 30s paced flexing-extension at 1Hz and 30s rest, repeated ten times, resulting in 10 minutes and 30 seconds of acquisition for each digit (defined as one run). For this task, flexion of D5 usually resulted in co-movement of D4 and the distal phalanx of D3. Nevertheless, we refer to this movement as 'D5'.

MR Sequences

The Slice Selective Slab Inversion VASO with 3D EPI readout (Huber et al., 2014; Oliveira et al., 2021) was implemented on a 7T MRI scanner (Philips Healthcare, Best, The Netherlands) using an eight-channel transmit coil and a 32 channel receive coil (Nova Medical Inc,

Wilmington, United States) with B1 shim settings from a previous study (Oliveira et al., 2021). In addition, an adiabatic inversion TR-FOCI pulse was used to ensure an effective inversion with reduced B1+ inhomogeneity (Hurley et al., 2010). The timing parameters for the interleaved acquisition were $TI_1/TI_2/TE/TR$ = 1100/2340/24/3000 ms. Data were acquired with a nominal in-plane resolution of 0.79mm and nominal slice thickness of 1.5mm (0.79 × 0.79 × 1.5 mm^3), FOV = 140×140×20 mm^3, matrix size = 176×176, 13 slices, partial Fourier factor = 0.78 in the phase encoding direction, $BW_{readout}$ = 87 Hz, and $SENSE_{inplane}$ factor = 2.7.

Data Analysis

The preprocessing steps consisted of a separate motion correction for BOLD and VASO-CBV data using SPM (Statistical Parametric Mapping), followed by the BOLD correction to minimize the extravascular BOLD signal present in the VASO images (Huber et al., 2014). We used the NORDIC PCA denoising technique (Moeller et al., 2021; Vizioli et al., 2021) before the head motion correction step to increase the tSNR and accuracy of the functional maps. No additional smoothing or temporal filtering was applied to minimize the loss in specificity. The alignment across the three-digit runs was conducted as part of the motion correction. After that, we computed z-score maps for each finger movement using FEAT in FSL (v.6.0). Statistical differences between VASO-CBV and BOLD were assessed using Paired t-tests in R (R Core Team, 2020).

The region of interest (ROI) definition was based on VASO-CBV and BOLD activated voxels as described below. M1 and S1 masks were drawn manually based on anatomical landmarks, i.e., the pre and post-central gyri. We included all voxels in the M1 and S1 regions that responded to the stimulation with a z-score greater than 2.5 for at least one digit in VASO-CBV and BOLD data.

We calculated the Dice Similarity Coefficient (DSC) and Jaccard Similarity Coefficient (JSC) for each digit cluster-pair (D1-D2, D1-D5, and D2-D5). Both metrics are overlap-based and often used to validate segmentation boundaries (Carass et al., 2020), and here were used to quantify the overlap between digit clusters. We defined these clusters from the statistical z-score maps for the movement of each digit within the M1 and S1 ROI. Next, a 'winner-takes-all' approach was used to divide the ROIs into digit clusters to obtain binary (non-overlapping)

digit representation maps and calculate the average z-scores of the dominant digit and the non-dominant digits (e.g., response to movement of D2 in the D1 ROI).

Finally, we used two distinct approaches to quantify the selectivity: 1) a general approach called 'overall selectivity' (OS). For the *OS* approach, we divide the maximum z-score between all three digits by the sum of the z-scores to all three digit movements. The advantage of the OS measure is the straightforward calculation because it does not require a winner-takes-all step (Equation 1). However, the disadvantage is that negative z-scores in the non-dominant digits (a common occurrence in somatotopic maps) can lead to a division by 0 and excessive selectivity values (see Supplementary Figure 2). Approach 2) is a more controlled measure, called 'digit selectivity' (DS). Voxels were assigned to a specific digit for the DS approach using a winner-takes-all approach, followed by equation [2] to quantify the selectivity per digit. In [2], we take the mean difference between the response of the thumb (D1), index finger (D2), and the little finger (D5) divided by the response of the thumb (D1). The benefit of the *DS* measure is that it avoids the division by zero or by negative values (see Supplementary Figure 2).

$$Overall\ Selectivity = \frac{\max(D_1,D_2,D_5)}{\sum(D_1,D_2,D_5)} \text{ [1]}$$

$$Digit\ Selectivity\ (D1) = \frac{0.5\cdot\left((D_1-D_2)+(D_1-D_5)\right)}{D_1} \text{ [2]}$$

Results

Robust VASO-CBV and BOLD responses in M1 and S1 were detected in all six participants (Figure 1). Figure 1 shows example slices of digit representation maps for all six participants. The maps show distinct activation patterns for movement of each of the three digits for this block-design task, organized in an orderly fashion (thumb-index-little finger) along the central sulcus and predominantly in S1. A secondary representation of the index and thumb, superior to the little digit representations, can be seen for subjects P02-P05. The VASO-CBV responses are smaller in amplitude and cluster size than the BOLD responses. In Figure 1, the threshold (Z-score $_{\text{VASO-CBV}}$ from 3 to 7 and from Z-score $_{\text{BOLD}}$ from 5 to 15) is adapted to allow a visual comparison of the activation patterns.

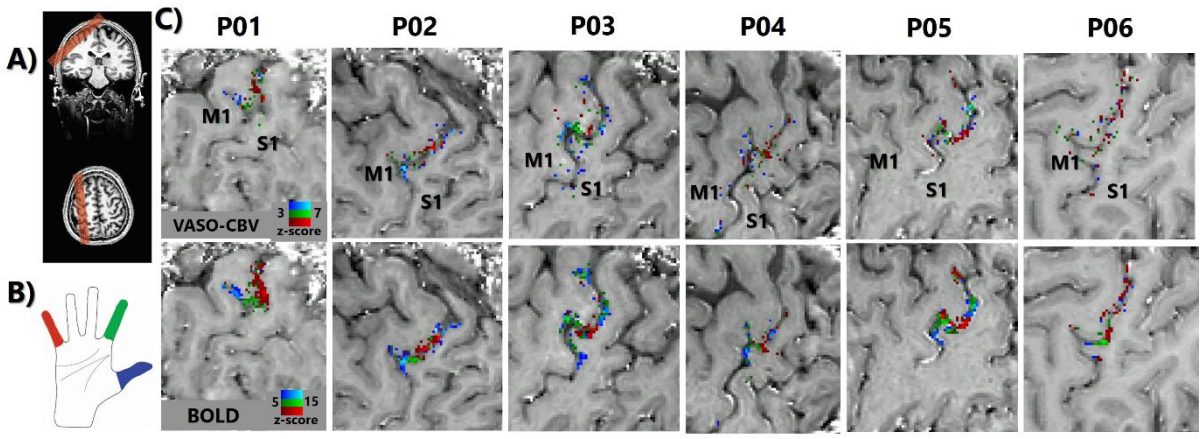

Figure 1. Overview of the acquisition method and the topographic digit mapping of a subset of fingers (D1, D2, and D5) using VASO-CBV and BOLD in the 6 participants. A) We carefully positioned the imaging slab (0.79 × 0.79 × 1.5 mm^3) to cover the left primary sensorimotor area. B) The participants performed individual finger movement on a block-designed task, using thumb (blue, D1), index (green, D2), and little (red, D5). C) Each voxel was assigned to a single digit using a winner-take-all algorithm, creating a subset of digit representation maps. The digit representations are orderly organized (thumb-index-little) along the central sulcus, predominantly in S1. No smoothing has been applied on VASO-CBV or BOLD data.

The quantification of the spatial similarity of each digit-pair is depicted in Figure 2. The DSC of each pair of digit clusters represents the overlap between that pair of response patterns. The pair-digits behave similarly for the M1 and S1 regions, with BOLD yielding consistently higher DSC values and, therefore, higher overlap than VASO-CBV. There was a significant difference between VASO-CBV and BOLD for both M1 and S1 regions for all three digit pairs (Paired t-test, $p<0.05$). The DSC scores were similar between digit-pairs for both ROIs, with a significant difference for the DSC score in the D2-D5 for BOLD (Paired t-test, $p<0.05$). Additionally, we used a Jaccard Similarity Coefficient (Supplementary Fig.1) on the same cluster in the same manner, and the results were nearly identical, with BOLD yielding a significantly higher overlap than VASO-CBV (Paired t-test, $p<0.05$).

After assigning the voxels with a winner-take-all strategy, we calculated the average z-scores of the dominant digit for a given digit cluster and the average z-scores of responses for movement of the other digits in the same voxels. Figure 3 illustrates the M1 and S1 results across all six participants. The obtained patterns were consistent across digits and participants, visualized as black dots in each subpanel of Figure 3. The z-scores for movement of the non-dominant digit were higher in the BOLD data than in the VASO-CBV data for both regions,

indicating more overlap and crosstalk in BOLD digit clusters than in VASO-CBV digit clusters, see the average group results in Table 1. These results agree with the DSC and JSC results in Figure 2 and Supplemental Figure 1. Consistent with the maps shown in Figure 1, the z-scores, on the whole, are higher for BOLD.

Figure 4A illustrates the overall selectivity *(OS)* measure for M1 and S1, and Figure 4B illustrates the digit selectivity *(DS)*. For the *OS*, VASO-CBV shows higher selectivity than BOLD for both ROIs (Paired t-test, $p<0.05$), with S1 showing higher selectivity indices than M1 for both VASO-CBV and BOLD (average $VASO\text{-}CBV_{M1} = 0.613 \pm 0.104$, $VASO\text{-}CBV_{S1} = 0.636 \pm 0.072$ and $BOLD_{M1} = 0.462 \pm 0.035$ and $BOLD_{S1} = 0.498 \pm 0.029$). All digit clusters showed similar results for the digit selectivity measure, with VASO-CBV yielding higher selectivity than BOLD (Paired t-test, $p<0.05$). Again, S1 yielded higher selectivity than M1 for both VASO-CBV and BOLD, though this difference was not significant (paired t-test, and see TABLE 2).

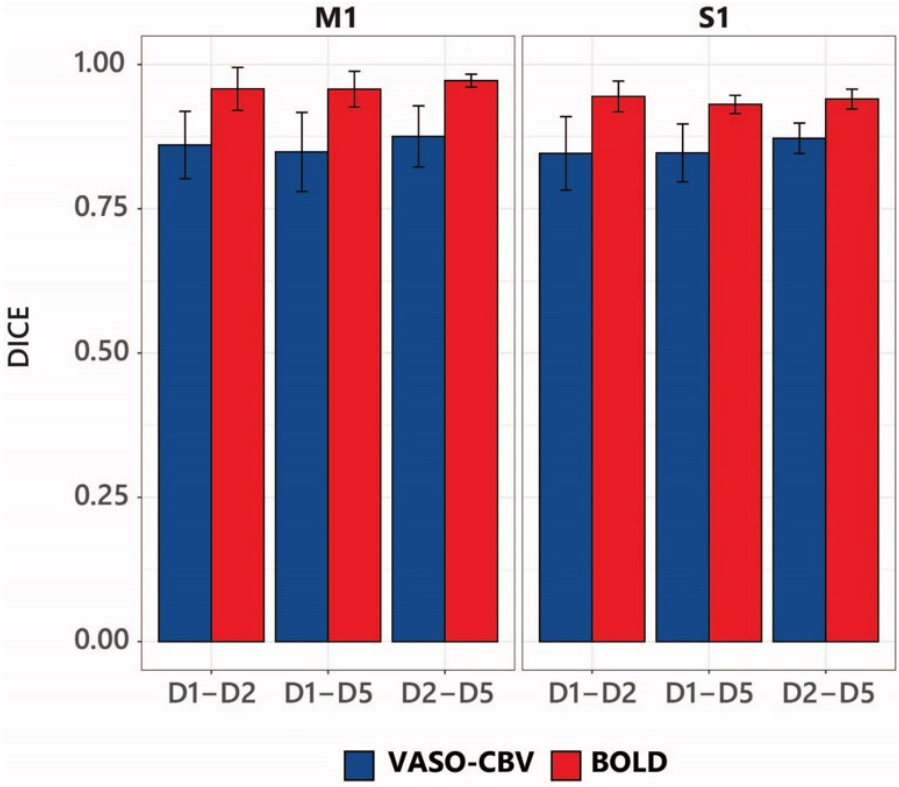

Figure 2. DICE similarity coefficients (DSC) for each pair-digit cluster in S1 and M1. BOLD yielded higher scores than VASO-CBV (Paired t-test, $p<0.05$) in both regions. A higher similarity score represents a higher overlap between each digit pair. The error bar is the standard deviation. Please see Supplementary Figure 1 for Jaccard measurements.

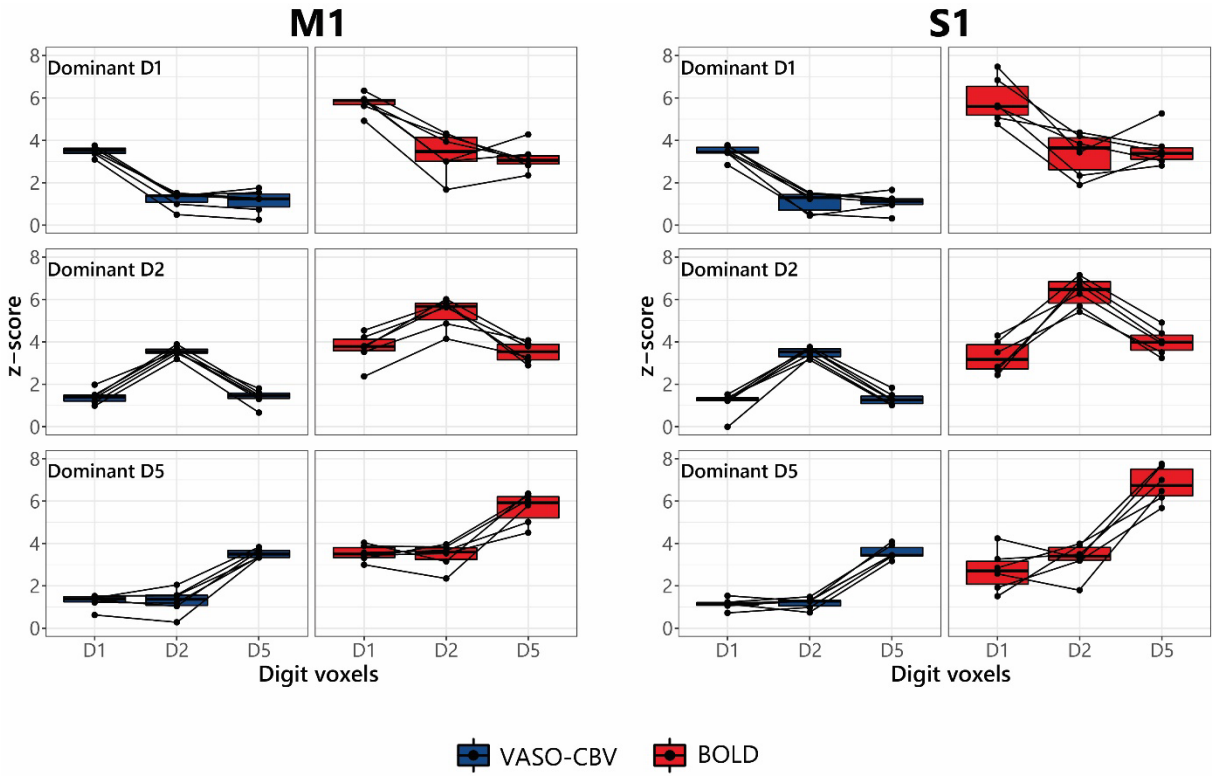

Figure 3. Average z-scores of the dominant finger (columns) in relation to the average z-score of the other voxels (digit voxels). The lines between each digit cluster denote each participant's average z-score. We found similar results for M1 and S1, with higher z-scores for the non-dominant digit voxels in the BOLD data than VASO-CBV data.

TABLE 1. Group average (z-scores) of the dominant finger in relation to the digit voxels for M1 and S1

Region	**DF**	**Digit voxels**					
		BOLD			**VASO-CBV**		
		D1	*D2*	*D5*	*D1*	*D2*	*D5*
M1	D1	5.76 ± 0.47	3.36 ± 1.01	3.15 ± 0.64	3.48 ± 0.24	1.20 ± 0.39	1.13 ± 0.55
	D2	3.70 ± 0.75	5.37 ± 0.72	3.51 ± 0.48	1.40 ± 0.34	3.55 ± 0.23	1.38 ± 0.39
	D5	3.54 ± 0.38	3.41 ± 0.59	5.66 ± 0.74	1.27 ± 0.34	1.28 ± 0.60	3.53 ± 0.21
S1	D1	5.89 ± 1.05	3.35 ± 1.02	3.60 ± 0.88	3.44 ± 0.34	1.09 ± 0.48	1.07 ± 0.44
	D2	3.29 ± 0.75	6.35 ± 0.69	4.00 ± 0.60	1.12 ± 0.56	3.49 ± 0.24	1.32 ± 0.31
	D5	2.72 ± 0.97	3.28 ± 0.80	6.79 ± 0.83	1.14 ± 0.26	1.18 ± 0.27	3.58 ± 0.35

Abbreviations: DF, Dominant finger.

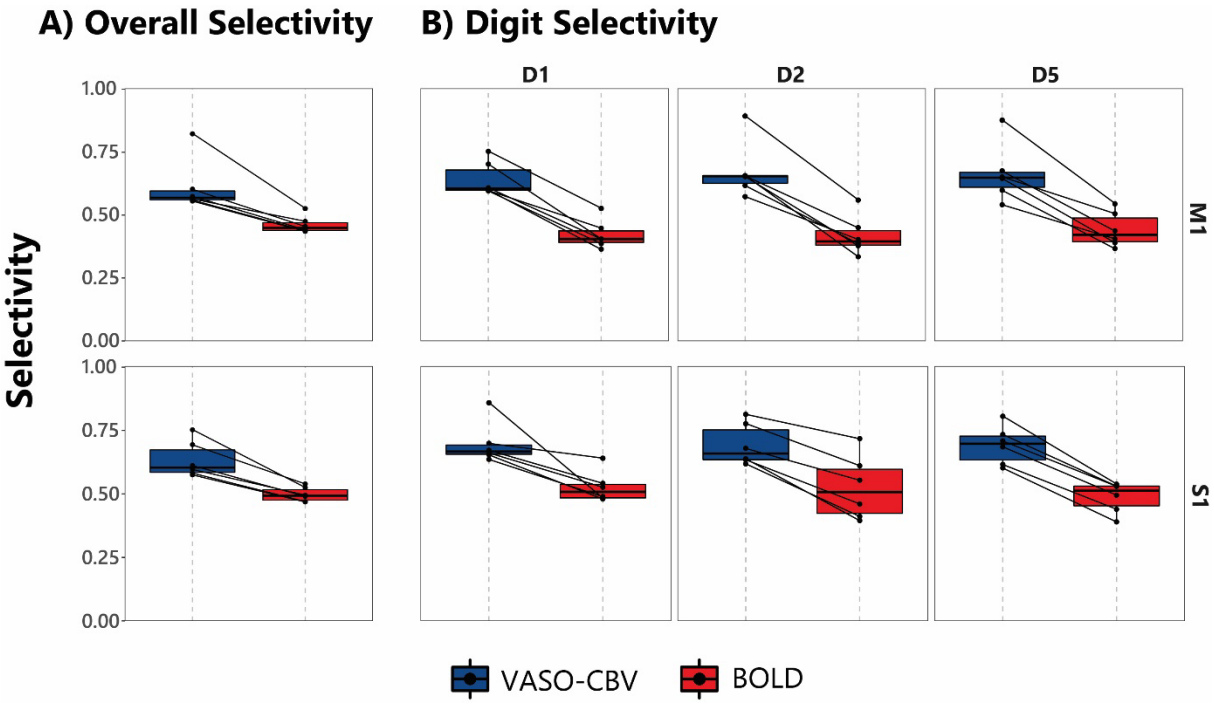

Figure 4. Response selectivity indices for the VASO-CBV and BOLD responses in M1 and S1. A) Overall selectivity, and B) Digit selectivity with D1 (thumb), D2 (index), and D5 (little) according to equations 1 and 2 (see methods). Both selectivity indices describe the magnitude of the fMRI response to the movement of a specific digit relative to the motion of other digits. For the overall selectivity, VASO-CBV showed higher cortical selectivity for all participants (lines denote each participant result) and both M1 and S1. The digit selectivity indices are also higher for VASO-CBV for all participants in both M1 and S1 when compared with BOLD.

TABLE 2. Average overall (OS) and digit selectivity (DS) for M1 and S1 ROIs (MEAN ± SD)

Region	**Method**	**Digit Selectivity**			**Overall Selectivity**
		D1	*D2*	*D5*	
M1	VASO-CBV	0.642 ± 0.068	0.674 ± 0.111	0.664 ± 0.114	0.613 ± 0.104
	BOLD	0.422 ± 0.058	0.418 ± 0.078	0.441 ± 0.070	0.462 ± 0.035
S1	VASO-CBV	0.696 ± 0.082	0.693 ± 0.082	0.691 ± 0.076	0.636 ± 0.072
	BOLD	0.526 ± 0.061	0.524 ± 0.126	0.487 ± 0.060	0.498 ± 0.029

Discussion

The present study compares the specificity between VASO-CBV and BOLD cortical activation of individual finger movements in healthy participants employing response selectivity and spatial overlap metrics. We simultaneously measured high-resolution VASO-

CBV and BOLD responses using SS-SI VASO sequence with a 3D-EPI readout. Therefore, any observed differences between VASO and BOLD fMRI is unlikely the result of task performance or head movement variations. We assessed the cortical overlap in different ways, (1) by calculating the Dice similarity coefficient (DSC), Jaccard similarity coefficient and assessing crosstalk between digit responses with the averaged z-scores of the dominant finger with respect to the other fingers, and (2) selectivity measurements. Using standard block-designed stimuli, we showed that VASO-CBV yields less overlap between the digit clusters than BOLD for both types of metrics. Moreover, we demonstrate a consistent topographical representation of part of the sensorimotor digit region (thumb-index-little fingers).

We consistently found distinct activation patterns for movement of each of the three digits, organized in an orderly fashion (thumb-index-little) along the central sulcus, reproducing the results reported by (Siero et al., 2014), which used the same group of fingers and directional cortical electrophysiological measurements, albeit with a slightly different stimulus design. Moreover, the activation progression pattern was similar to 7T BOLD fMRI studies employing tactile stimuli (Besle et al., 2014; Kolasinski et al., 2016; Sanchez-Panchuelo et al., 2010; Schellekens et al., 2018; Stringer et al., 2011), 3T BOLD fMRI (Olman et al., 2012) and a recent 7T VASO fMRI motor study (Huber et al., 2020). In addition, our results also showed a secondary representation of the index and thumb, positioned superior to the little finger representations (seen for participants P02-P05), as previously found by (Huber et al., 2020). The VASO-CBV responses are smaller in amplitude and cluster size than the BOLD responses, as also reported previously in different VASO-CBV – BOLD comparisons (Huber et al., 2020, 2017; Oliveira et al., 2022, 2021).

For the DSC results, the BOLD data yielded higher DSC values than VASO-CBV and hence higher overlap between the activation clusters. The results for the Jaccard similarity coefficient were nearly identical (see Supplementary Figure 1). A complementary measurement was performed with the averaged z-scores of the dominant digit relative to the average z-scores of the responses for the other digits (Figure 2). The averaged z-scores behaved similarly to the overlap metrics (DSC and JSC). Moreover, our results were consistent across participants. VASO-CBV yielded higher selectivity than BOLD for the overall and the individual digit selectivity (Figure 4). These results were also consistent across participants. We did not observe significant differences between M1 and S1 in the DSC, JSC, or crosstalk measures except in (D2-

D5, for DSC). Taken together, the observed higher response selectivity for the VASO-CBV signal corroborates the hypothesized higher vascular specificity of VASO-CBV fMRI compared to the BOLD signal.

The digit overlap between different digit representations has different sources, i.e., neural, vascular, and methodology-related overlap. Because we acquired VASO-CBV and BOLD signal within the same functional run, the neural and methodological contributions are not expected to differ in VASO-CBV compared to BOLD. The higher specificity in VASO-CBV is likely due to the lower vascular contribution in the point-spread function. Thus, we speculate that the selectivity quantification using VASO-CBV could be a tool to investigate pathological conditions related to sensory and motor function and may perhaps be used to investigate brain plasticity or aging and development.

Regarding the selectivity metrics used, we opted for multiple selectivity metrics rather than a single metric because there are pros and cons to applying these metrics. As our results show, *OS* and *DS* metrics demonstrate a higher spatial specificity for the VASO-CBV. However, by using the overall selectivity, lower or negative responses (z-scores) in a single-digit voxel can lead to divisions by zero and outliers values, potentially shifting the ROI selectivity value. We did not observe a significant number of outliers here (less than 1%). On the other hand, digit selectivity is better controlled, and this metric captures the selectivity for each digit. For these reasons, we favor *digit selectivity* rather than *overall selectivity*. Nevertheless, both metrics showed the same pattern and were consistent across participants. Another common approach is calculating the sum of the absolute value of the responses using equation 1. This way, the outliers can also be avoided; however, it can also lead to overestimating or underestimating the selectivity values (see OS_2 in Supplementary Figure 2).

Conclusion

Here, we simultaneously recorded submillimeter VASO-CBV and BOLD signals to investigate cortical activation in the primary somatosensory and motor areas during individual finger movement. We used similarity and response selectivity metrics to compare VASO-CBV and BOLD specificity. BOLD showed a higher overlap and lower selectivity than VASO-CBV. These results were consistent across metrics and participants. Together, they suggest that the

higher vascular specificity of VASO-CBV results in higher response selectivity or less vascular overlap than BOLD, confirming the higher spatial specificity of VASO-CBV compared to BOLD.

Supplementary material

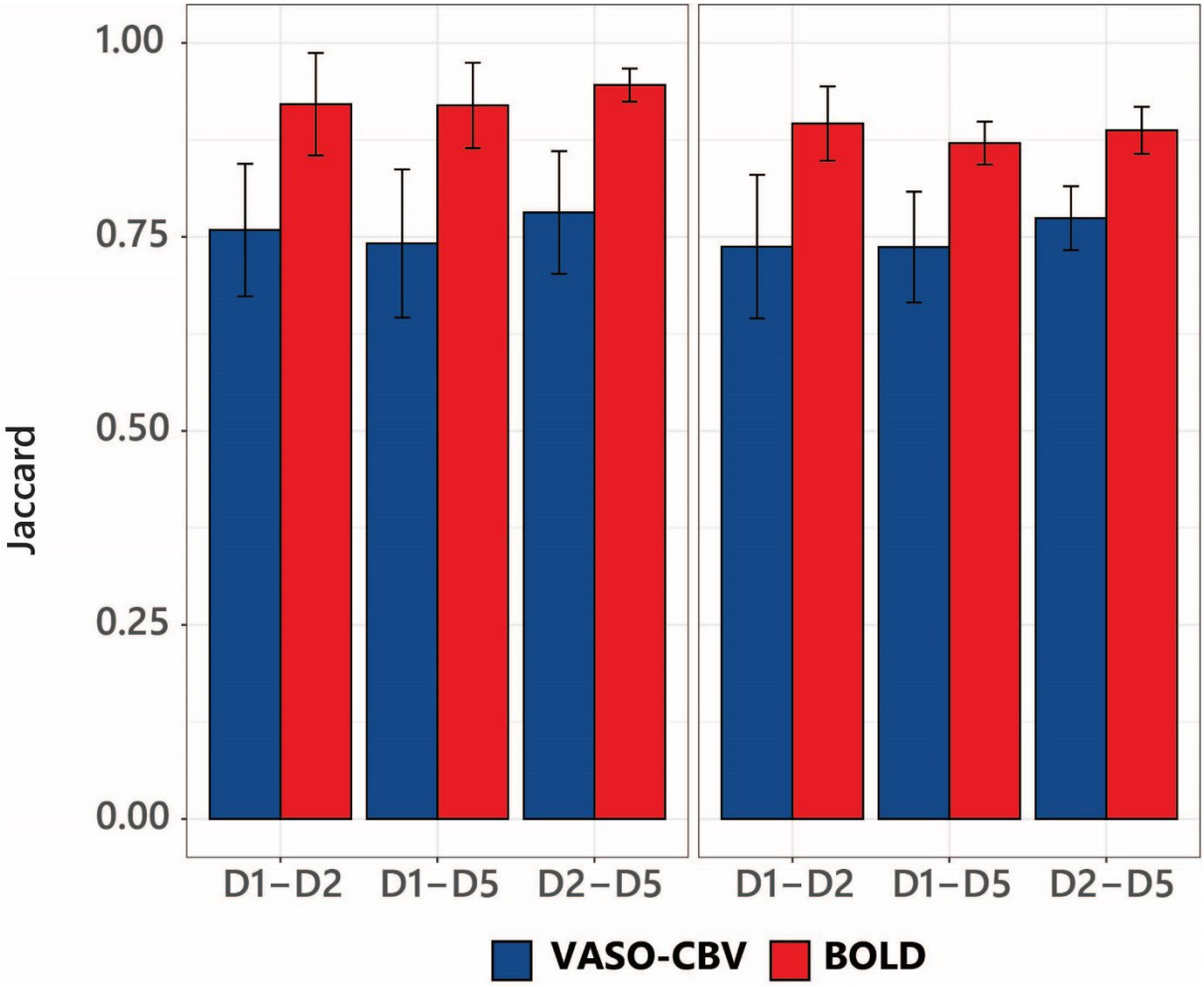

Supplementary Figure 1: Jaccard Similarity Coefficient (JSC) for each pair-digit in S1 and M1. As seen in Figure 2 with the DICE coefficient, the BOLD responses yielded higher scores than VASO-CBV (Paired t-test, $p<0.05$) in both regions. A higher similarity score represents a higher overlap between each digit pair. The error bar is the standard deviation.

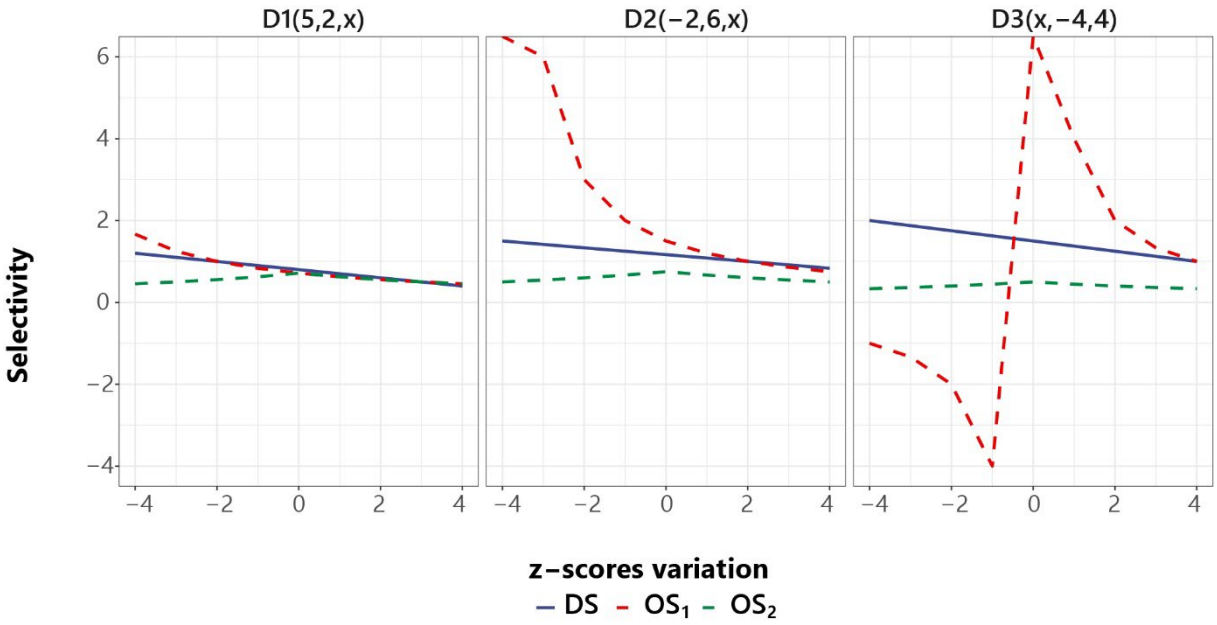

Supplementary Figure 2: Selectivity response using two variants of the overall selectivity (OS_1 and OS_2) in addition to the digit selectivity (DS). We computed each metric using the z-scores of the three fingers, D1, D2, and D5. Each column represents the result in a specific dominant digit. The number in parenthesis represents the z-scores, and x represents the digit z-score that we vary from -4 to 4. Each curve highlights the advantages and disadvantages of each selectivity method. For example, OS_1 is attractive because of its straightforward computation; it does not require a winner-take-all step. However, lower z-scores or negative values can lead to divisions by zero or negative selectivity responses, acting as outliers as shown for D2 and D3). In OS_2, the sum of the digits uses the absolute value of each digit. Thus the OS_2 can avoid the outliers because the division by zero is not possible anymore. However, it can also lead to underestimating the selectivity values. The *DS* metric shows a more linear behavior, which we believe is preferred. The mean difference between the target digit and the others avoids division by zeros, and the *DS* can capture the selectivity of each digit rather than just one overall measurement.

References

Akselrod, M., Martuzzi, R., Serino, A., van der Zwaag, W., Gassert, R., Blanke, O., 2017. Anatomical and functional properties of the foot and leg representation in areas 3b, 1 and 2 of primary somatosensory cortex in humans: A 7T fMRI study. Neuroimage 159, 473–487. https://doi.org/10.1016/j.neuroimage.2017.06.021

Besle, J., Sánchez-Panchuelo, R.M., Bowtell, R., Francis, S., Schluppeck, D., 2014. Event-related fMRI at 7T reveals overlapping cortical representations for adjacent fingertips in S1 of individual subjects. Hum. Brain Mapp. 35, 2027–2043. https://doi.org/10.1002/HBM.22310/FORMAT/PDF

Brainard, D.H., 1997. The Psychophysics Toolbox. Spat. Vis. 10, 433–436. https://doi.org/10.1163/156856897X00357

Butterworth, S., Francis, S., Kelly, E., McGlone, F., Bowtell, R., Sawle, G. V., 2003. Abnormal cortical sensory activation in dystonia: An fMRI study. Mov. Disord. 18, 673–682. https://doi.org/10.1002/MDS.10416

Cai, Y., Hofstetter, S., van der Zwaag, W., Zuiderbaan, W., Dumoulin, S.O., 2021. Individualized cognitive neuroscience needs 7T: Comparing numerosity maps at 3T and 7T MRI. Neuroimage 237, 118184. https://doi.org/10.1016/j.neuroimage.2021.118184

Carass, A., Roy, S., Gherman, A., Reinhold, J.C., Jesson, A., Arbel, T., Maier, O., Handels, H., Ghafoorian, M., Platel, B., Birenbaum, A., Greenspan, H., Pham, D.L., Crainiceanu, C.M., Calabresi, P.A., Prince, J.L., Roncal, W.R.G., Shinohara, R.T., Oguz, I., 2020. Evaluating White Matter Lesion Segmentations with Refined Sørensen-Dice Analysis. Sci. Rep. 10, 8242. https://doi.org/10.1038/s41598-020-64803-w

Dumoulin, S.O., Fracasso, A., van der Zwaag, W., Siero, J.C.W., Petridou, N., 2017. Ultra-high field MRI: Advancing systems neuroscience towards mesoscopic human brain function. Neuroimage 0–1. https://doi.org/10.1016/j.neuroimage.2017.01.028

Gardner, E.P., Costanzo, R.M., 1980. Spatial integration of multiple-point stimuli in primary somatosensory cortical receptive fields of alert monkeys. https://doi.org/10.1152/jn.1980.43.2.420 43, 420–443. https://doi.org/10.1152/JN.1980.43.2.420

Georgopoulos, A.P., Pellizzer, G., Poliakov, A. V, Schieber, M.H., 1999. Neural coding of finger and wrist movements. J. Comput. Neurosci. 6, 279–288. https://doi.org/10.1023/A:1008810007672

Huber, L., Finn, E.S., Handwerker, D.A., Bönstrup, M., Glen, D.R., Kashyap, S., Ivanov, D., Petridou, N., Marrett, S., Goense, J., Benedikt, A., Bandettini, P.A., Poser, B.A., Bandettini, P.A., 2020. Sub-millimeter fMRI reveals multiple topographical digit representations that form action maps in human motor cortex. Neuroimage 208. https://doi.org/10.1016/j.neuroimage.2019.116463

Huber, L., Handwerker, D.A., Jangraw, D.C., Chen, G., Hall, A., Stüber, C., Gonzalez-Castillo, J., Ivanov, D., Marrett, S., Guidi, M., Goense, J., Poser, B.A., Bandettini, P.A., 2017. High-Resolution CBV-fMRI Allows Mapping of Laminar Activity and Connectivity of Cortical Input and Output in Human M1. Neuron 96, 1253-1263.e7. https://doi.org/10.1016/j.neuron.2017.11.005

Huber, L., Ivanov, D., Krieger, S.N., Streicher, M.N., Mildner, T., Poser, B.A., Möller, H.E., Turner, R., 2014. Slab-selective, BOLD-corrected VASO at 7 tesla provides measures of cerebral blood volume reactivity with high signal-to-noise ratio. Magn. Reson. Med. 72, 137–148. https://doi.org/10.1002/mrm.24916

Jin, T., Kim, S.G., 2008. Improved cortical-layer specificity of vascular space occupancy fMRI with slab inversion relative to spin-echo BOLD at 9.4 T. Neuroimage 40, 59–67. https://doi.org/10.1016/j.neuroimage.2007.11.045

Kashyap, S., Ivanov, D., Havlicek, M., Huber, L., Poser, B.A., Uludağ, K., 2021. Sub-millimetre resolution laminar fMRI using Arterial Spin Labelling in humans at 7 T. PLoS One 16, e0250504. https://doi.org/10.1371/journal.pone.0250504

Kim, S.-G., Ogawa, S., 2012. Biophysical and physiological origins of blood oxygenation level-dependent fMRI signals. J. Cereb. Blood Flow Metab. 32, 1188–206. https://doi.org/10.1038/jcbfm.2012.23

Kleiner, M., Brainard, D., Pelli, D., Ingling, A., Murray, R., Broussard, C., 2007. What's new in psychtoolbox-3. Perception 36, 1–16.

Kolasinski, X., Makin, T.R., Jbabdi, S., Clare, S., Stagg, C.J., Johansen-Berg, H., 2016.

Investigating the stability of fine-grain digit somatotopy in individual human participants. J. Neurosci. 36, 1113–1127. https://doi.org/10.1523/JNEUROSCI.1742-15.2016

Lu, H., Hua, J., van Zijl, P.C.M.M., 2013. Noninvasive functional imaging of cerebral blood volume with vascular-space-occupancy (VASO) MRI. NMR Biomed. 26, 932–948. https://doi.org/10.1002/nbm.2905

Markuerkiaga, I., Barth, M., Norris, D.G., 2016. A cortical vascular model for examining the specificity of the laminar BOLD signal. Neuroimage 132, 491–498. https://doi.org/10.1016/j.neuroimage.2016.02.073

Marquis, R., Jastrzębowska, M., Draganski, B., 2017. Novel imaging techniques to study the functional organization of the human brain. Clin. Transl. Neurosci. 1, 2514183X1771410. https://doi.org/10.1177/2514183X17714104

Martuzzi, R., van der Zwaag, W., Farthouat, J., Gruetter, R., Blanke, O., 2014. Human finger somatotopy in areas 3b, 1, and 2: A 7T fMRI study using a natural stimulus. Hum. Brain Mapp. 35, 213–226. https://doi.org/10.1002/hbm.22172

Menon, R.S., 2002. Postacquisition suppression of large-vessel BOLD signals in high-resolution fMRI. Magn. Reson. Med. 47, 1–9. https://doi.org/10.1002/mrm.10041

Moeller, S., Pisharady, P.K., Ramanna, S., Lenglet, C., Wu, X., Dowdle, L., Yacoub, E., Uğurbil, K., Akçakaya, M., 2021. NOise reduction with DIstribution Corrected (NORDIC) PCA in dMRI with complex-valued parameter-free locally low-rank processing. Neuroimage 226. https://doi.org/10.1016/j.neuroimage.2020.117539

Norris, D.G., Polimeni, J.R., 2019. Laminar (f)MRI: A short history and future prospects. Neuroimage. https://doi.org/10.1016/j.neuroimage.2019.04.082

Oliveira, Í.A.F., Cai, Y., Hofstetter, S., Siero, J.C.W., van der Zwaag, W., Dumoulin, S.O., 2022. Comparing BOLD and VASO-CBV population receptive field estimates in human visual cortex. Neuroimage 248, 118868. https://doi.org/10.1016/j.neuroimage.2021.118868

Oliveira, Í.A.F., van der Zwaag, W., Raimondo, L., Dumoulin, S.O., Siero, J.C.W., 2021. Comparing hand movement rate dependence of cerebral blood volume and BOLD

responses at 7T. Neuroimage 226, 117623. https://doi.org/10.1016/j.neuroimage.2020.117623

Olman, C.A., Pickett, K.A., Schallmo, M.P., Kimberley, T.J., 2012. Selective BOLD responses to individual finger movement measured with fMRI at 3T. Hum. Brain Mapp. 33, 1594–1606. https://doi.org/10.1002/hbm.21310

Penfield, W., Boldrey, E., 1937. Somatic motor and sensory representation in the cerebral cortex of man as studied by electrical stimulation. Brain 60, 389–443. https://doi.org/10.1093/brain/60.4.389

R Core Team, 2020. A Language and Environment for Statistical Computing. R Found. Stat. Comput.

Sanchez-Panchuelo, R.M., Francis, S., Bowtell, R., Schluppeck, D., 2010. Mapping Human Somatosensory Cortex in Individual Subjects With 7T Functional MRI. J. Neurophysiol. 103, 2544–2556. https://doi.org/10.1152/jn.01017.2009

Schellekens, W., Petridou, N., Ramsey, N.F., 2018. Detailed somatotopy in primary motor and somatosensory cortex revealed by Gaussian population receptive fields. Neuroimage 179, 337–347. https://doi.org/10.1016/J.NEUROIMAGE.2018.06.062

Serino, A., Akselrod, M., Salomon, R., Martuzzi, R., Blefari, M.L., Canzoneri, E., Rognini, G., van der Zwaag, W., Iakova, M., Luthi, F., Amoresano, A., Kuiken, T., Blanke, O., 2017. Upper limb cortical maps in amputees with targeted muscle and sensory reinnervation. Brain 140, 2993–3011. https://doi.org/10.1093/brain/awx242

Siero, J.C.W., Hermes, D., Hoogduin, H., Luijten, P.R., Ramsey, N.F., Petridou, N., 2014. BOLD matches neuronal activity at the mm scale: A combined 7T fMRI and ECoG study in human sensorimotor cortex. Neuroimage 101, 177–184. https://doi.org/10.1016/j.neuroimage.2014.07.002

Stringer, E.A., Chen, L.M., Friedman, R.M., Gatenby, C., Gore, J.C., 2011. Differentiation of somatosensory cortices by high-resolution fMRI at 7T. Neuroimage 54, 1012–1020. https://doi.org/10.1016/j.neuroimage.2010.09.058

Turner, R., 2002. How Much Cortex Can a Vein Drain? Downstream Dilution of Activation-

Related Cerebral Blood Oxygenation Changes. Neuroimage 16, 1062–1067. https://doi.org/10.1006/nimg.2002.1082

Uğurbil, K., 2021. Ultrahigh field and ultrahigh resolution fMRI. Curr. Opin. Biomed. Eng. 18, 100288. https://doi.org/10.1016/J.COBME.2021.100288

Uludağ, K., Blinder, P., 2016. Linking brain vascular physiology to hemodynamic response in ultra-high field MRI. Neuroimage 168, 279–295. https://doi.org/10.1016/j.neuroimage.2017.02.063

Uludağ, K., Müller-Bierl, B., Uğurbil, K., 2009. An integrative model for neuronal activity-induced signal changes for gradient and spin echo functional imaging. Neuroimage 48, 150–165. https://doi.org/10.1016/j.neuroimage.2009.05.051

van der Zwaag, W., Francis, S., Head, K., Peters, A., Gowland, P., Morris, P., Bowtell, R., 2009. fMRI at 1.5, 3 and 7 T: Characterising BOLD signal changes. Neuroimage 47, 1425–1434. https://doi.org/10.1016/j.neuroimage.2009.05.015

Vizioli, L., Moeller, S., Dowdle, L., Akçakaya, M., De Martino, F., Yacoub, E., Uğurbil, K., 2021. Lowering the thermal noise barrier in functional brain mapping with magnetic resonance imaging. Nat. Commun. 12, 5181. https://doi.org/10.1038/s41467-021-25431-8

Yacoub, E., Wald, L.L., 2018. Pushing the spatio-temporal limits of MRI and fMRI. Neuroimage 164, 1–3. https://doi.org/10.1016/j.neuroimage.2017.11.034

Chapter 5

Comparing BOLD and VASO-CBV population receptive field estimates in human visual cortex

Ícaro A.F. de Oliveira,

Yuxuan Cai,

Shir Hofstetter,

Wietske van der Zwaag,

Jeroen C.W. Siero,

Serge O. Dumoulin

Based on the publication: Oliveira, Í.A.F., Cai, Y., Hofstetter, S., Siero, J.C.W., van der Zwaag, W., Dumoulin, S.O., 2022. Comparing BOLD and VASO-CBV population receptive field estimates in human visual cortex. Neuroimage 248, 118868. https://doi.org/10.1016/j.neuroimage.2021.118868

Abstract

Vascular Space Occupancy (VASO) is an alternative fMRI approach based on changes in Cerebral Blood Volume (CBV). VASO-CBV fMRI can provide higher spatial specificity than the blood oxygenation level-dependent (BOLD) method because the CBV response is thought to be limited to smaller vessels. To investigate how this technique compares to BOLD fMRI for cognitive neuroscience applications, we compared population receptive field (pRF) mapping estimates between BOLD and VASO-CBV. We hypothesized that VASO-CBV would elicit distinct pRF properties compared to BOLD. Specifically, since pRF size estimates also depend on vascular sources, we hypothesized that reduced vascular blurring might yield narrower pRFs for VASO-CBV measurements. We used a VASO sequence with a double readout 3D EPI sequence at 7T to simultaneously measure VASO-CBV and BOLD responses in the visual cortex while participants viewed conventional pRF mapping stimuli. Both VASO-CBV and BOLD images show similar eccentricity and polar angle maps across all participants. Compared to BOLD-based measurements, VASO-CBV yielded lower tSNR and variance explained. The pRF size changed with eccentricity similarly for VASO-CBV and BOLD, and the pRF size estimates were similar for VASO-CBV and BOLD, even when we equate variance explained between VASO-CBV and BOLD. This result suggests that the vascular component of the pRF size is not dominating in either VASO-CBV or BOLD.

Introduction

The majority of functional MRI (fMRI) studies employ blood oxygenation level-dependent (BOLD) contrast (Glover, 2011; Ogawa et al., 1990). BOLD contrast reflects a combination of changes in venous blood oxygenation, cerebral blood flow (CBF), and cerebral blood volume (CBV) (Buxton et al., 2014). The Gradient Echo (GE) BOLD sequence is the typical method of choice, mainly because of its superior sensitivity, available Signal-to-Noise Ratio (SNR), and high coverage (Havlicek and Uludağ, 2020). Unfortunately, this sequence suffers from limited spatial specificity due to contamination of the functional signal with draining and pial veins effect (Kim and Ogawa, 2012; Menon, 2002; Uludağ et al., 2009).

Vascular Space Occupancy (VASO) is a non-invasive fMRI technique sensitive to changes in CBV (Lu et al., 2013, 2003). The VASO sequence and its variants take advantage of the T1 differences between arterial blood and the surrounding tissue to null the blood signal and measure CBV changes (Lu et al., 2003). An inversion recovery pulse is used to minimize blood signal while a substantial part of the tissue signal remains available for detection. The increased cerebral blood volume results in a negative signal change during the neuronal activity, caused by the tissue signal reduction in the voxel. VASO-CBV contrast promises higher microvascular specificity since it is sensitive to arteriole and post-arterial CBV changes, resulting in better spatial localization of the neuronal activity with reduced draining vein contamination than BOLD (Huber et al., 2014; Jin and Kim, 2008).

The VASO-CBV sequence variant developed by Huber (Huber et al., 2014) for 7T scanners has proven to be a highly effective alternative for high-resolution acquisitions, especially for depth-dependent applications (Beckett et al., 2020; Huber et al., 2020b, 2017, 2015; Persichetti et al., 2019; Yu et al., 2019). Another remark of the 7T VASO fMRI is that the sequence was recently validated against established preclinical imaging modalities (Huber et al., 2021). In addition, significant improvements in accelerated acquisition techniques, such as 3D EPI readout (Huber et al., 2018a) and increased spatial coverage with MAGEC VASO (Huber et al., 2020a), enabled the possibility of a broader number of applications. Multiple studies have demonstrated the feasibility of using VASO fMRI for advanced neuroimaging applications (Finn et al., 2019; Huber et al., 2020b; Lu et al., 2005). However, to date, VASO-CBV responses have

not been extended to more complex paradigms and computational models, such as population receptive field mapping.

Here, we evaluate the feasibility of VASO-CBV in the visual cortex using population receptive field (pRF) modeling (Dumoulin and Wandell, 2008). The pRF is the region of visual space that elicits a response for a given cortical location (Victor et al., 1994). The pRF analysis with fMRI has become a popular method to study the topographic organization of primary sensory neural populations and has been extended to several perceptual, cognitive, and clinical domains (Dumoulin and Knapen, 2018; Wandell and Winawer, 2015). The conventional pRF model characterizes the pRF with a two-dimensional Gaussian function with three parameters: position (x,y or eccentricity, and polar angle) and size (sigma). Both neural and non-neural components contribute to the pRF size (Dumoulin and Wandell, 2008). Neural components include both single-neuron receptive field size and positional scatter. Non-neural components include methodological aspects of head and eye movements, but also vasculature, such as hemodynamic response function (HRF) and vascular point spread function (Dumoulin and Wandell, 2008; Lerma-Usabiaga et al., 2020). Since pRF properties have both vascular and neuronal contributions and the vascular contributions to pRF size are expected to be smaller in VASO-CBV, we hypothesized that the VASO-CBV responses are more specific than BOLD responses.

Thus the present work extends the use of the VASO-CBV technique to the population receptive field modeling. The aim is to evaluate and compare VASO-CBV and BOLD pRF estimates such as eccentricity and polar angle maps in addition to the pRF size, using a standard pRF mapping approach in the visual cortex. We first used a dartboard flickering checkerboard stimuli to determine the optimal slice orientation for VASO-fMRI in the visual cortex. With the optimized slice orientation, we measured pRF estimates in visual field maps V1-V3 simultaneously using a double readout 3D-EPI VASO sequence to test the hypothesis that the higher spatial specificity of VASO-CBV would translate to smaller pRF size estimates.

Materials and methods

Participants

The measurements were obtained from six healthy participants (five females, age 32 ± 7 years [Mean ± SD]). Three participants participated in the slice orientation experiment (P01-P03). The other three volunteers participated in the pRF experiment (P04- P06). All participants had normal or corrected-to-normal visual acuity. The ethics committee of the Amsterdam University Medical Centre - location AMC approved this study, and all volunteers provided written consent before participating after being informed of the experimental procedures.

Visual Stimuli Setup

Visual stimuli were presented on a 69.84 x 39.29 cm LCD screen (Cambridge Research System) placed at the end of the scanner's bore. Participants viewed the display through a mirror mounted on top of the coil. The distance from the mirror to the display screen was 220 cm, and the display resolution was 1920 x 1080 pixels. The visual stimuli were generated in Matlab (The MathWorks, Natick, United States) using PsychToolbox Version 3 (Brainard, 1997; Kleiner et al., 2007).

Slice Orientation Experiment

We determined the optimal slice orientation for VASO fMRI in the visual cortex using a dartboard-shaped flickering checkerboard stimulus. The dartboard was subdivided into 13 rings and 24 segments, totalizing 312 sectors. These sectors changed their contrast between 2 levels of luminance (black and white) in a frequency rate of 2 Hz. Each experiment run consisted of 24 seconds of stimulation followed by 24 seconds of baseline, with an extra 12 seconds of fixation at the start of each run.

pRF Experiment

The pRF mapping paradigm was similar to that described in previous studies (Dumoulin and Wandell, 2008; Harvey and Dumoulin, 2011). The stimulus consisted of bar apertures with a moving checkerboard pattern (100% contrast) that moved across the visual field. The width of the bar subtended 1/4th of the stimulus radius (1.25°). Four bar orientations (0°, 45°, 90°, and 135°) and two different motion directions for each bar were used, giving a total of 8 different bar configurations within a given scan. The bar sweeps across the stimulus aperture in 12 TRs (when the bar orientation is 45° and 135°) followed by a mean luminance period of 4 TRs, or in

16 TRs (when the bar orientation is 0° and 90°) with no blank period. Diagonally and orthogonally oriented sweeps were interleaved during each scan.

Participants were asked to fixate on the dot (0.125 radius) in the center of the visual stimulus and press a button every time the dot color changed. The dot changed between red and green at random intervals to ensure the participant's attention to the presented stimulus. Each participant's measurement was repeated twice in two separate sessions with seven runs to obtain higher temporal SNR.

MR Sequences

A Slice-selective Slab-Inversion (SS-SI) VASO with a double 3D readout (Huber et al., 2018a, 2014; Oliveira et al., 2021b) was implemented on a 7T MRI scanner (Philips Healthcare, Best, The Netherlands). All data were acquired using an 8 channel transmit coil and a 32 channel receive coil (Nova Medical Inc, Wilmington, United States). We used a global B1 shim set from a previously assessed group of volunteers to achieve a, close to, circular polarization (quadrature) transmission mode (Oliveira et al., 2021a).

The visual cortex has a longer arterial arrival time (AAT) than other brain areas (Mildner et al., 2014). However, contamination by the inflow of non-inverted blood can be minimized if the blood T1 is much shorter than the TR (Donahue et al., 2009; Huber et al., 2018b). To minimize the inflow effect, the inversion time was kept relatively short. The timing parameters for the interleaved acquisition are TI_1/TI_2/TE/TR = 1100/2600/15/3000ms. In addition, an adiabatic inversion TR-FOCI pulse was used to ensure an effective inversion with reduced B1+ inhomogeneity (Hurley et al., 2010). The voxel size used in the present study is close to the resolution typically used in pRF modeling (Aqil et al., 2021; Cai et al., 2021b; Hofstetter et al., 2021). Data were acquired with an isotropic voxel size of 1.75 mm, FOV = 196×196×32 mm^3, matrix size = 112×112, 18 slices, partial Fourier factor = 0.78 in the phase encoding direction and $SENSE_{inplane}$ factor = 2.5 with constant flip angle, flip angle (FA) =15º. We included a fat suppression module Spectral Attenuated Inversion Recovery (SPAIR) before VASO-CBV and BOLD readout blocks with the same settings (TI = 360ms, TR = 754ms, pulse duration ~ 20ms). The vendor's specific absorption ratio (SAR) values never exceeded 65% of the local SAR limit. Both experiments used the same SS-SI-VASO sequence. For the slice orientation experiment, 100 volumes were acquired per 5 minutes run, with 1 run for each orientation, and run order

varied between participants. For the pRF experiment, 132 volumes were acquired per run, leading to a total scan time of 6 minutes and 42 seconds.

Anatomical scans were acquired in separate sessions with the MP2RAGE sequence (Marques et al., 2010; Oliveira et al., 2021a) at the isotropic resolution of 0.64 mm, $TR_{MP2RAGE}$=5500ms, TR/TE=6.2/2.2 ms, TI_1/TI_2=800/2700 ms with FA = 7º/5º. For one of the participants, a previously acquired dataset was used as an anatomical reference (0.8 mm).

We optimized the VASO-CBV scanning protocol for the visual cortex. Four different orientations of the slab, together with a change in the direction of the readout gradient orientation, were compared. Note that the slab positioning influences the amount of inflow, the amount of available tissue signal in VASO measurements and SENSE unfolding performance. The slice orientations (Fig. 1) were defined as follows: I) Aligned with the ACPC-axis (Anterior-Posterior Commissure) covering the calcarine sulcus obliquely, with the phase encoding in the Anterior-Posterior direction. II) Aligned with the calcarine sulcus with phase encoding in the Anterior-Posterior direction. III) Aligned with the superior surface of the cerebellum, covering the calcarine sulcus (coronal orientation), with phase encoding in the Right-Left direction. IV) Purely coronal slices, again with phase encoding in the Right-Left direction.

Data Analysis

Slice orientation Experiment

Raw images were corrected for head-motion, with a separate realignment for VASO and BOLD in SPM12 (Statistical Parametric Mapping) software package using default settings, followed by a BOLD correction to account for the T2* dependency in the VASO images (Huber et al., 2014). The optimal slice orientation for VASO fMRI in the visual cortex was determined by the highest level of activation represented by the highest average Z-scores obtained from FEAT (FSL, v.6.0). The region of interest (ROI) definition consisted of the shared VASO-CBV activated voxels within gray matter in all orientations with a minimum Z-score of 1.5, which we will dub as overlap ROI. The Z-score differences were assessed using a one-way repeated

measures ANOVA with post-hoc Holm correction. In addition, we also evaluated the Temporal Signal-to-Noise Ratio (tSNR) using two cubic ROIs (12 × 12 × 12 mm) in the visual cortex. The tSNR differences were also assessed using one-way repeated ANOVA with the same post-hoc analysis.

pRF Experiment

T1w images were segmented into gray and white matter using cbs-tools (Bazin et al., 2014) and resampled to a 1 mm isotropic resolution. The pre-processing steps were the same as in the slice orientation experiment. No additional spatial smoothing or temporal filtering was applied to minimize the loss in specificity.

Pre-processed functional data were then analyzed in the vistasoft software (https://github.com/vistalab/vistasoft). The first four volumes of the functional data were discarded to ensure steady-state magnetization. The first VASO-CBV volume was aligned to the segmented anatomy, resulting in a 4 × 4 transform matrix in each session. Individual functional images in the session were co-registered to the same anatomical space using the same transformation. VASO-CBV and BOLD functional data were averaged across runs, respectively. Since the VASO-CBV mechanism generates a negative intensity response, all VASO-CBV time series were flipped by removing the mean, inverting the signal polarity, and adding the mean.

We estimated the population receptive field position and sizes using the conventional Gaussian pRF model (Dumoulin and Wandell, 2008). First, the functional response of each voxel is predicted using a two-dimensional Gaussian pRF model. The predicted fMRI time course is calculated by the convolution of the modeled pRF, the stimulus sequence, and a canonical BOLD HRF (Boynton et al., 1996; Friston et al., 1998). The quantitative pRF parameters for each voxel are determined by minimizing the residual sum of squared errors (RSS) between the predicted and the observed fMRI time series. After estimating these pRF parameters, we estimated the HRF parameters by minimizing the RSS between the predicted and the observed responses over the visual cortex, where the pRF model explained > 10% of the variance in the data. We used the new HRF to refine the pRF estimates (Harvey and Dumoulin, 2011). We

analyzed the data both with and without the final HRF fit stage. The results were similar (Supplementary Fig.1).

We included voxels for further analysis based on two criteria. First, we only used voxels in V1, V2, and V3. Second, we limited the analysis to those voxels where the R^2 corresponded to a p-value less than 0.05 in the VASO data. The variance explained (R^2) was converted to p-values using the same principle as shown in (Hofstetter and Dumoulin, 2021). We created a null distribution using the same model-fitting procedure on voxels taken from the white matter (WM) pooled across participants (P04: 44912 voxels; P05: 40920 voxels, and P06: 67890 voxels). For each variance explained, the proportion of these voxels with model fits were calculated. The variance explained of the pRF model was 21%, resulting in an equivalent probability of 0.048 of observing this goodness of fit by chance. Note that using these criteria, we are not excluding the possibility of including voxels in the ROI that have below-threshold variance explained in the BOLD data. For P04, this is the case in less than 1% of the voxels in each ROI (V1, V2, and V3). For P05, in V1, and V3, less than 1% of the voxels had lower than 21% of variance explained, and 2% in V2. For P06, all voxels had higher than 21% of the variance explained in BOLD data.

Next, population receptive field sizes were estimated as a function of eccentricity for V1, V2, and V3. We used unbinned data to estimate the best linear relationship (slope and offset) and used data between 0.5-4.5 visual degrees to avoid pRFs close to the fovea and to account for the boundaries of the stimulus display. The data was binned for visualization purposes only. To assess BOLD and VASO-CBV pRF size differences, the pRF size from the central eccentricity was calculated using the slope and intercept values per participant and per ROI (V1-3). The comparison was performed between each BOLD run separately against the averaged VASO (14 runs) to approximate the variance explained. A one-way Bayesian ANOVA using JASP software was used to assess the statistical differences (JASP team, 2021). The Pearson's correlation and the plots were generated in R (R Core Team, 2020).

Noise level assessment

The noise level was evaluated using two metrics: tSNR and variance explained (Cai et al., 2021a). For both metrics, the quantification was calculated as a function of the number of runs. The tSNR was separately estimated for the BOLD and VASO time series after motion correction

and co-registration between both sessions. Gray and white matter masks were defined as the intersection of the relevant output of the segmentation of the anatomical data with the functional slab. The tSNR was calculated cumulatively across runs, the BOLD and VASO tSNR was calculated as the mean value across gray matter (GM) and white matter (WM) divided by the standard deviation across the same regions. The order of the runs was randomized within ten iterations. The variance explained was estimated per voxel by computing the variance after fitting the BOLD and VASO-CBV time series separately with the model prediction of a given voxel. The voxel's prediction of a single BOLD run was used as the model prediction for BOLD and VASO-CBV datasets. For the variance explained assessment, only voxels in V1 were used. The order of the runs was also randomized within ten iterations.

Results

Optimal slice orientation for VASO-CBV

We evaluated four different slice orientations to find the optimal orientation for visual responses in a VASO-CBV experiment: I) Aligned with the Anterior-Posterior Commissure covering the calcarine sulcus with the phase encoding in the Anterior-Posterior direction, II) parallel to the calcarine sulcus with phase encoding in the Anterior-Posterior direction, III) aligned with the cerebellar superior surface, with phase encoding in the Right-Left direction, and IV) perpendicular to the calcarine sulcus (coronal orientation) with phase encoding in the Right-Left direction (Fig. 1A). Fig. 1A shows the four slice orientation planes (I-IV). Figure 1B shows VASO-CBV activated voxels ($z > 2.5$) within the shared volume of all orientations, overlaid on the anatomical data. Robust VASO-CBV responses in the visual cortex were detected in all participants for all orientation planes (Fig.1B).

We summarized the slice orientation results by computing the average response into Z-scores within the overlap ROI. The results of the slice orientation experiment are shown in Fig.1C and D, for individual participants and averaged across participants, respectively. The third slice orientation option (III) yielded the highest average Z-scores across individual and group averaged data. The Z score of orientation III was significantly different than the other orientations. The post hoc Holm correction showed differences between I vs III: $p<0.001$, II vs III: $p= 0.016$, III vs IV: $p=0.04$. There was also a significant difference between I and IV ($p=0.04$).

Supplementary Fig.2A shows an example of tSNR maps for one of the participants (P02) across all four orientations and the group mean across participants. The tSNR values were higher for orientation III, with no statistical significance difference. In addition, we observed insufficient fat suppression in the EPI readout for all three participants, which led to larger ghosting, notably for orientation II (Supplementary Fig.2B). Supplementary Fig.2B shows a direct comparison between orientation II and III. We did not observe ghosting artifacts due to insufficient fat suppression for the other orientations. Hence, all subsequent experiments used an orientation of the slab aligned with the superior surface of the cerebellum, covering the calcarine sulcus in a coronal-oblique plane with the phase-encoding direction along the right-left axis.

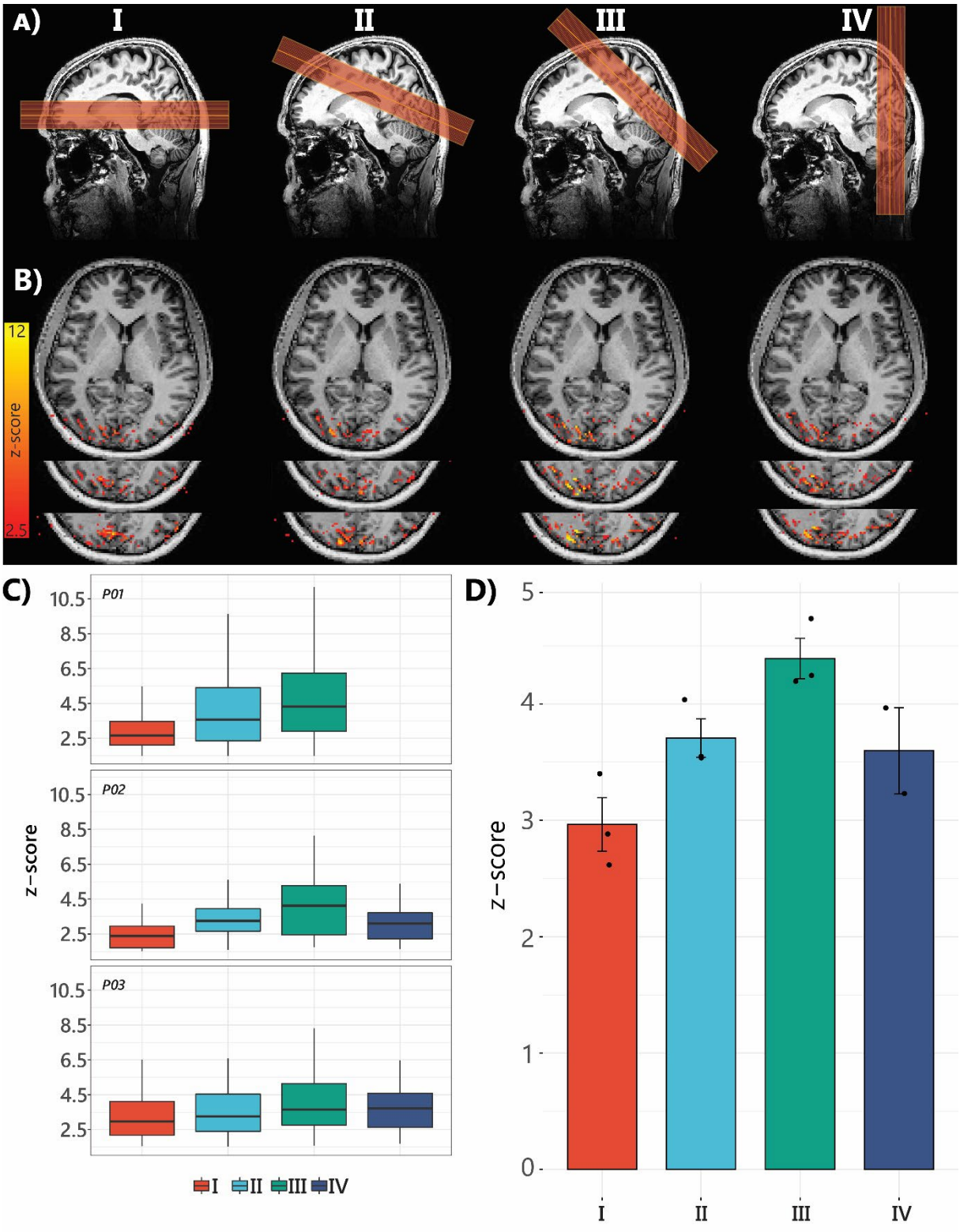

Fig.1. We evaluated four different slice orientations to find the optimal orientation for visual responses in a VASO-CBV experiment. A) Four slice orientations: I) Aligned with the Anterior-Posterior Commissure with the phase encoding in the Anterior-Posterior direction, II) parallel to the calcarine sulcus with phase encoding in the Anterior-Posterior direction, III) aligned with the cerebellar superior surface, with phase encoding in the Right-Left direction, and IV) perpendicular to the calcarine sulcus with phase encoding in the Right-Left direction. In all

orientations, the calcarine sulcus was included in the slab. B) VASO-CBV activated voxels (z > 2.5) within the shared volume of all orientations, overlaid on the anatomical data. C) Boxplot of the Z-scores within the overlap ROI per participant. D) Z-score averaged across participants (the data points represent each participant). Both in single participants and averaged data, slice orientation (III) yielded the strongest signals.

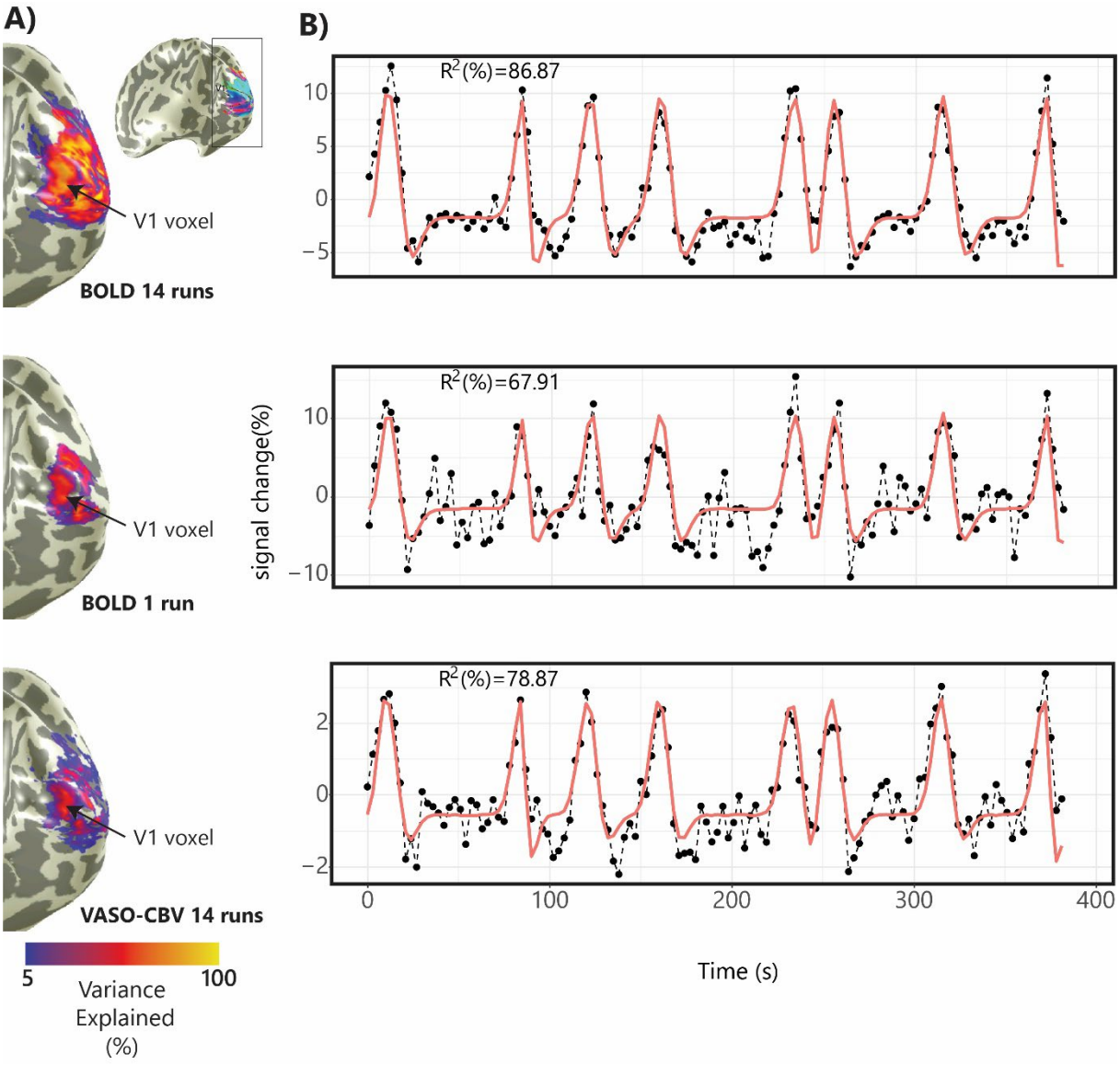

Fig.2. Example time courses and variance explained maps for VASO-CBV and BOLD. V1 is outlined on top of a polar angle map from a representative participant. A) Map of the variance explained by the pRF model for 14-run average VASO-CBV and two BOLD examples, one averaged over 14 runs and a single run. B) An example pRF fMRI responses from a voxel located in V1, for VASO-CBV, averaged over 14 runs and two BOLD examples, one averaged over 14 runs and a single run. The dashed lines with bullet points represent the measured response, and the red line represents the model prediction. R^2 denotes the amount of variance explained by the model for the selected voxel.

VASO-CBV and BOLD Population Receptive Field responses

The variance explained maps show the fMRI signal quality captured by the pRF model (Fig.2). These responses covered the target visual area (V1-V3) for all three examples, although the 14-run average BOLD shows more robust voxel responses. The single BOLD run shows a lower but still a comparable explained variance. For VASO-CBV, the extension of the variance explained map is similar to the single BOLD run. The example voxel was selected to have a high variance explained (R^2=78.87%) in the VASO-CBV responses and was directly compared to the BOLD responses in the same voxel, in a single run, averaged over 14 runs. The VASO-CBV time series exhibits a lower response amplitude than the BOLD time series. The single BOLD run has a comparable signal change to the 14-average BOLD run but has a much higher noise floor, leading to a worse model fit and lower R^2 value. Note that the difference in amplitude for BOLD and VASO-CBV is expected and reflects their sensitivity differences.

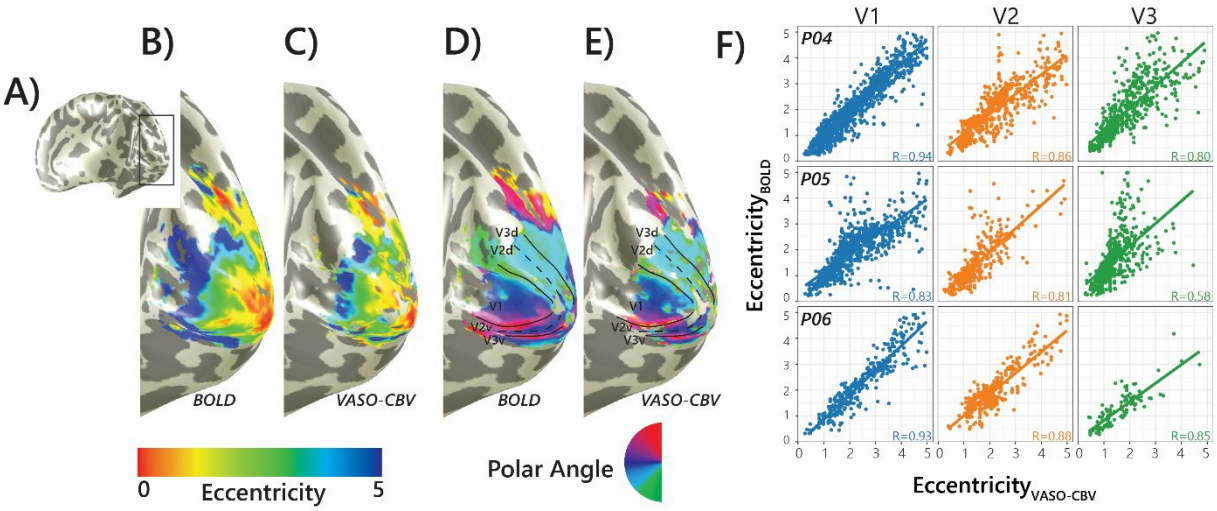

Fig.3. pRF position estimates on an inflated cortical surface. A.) The visual area (occipital pole) is indicated on the inflated cortical surface. The eccentricity maps are shown for BOLD (B) and VASO-CBV (C). Polar angle maps are likewise compared between BOLD (D) and VASO-CBV (E). Maps are threshold at a variance explained of 5%. F) Correlations between eccentricity values obtained from BOLD and VASO-CBV indicate a similar progression of pRF values across eccentricity between the two sequences. R-value is the Pearson correlation coefficient.

The pRF visual field maps are shown in Fig.3. BOLD pRF maps show the expected pattern of a complete visual field representation (Dumoulin and Wandell, 2008). VASO-CBV maps show

a similar pattern for eccentricity and polar angle. The similarity between BOLD and VASO-CBV pRFs was quantified using a Pearson's correlation test on the eccentricity values (Fig.3F). The correlation was strong and statistically significant for all regions and participants at ($R = 0.83 \pm 0.11$ [Mean ± SD], $p<0.0001$). Most slope values of the fits were close to the unity line, where eccentricity equates between VASO-CBV and BOLD (>0.9). Apart from V3 for P04 and P05; and V2 for P05, the measured slope was 0.73, 0.38, and 0.72, respectively. The pRF maps for the other two participants are depicted in Supplementary Fig.3. These results show that pRF maps can be obtained reliably with VASO-CBV as well as with BOLD.

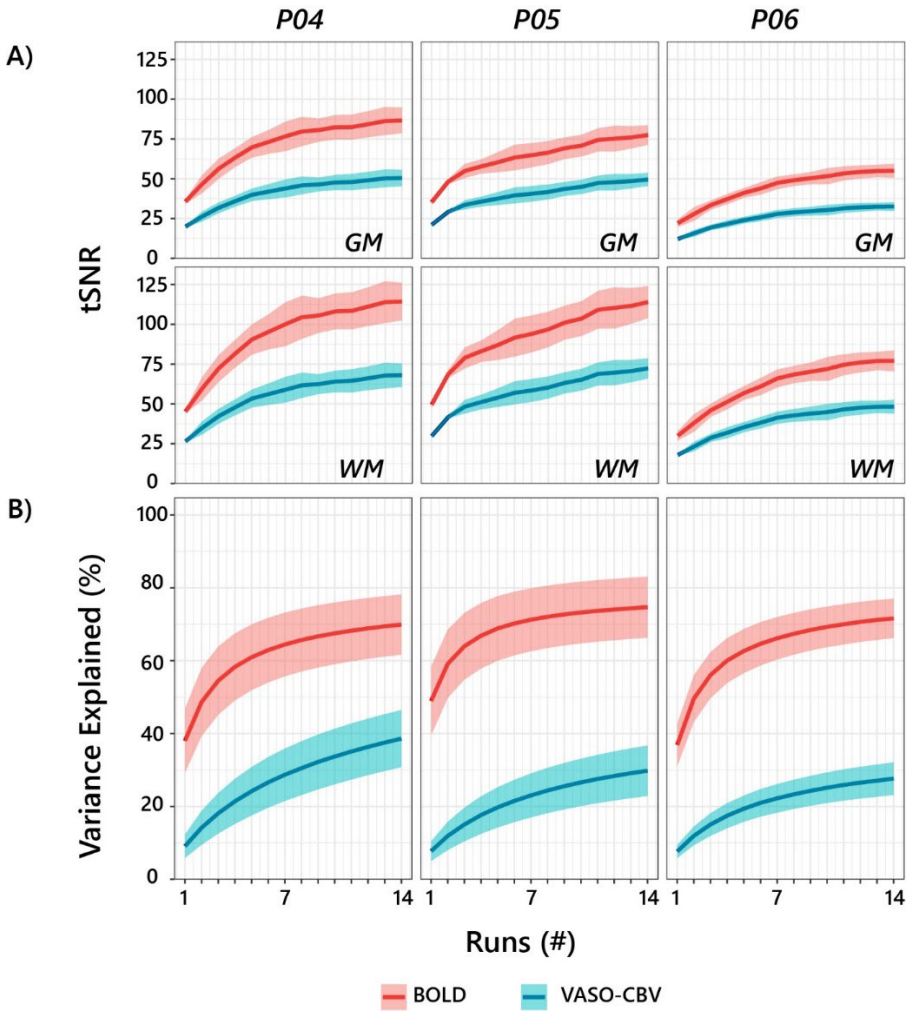

Fig.4. Quantification of the noise level assessed by tSNR and variance explained as a function of the number of runs. A) The tSNR increases with the number of averaged runs for all participants and both tissue types in similar proportions. BOLD tSNR is higher than VASO-CBV for all regions and participants. B) The increase in variance explained is not at the same rate and amplitude for BOLD and VASO-CBV. For BOLD, variance explained plateaus earlier than

the VASO-CBV variance explained, but the levels of variance explained by BOLD are consistently higher.

Fig.4. shows the tSNR (Panel A) and variance explained (Panel B) as a function of the number of runs for BOLD and VASO-CBV. For both BOLD and VASO-CBV, the tSNR increases with the number of runs for both regions and participants in similar proportions with higher values for BOLD than VASO-CBV. Note that the differences between gray and white matter are most likely caused by the stimulus-driven signal fluctuations in the gray matter, baseline signal intensity, and non-task-related BOLD signal fluctuations, all leading to lower tSNR values in the gray matter relative to the white matter. The variance explained in V1 does not increase at the same rate and amplitude for both acquisitions: For BOLD, the same selected voxels can reach 70% variance explained at a cumulative sum of 14 runs (average), whereas the VASO-CBV explained variance in the same voxels approaches 30%, approximately the same variance explained as a single run of BOLD data.

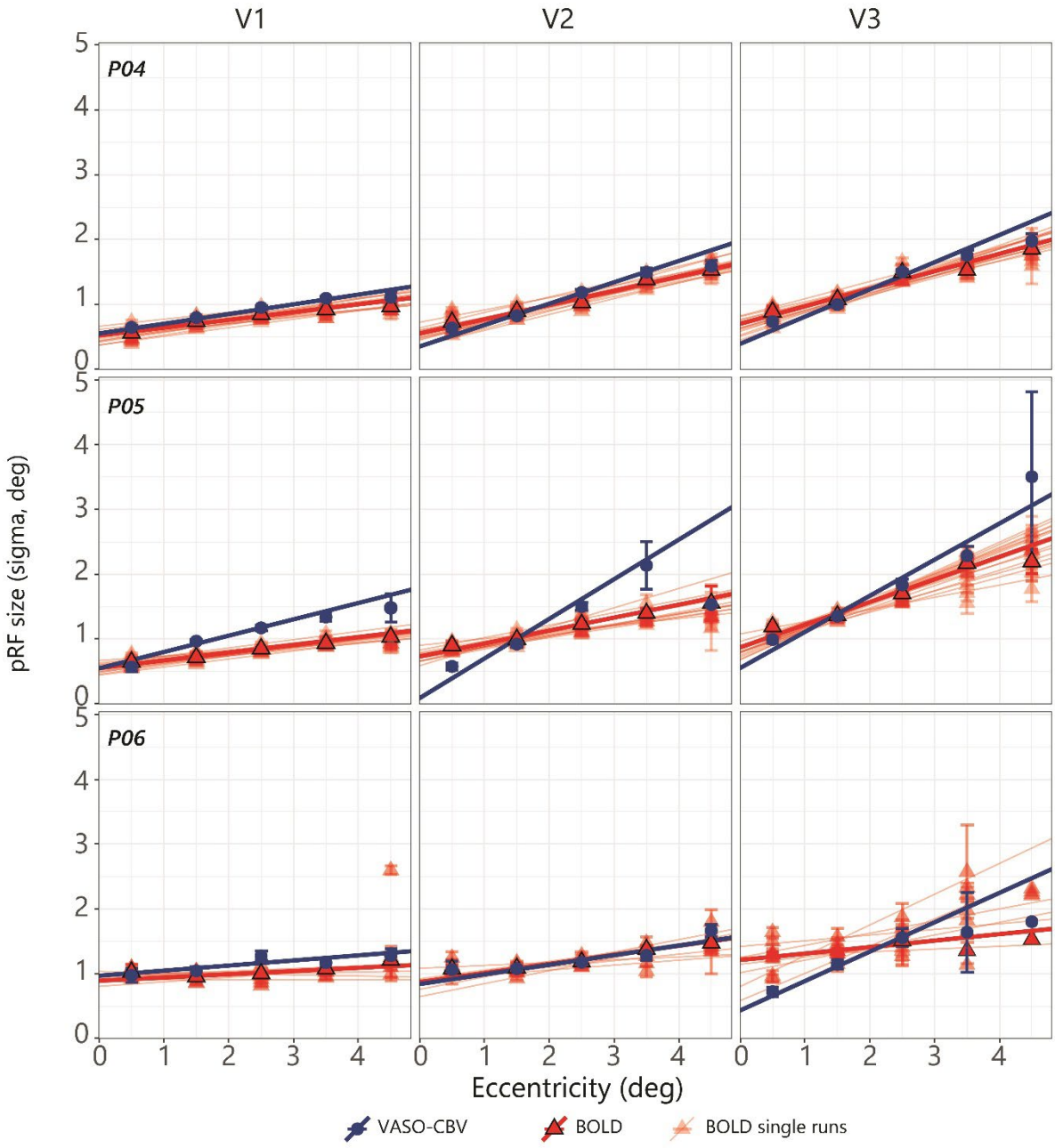

Fig.5. pRF size changes across eccentricity in V1, V2, and V3 for all participants, for the averaged VASO-CBV 14 runs, the averaged BOLD 14 runs, and the individual BOLD runs. pRF sizes increase with visual field eccentricity and across the visual area hierarchy.

The comparison of pRF sizes obtained from BOLD and VASO-CBV runs was performed between the 14-run averaged VASO-CBV data and for each BOLD run to maintain similar levels of variance explained. A linear increase of pRF size with eccentricity is expected for all visual field areas, with increasing slopes for more downstream areas (Dumoulin and Wandell, 2008). As expected, the pRF size increases as a function of eccentricity for both BOLD and VASO-CBV

(Fig.5). The slope of this function increases from V1 to V3 in almost all volunteers. The only exception is P05, presenting a nearly similar slope for V2 and V3. However, in contrast to our hypothesis, we did not observe smaller pRF sizes derived from VASO-CBV than BOLD-derived pRF sizes. A one-way Bayesian ANOVA was performed to test the differences between pRF size in BOLD and VASO-CBV. In the Bayesian framework, the alternative hypothesis is the difference in the means between the averaged 14 VASO-CBV and the individual BOLD runs. We defined the alternative hypothesis as the difference between the averaged 14 VASO-CBV and the individual BOLD runs. The Bayesian ANOVA indicated weak evidence for the alternative hypothesis in V1 (BF_{10}=2.687). Moreover, no evidence was found for the alternative hypothesis in V2 (BF_{10}=1.044) and V3 (BF_{10}=0.477). These results indicate that the pRF sizes for BOLD and VASO-CBV are not significantly different.

Discussion

Overview of the results

In the present study, we evaluated the feasibility of VASO-CBV 7T fMRI for pRF mapping. The SS-SI VASO sequence with 3D EPI readout enabled us to simultaneously acquire BOLD and VASO-CBV responses in the visual cortex. Because of the longer arterial arrival time of the visual cortex, we firstly aimed at the slice optimization of the VASO-fMRI sequence. The optimal orientation that yielded a higher activation level (Z-score) was used in the pRF mapping experiment. We found similar pRF positions, i.e. eccentricity and polar angle, for VASO-CBV and BOLD derived maps. Likewise, the pRF size changed with eccentricity in V1-V3 for VASO-CBV and BOLD in a similar manner. Because of its distinct sensitivity to microvascular blood volume changes, we anticipated that VASO-CBV would show smaller pRF sizes than BOLD. However, we found very similar pRF size estimates for BOLD and VASO-CBV. These results suggest that, for the spatial resolution used here, the vascular component of the pRF size is not dominating in either VASO-CBV or BOLD.

Slice optimization

The way the CBV contrast is generated in VASO-CBV images implies limitations in acquisition parameters. The readout blocks have to be timed so that the blood signal is nulled or close to zero, e.g., a certain time after the inversion pulse. During this time, fast inflowing blood may enter the slab if vessels transport non-inverted blood fast enough to the area of interest. The so-called inflow effects lead to bright signals in small arteries and an unwanted Cerebral Blood Flow (CBF) contribution, resulting in low sensitivity to CBV changes. At the same time, we assume that all blood is replenished before the BOLD weighted image is acquired (~1.5s after inversion). The manifestation of the inflow effect depends on several experimental conditions, including the transmit coil coverage, inversion time, and functional task. For example, the arterial arrival time is expected to be shorter during the task because of the dilatation of the vessels and the changes in the flow velocity. For the visual cortex, the arterial arrival time is much longer than in the more superior motor cortex (Mildner et al., 2014), potentially affecting blood refilling in an occipital imaging slab.

Here, we positioned the slice orientation to ensure that the slab covered V1, V2, and V3 used a short TI to limit inflow effects in VASO-CBV images even during the task, while sufficient refilling occurred to achieve good VASO-CBV sensitivity. The coverage of the transmit coil determines the area of tissue in which a complete inversion of the signal is achieved and does not differ between slice orientations. We did not observe indications of inflow artifacts in any of the orientation planes. Nevertheless, the absence of clearly visible inflow artifacts is not complete evidence of no residual inflow effect in the data (Huber et al., 2018b).

Still, orientation III yielded higher z-scores than the other orientations. One possible cause for this difference was the quality of the fat suppression when compared with orientation II (Supplementary Fig.2). Although not significant, the tSNR measured in the visual area was also higher for orientation III. The proximity and distribution of the channels in the receive coil could also contribute to this result, as SNR and SENSE unfolding depend heavily on the architecture of the rf-coil (Hendriks et al., 2020). Noteworthy, we believed that these findings might depend on other aspects of the sequence. A different spatial resolution might result in a different optimal slice orientation than found here, especially for small voxel sizes where peripheral nerve stimulation (PNS) limits the maximum gradient strength and slew rate. Note

that the gradient strength did not limit our experiment, and the PNS level was low according to the vendor measurements.

tSNR and variance explained differences

Another challenge for the VASO sequence is the inherent lower SNR. In the present study, VASO-CBV tSNR was consistently lower than BOLD. A previous study observed similar behavior using similar spatial resolution and readout strategies in the motor area (Huber et al., 2018a). The tSNR curves in Fig.4A reveal that, in general, a single BOLD run is equivalent to 4-5 average runs of VASO-CBV. This low tSNR value limits the detection of VASO fMRI signal activation and increases the experimental time compared to typical BOLD acquisitions. The pRF model performance was measured by the variance explained (R^2). For both VASO-CBV and BOLD, the variance explained increases with the number of runs, although in different ratios, with BOLD reaching a plateau earlier than VASO-CBV. Therefore, we compared the average of 14 runs of VASO-CBV to individual BOLD runs in the pRF size analysis.

A promising approach for further VASO-CBV improvements is using denoising techniques, for example, the recently proposed noise reduction with distribution corrected PCA (NORDIC PCA) (Moeller et al., 2021). NORDIC PCA denoising targets the removal of the thermal noise contribution to fMRI, leading to improvements in temporal SNR, functional signal detection (more significant activated voxels), and accuracy of functional maps (Vizioli et al., 2021). Such a denoising technique could improve VASO-CBV tSNR resulting in reduced acquisition times with fewer runs. Of course, BOLD runs also benefit from denoising, and the need to average higher numbers of runs for VASO-CBV might not change.

VASO-CBV and BOLD pRF estimations

Polar angle and eccentricity maps derived from BOLD contrast were consistent with previous fMRI findings (Dumoulin and Wandell, 2008). The maps derived from VASO-CBV contrast were similar, but because of the lower tSNR less spatially extensive than BOLD at a given threshold (Supplementary Fig.3). Our results show that VASO-CBV eccentricity has a

strong correlation with BOLD eccentricity (Fig.3). The pRF tuning width changed with the eccentricity (Fig.5) in V1-V3 for all three participants, similarly for BOLD and VASO-CBV. The pRF variations observed here correspond to the same pattern as in previous reports (Dekker et al., 2019; Dumoulin and Wandell, 2008; Harvey and Dumoulin, 2011). Interestingly, pRF size measurements for VASO-CBV are not smaller than BOLD. The expected higher microvascular specificity of VASO-CBV does not directly result in smaller pRF size estimates for the present pRF experiment.

The pRF size estimate depends on a combination of two types of signal components; neural and non-neural. For the neural component, the position scatter of the individual receptive fields of the recorded neural population contributes to the overall pRF size (Dumoulin and Wandell, 2008). Since the comparison was performed in the same cortical locations, the position scatter is not expected to differ in VASO-CBV compared to BOLD. The non-neural components have different origins: Previous studies showed that eye movements could cause an increase in the pRF size (Klein et al., 2014; Levin et al., 2010). Similarly, head movement-related motion artifacts add noise to the measured responses and reduce the model prediction accuracy, leading to broader measured pRF sizes. Because VASO-CBV and BOLD signals are collected within the same functional run, movement related artifacts are not likely to differ between VASO-CBV and BOLD. Additionally, the V1-3 pRF size variations (Fig.5) are similar to previous studies (Dumoulin and Wandell, 2008), which provide further evidence that these methodological aspects did not dominate our results. Last, another factor that may influence the observed pRF size estimate is the SNR (Lerma-Usabiaga et al., 2020). However, the high SNR case of 14-run averaged BOLD shows no difference in observed pRF size of single run pRF estimates (Fig 5), therefore, we do not think that variations in SNR were a factor of influence.

The hemodynamic response properties may also influence the pRF size measurements (Dumoulin and Wandell, 2008; Klein et al., 2014; Lerma-Usabiaga et al., 2020). To investigate the impact of the HRF, we added an HRF fit procedure in addition to the pRF parameters estimation (Harvey and Dumoulin, 2011). For comparison, we also analyzed the pRF sizes obtained using the canonical HRF. The results with the canonical HRF and fitted HRF are near identical (see Supplementary Fig.1). Taking these results together, we do not believe that the HRF properties affected the VASO and BOLD pRF size.

Therefore, our results suggest that either (1) the spatial vascular contributions to VASO-CBV and BOLD signals do not differ or (2) that the vascular contributions to the pRF estimates are small. We favor the second explanation. First, there are ample studies suggesting different vascular contributions to the VASO-CBV and BOLD signals (Huber et al., 2017, 2021; Jin and Kim, 2008). Second, the pRF estimates from BOLD fMRI and direct neural recordings are similar in the same subjects, both in humans (Harvey et al., 2013; Hermes et al., 2017) and primates (Klink et al., 2021). Furthermore, these pRF estimates match the spatial location of electrically induced visual sensations further linking pRF measurements with perception (Winawer and Parvizi, 2016). Thus, we suggest that pRF measurements are dominated by neural components and that the vascular contribution to the pRF size measurements are minimal and thus pRF estimates derived from VASO-CBV and BOLD signals will be similar.

These findings are specific for the experimental setup used in the present study, including the spatial resolution used here. Higher spatial resolutions, e.g. 1 mm or lower, may elicit different pRF size estimates, especially if investigated across cortical depth where the VASO-CBV specificity is more pronounced since it is much less sensitive to the draining vein effect than BOLD. Thus, we speculate that in a situation in which both the neural component of the pRF decreases in size and VASO-CBV is less sensitive to the large draining veins, there may be a difference between pRF estimates derived from BOLD and VASO-CBV. However, the VASO-CBV experiments would become practically unfeasible in terms of scan time.

Conclusion

In the present study, we investigate how VASO-CBV compares to BOLD fMRI for cognitive neuroscience applications. We compared population receptive field (pRF) mapping estimates between BOLD and VASO-CBV by extending the pRF mapping method to VASO-CBV fMRI at 7T. We simultaneously obtained VASO-CBV and BOLD weighted fMRI using a double readout 3D SS-SI-VASO sequence. The VASO-CBV reliably shows similar polar angle and eccentricity maps to BOLD-based data. The pRF size increased systematically, both with eccentricity and going from V1 to V3, with a high similarity between BOLD and VASO-CBV measured pRF sizes. The expected higher microvascular specificity of VASO-CBV did not directly result in a smaller

pRF size. These results suggest that the vascular contribution in the spatial pRF size is minimal or very similar for VASO-CBV and BOLD for the spatial resolution used here.

Supplementary material

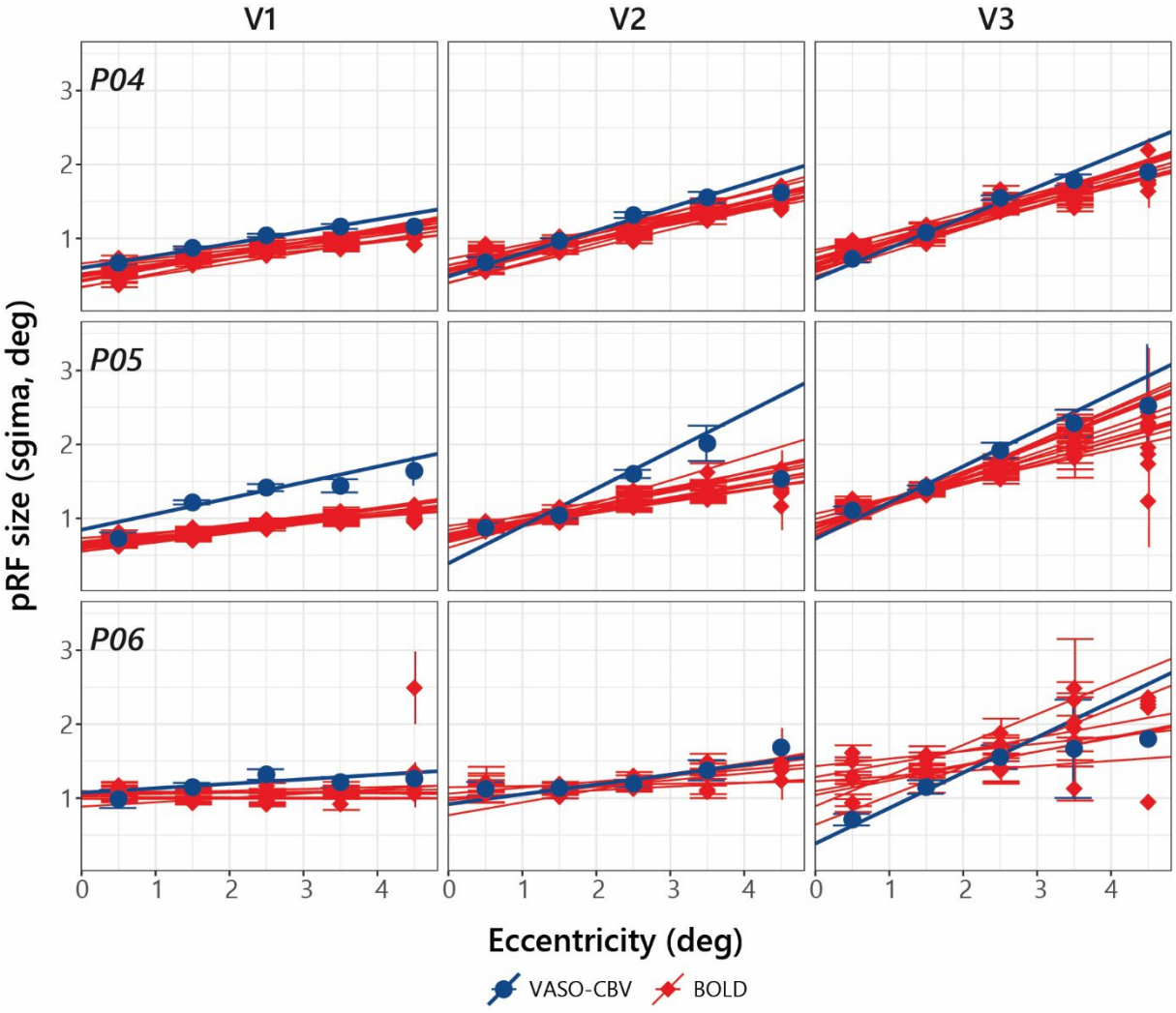

Supplementary Fig.1: pRF size estimates across visual field eccentricity in voxels from V1, V2, and V3 for all participants, for the canonical HRF. Average VASO-CBV time course and the 14 BOLD runs were plotted separately. For the canonical HRF, pRF sizes also increased with visual field eccentricity and between visual areas. A one-way Bayesian ANOVA was also performed to check the differences between pRF size in BOLD and VASO-CBV. The alternative hypothesis was that the means are different, and the results indicated strong evidence that the means are different in V1 (BF_{10}=11.094). Weak evidence that the means are different in V2 (BF_{10}=2.898), and no difference between the means in V3 (BF_{10}=0.477).

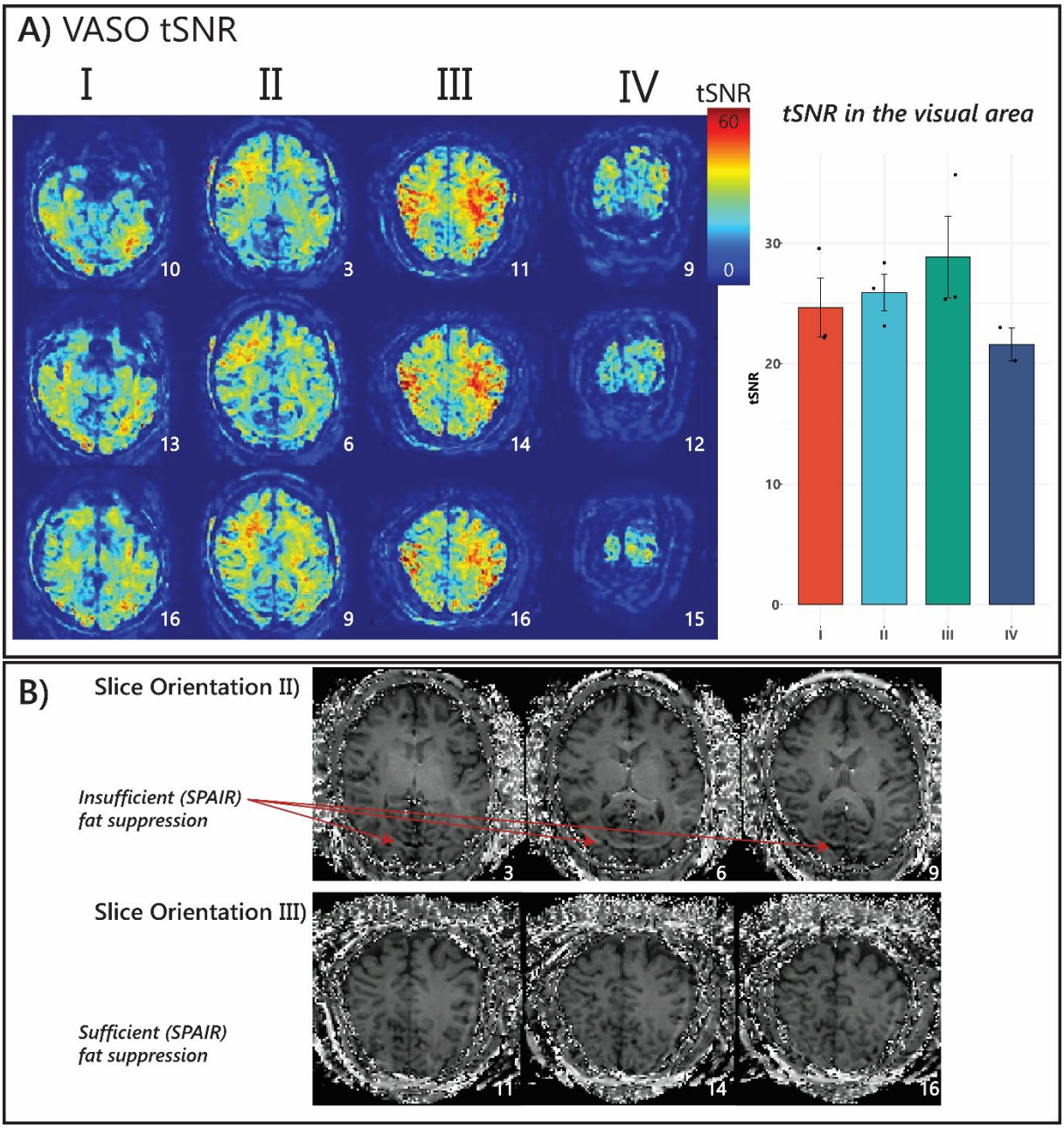

Supplementary Fig.2: Example of VASO tSNR maps for all four slice orientations: I) Aligned with the Anterior-Posterior Commissure with the phase encoding in the Anterior-Posterior direction, II) parallel to the calcarine sulcus with phase encoding in the Anterior-Posterior direction, III) aligned with the cerebellar superior surface, with phase encoding in the Right-Left direction, and IV) perpendicular to the calcarine sulcus with phase encoding in the Right-Left direction. In all orientations, the calcarine sulcus was included in the slab. We also calculated the tSNR in the visual area (two cubic ROIs positioned in the visual cortex, 12×12×12 mm). The orientation III) also shows higher signal stability than all other orientations, although with no statistical significance. We also observed insufficient fat suppression in the EPI readout, which led to larger ghosting, especially for orientation II).

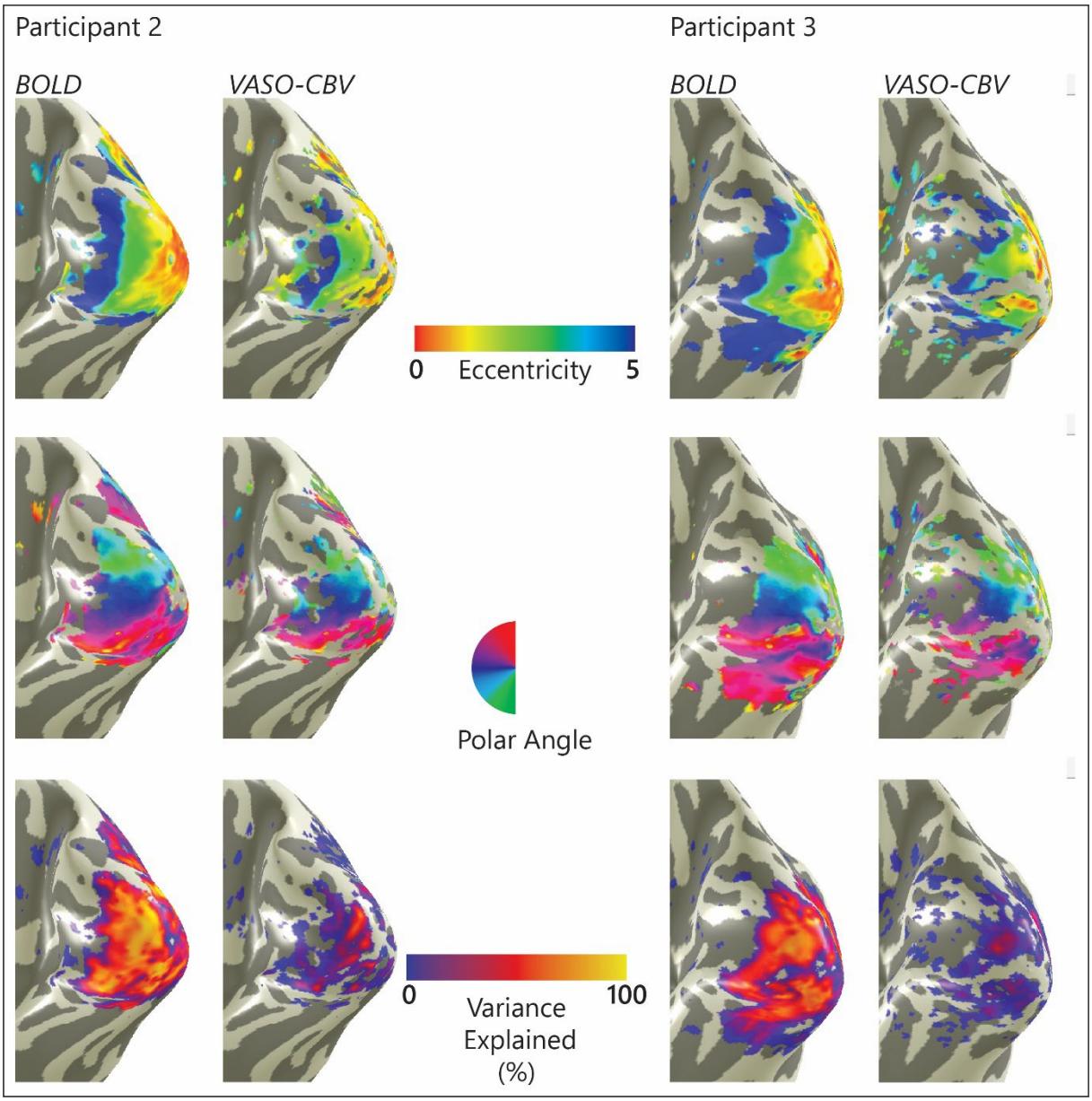

Supplementary Fig.3: Comparison of VASO-CBV and BOLD estimates for participants 2 and 3. All maps were projected on an inflated brain mesh. The threshold used for both VASO-CBV and BOLD and Eccentricity and Polar Angle maps was a variance explained of 5%. For participants 2 and 3, VASO-CBV maps show a highly similar pattern for eccentricity and polar angle. However less extensive than BOLD maps. The variance explained maps show that the pRF model performance is markedly low for VASO compared with BOLD. Note that the qualitative comparison is between 14 average VASO-CBV runs versus also 14 average BOLD runs.

References

Aqil, M., Knapen, T., Dumoulin, S.O., 2021. Divisive normalization unifies disparate response signatures throughout the human visual hierarchy. Proc. Natl. Acad. Sci. 118, e2108713118. https://doi.org/10.1073/pnas.2108713118

Bazin, P.-L., Weiss, M., Dinse, J., Schäfer, A., Trampel, R., Turner, R., 2014. A computational framework for ultra-high resolution cortical segmentation at 7Tesla. Neuroimage 93, 201–209. https://doi.org/10.1016/j.neuroimage.2013.03.077

Beckett, A.J.S., Dadakova, T., Townsend, J., Huber, L., Park, S., Feinberg, D.A., 2020. Comparison of BOLD and CBV using 3D EPI and 3D GRASE for cortical layer functional MRI at 7 T. Magn. Reson. Med. mrm.28347. https://doi.org/10.1002/mrm.28347

Boynton, G.M., Engel, S.A., Glover, G.H., Heeger, D.J., 1996. Linear systems analysis of functional magnetic resonance imaging in human V1. J. Neurosci. 16, 4207–4221. https://doi.org/10.1523/jneurosci.16-13-04207.1996

Brainard, D.H., 1997. The Psychophysics Toolbox. Spat. Vis. 10, 433–436. https://doi.org/10.1163/156856897X00357

Buxton, R.B., Griffeth, V.E.M.M., Simon, A.B., Moradi, F., 2014. Variability of the coupling of blood flow and oxygen metabolism responses in the brain: a problem for interpreting BOLD studies but potentially a new window on the underlying neural activity. Front. Neurosci. 8, 1–6. https://doi.org/10.3389/fnins.2014.00139

Cai, Y., Hofstetter, S., van der Zwaag, W., Zuiderbaan, W., Dumoulin, S.O., 2021a. Individualized cognitive neuroscience needs 7T: Comparing numerosity maps at 3T and 7T MRI. Neuroimage 237, 118184. https://doi.org/10.1016/j.neuroimage.2021.118184

Cai, Y., Hofstetter, S., van Dijk, J., Zuiderbaan, W., van der Zwaag, W., Harvey, B.M., Dumoulin, S.O., 2021b. Topographic numerosity maps cover subitizing and estimation ranges. Nat. Commun. 2021 121 12, 1–10. https://doi.org/10.1038/s41467-021-23785-7

Dekker, T.M., Schwarzkopf, D.S., de Haas, B., Nardini, M., Sereno, M.I., 2019. Population receptive field tuning properties of visual cortex during childhood. Dev. Cogn. Neurosci.

37. https://doi.org/10.1016/J.DCN.2019.01.001

Donahue, M., MacIntosh, B., Sideso, E., Bright, M., Kennedy, J., Handa, A., Jezzard, P., 2009. Absolute cerebral blood volume (CBV) quantification without contrast agents using inflow vascular-space-occupancy (iVASO) with dynamic subtraction. Proc. 17th Sci. Meet. Int. Soc. Magn. Reson. Med. Honolulu, 627.

Dumoulin, S.O., Knapen, T., 2018. How visual cortical organization is altered by ophthalmologic and neurologic disorders. Annu. Rev. Vis. Sci. 4, 357–379. https://doi.org/10.1146/annurev-vision-091517-033948

Dumoulin, S.O., Wandell, B.A., 2008. Population receptive field estimates in human visual cortex. Neuroimage 39, 647–660. https://doi.org/10.1016/j.neuroimage.2007.09.034

Finn, E.S., Huber, L., Jangraw, D.C., Molfese, P.J., Bandettini, P.A., 2019. Layer-dependent activity in human prefrontal cortex during working memory. Nat. Neurosci. 22, 1687–1695. https://doi.org/10.1038/s41593-019-0487-z

Friston, K.J., Josephs, O., Rees, G., Turner, R., 1998. Nonlinear event-related responses in fMRI. Magn. Reson. Med. 39, 41–52. https://doi.org/10.1002/mrm.1910390109

Glover, G.H., 2011. Overview of Functional Magnetic Resonance Imaging. Neurosurg. Clin. N. Am. 22, 133–139. https://doi.org/10.1016/j.nec.2010.11.001

Harvey, B.M., Dumoulin, S.O., 2011. The relationship between cortical magnification factor and population receptive field size in human visual cortex: Constancies in cortical architecture. J. Neurosci. 31, 13604–13612. https://doi.org/10.1523/JNEUROSCI.2572-11.2011

Harvey, B.M., Klein, B.P., Petridou, N., Dumoulin, S.O., 2013. Topographic Representation of Numerosity in the Human Parietal Cortex. Science (80-.). 341, 1123–1126. https://doi.org/10.1126/science.1239052

Havlicek, M., Uludağ, K., 2020. A dynamical model of the laminar BOLD response. Neuroimage 204. https://doi.org/10.1016/j.neuroimage.2019.116209

Hendriks, A.D., D'Agata, F., Raimondo, L., Schakel, T., Geerts, L., Luijten, P.R., Klomp, D.W.J., Petridou, N., 2020. Pushing functional MRI spatial and temporal resolution further: High-density receive arrays combined with shot-selective 2D CAIPIRINHA for 3D echo-planar imaging at 7 T. NMR Biomed. 33, 1–13. https://doi.org/10.1002/nbm.4281

Hermes, D., Nguyen, M., Winawer, J., 2017. Neuronal synchrony and the relation between the blood-oxygen-level dependent response and the local field potential. PLOS Biol. 15, e2001461. https://doi.org/10.1371/journal.pbio.2001461

Hofstetter, S., Cai, Y., Harvey, B.M., Dumoulin, S.O., 2021. Topographic maps representing haptic numerosity reveals distinct sensory representations in supramodal networks. Nat. Commun. 12, 221. https://doi.org/10.1038/s41467-020-20567-5

Hofstetter, S., Dumoulin, S.O., 2021. Tuned neural responses to haptic numerosity in the putamen. Neuroimage 238, 118178. https://doi.org/10.1016/j.neuroimage.2021.118178

Huber, L. (Renzo), Poser, B.A., Kaas, A.L., Fear, E.J., Dresbach, S., Berwick, J., Goebel, R., Turner, R., Kennerley, A.J., 2021. Validating layer-specific VASO across species. Neuroimage 237, 118195. https://doi.org/10.1016/j.neuroimage.2021.118195

Huber, L., Finn, E.S., Chai, Y., Goebel, R., Stirnberg, R., Stöcker, T., Marrett, S., Uludag, K., Kim, S.G., Han, S.H., Bandettini, P.A., Poser, B.A., 2020a. Layer-dependent functional connectivity methods. Prog. Neurobiol. 101835. https://doi.org/10.1016/j.pneurobio.2020.101835

Huber, L., Finn, E.S., Handwerker, D.A., Bönstrup, M., Glen, D.R., Kashyap, S., Ivanov, D., Petridou, N., Marrett, S., Goense, J., Benedikt, A., Bandettini, P.A., Poser, B.A., Bandettini, P.A., 2020b. Sub-millimeter fMRI reveals multiple topographical digit representations that form action maps in human motor cortex. Neuroimage 208. https://doi.org/10.1016/j.neuroimage.2019.116463

Huber, L., Goense, J., Kennerley, A.J., Trampel, R., Guidi, M., Reimer, E., Ivanov, D., Neef, N., Gauthier, C.J., Turner, R., Möller, H.E., 2015. Cortical lamina-dependent blood volume changes in human brain at 7T. Neuroimage 107, 23–33. https://doi.org/10.1016/j.neuroimage.2014.11.046

Huber, L., Handwerker, D.A., Jangraw, D.C., Chen, G., Hall, A., Stüber, C., Gonzalez-Castillo, J., Ivanov, D., Marrett, S., Guidi, M., Goense, J.B.M., Poser, B.A., Bandettini, P.A., 2017. High-resolution CBV-fMRI allows mapping of laminar activity and connectivity of cortical input and output in human M1. Neuron 96, 1–11. https://doi.org/10.1016/j.neuron.2017.11.005

Huber, L., Ivanov, D., Handwerker, D.A., Marrett, S., Guidi, M., Uludağ, K., Bandettini, P.A., Poser, B.A., 2018a. Techniques for blood volume fMRI with VASO: From low-resolution mapping towards sub-millimeter layer-dependent applications. Neuroimage 164, 131–143. https://doi.org/10.1016/j.neuroimage.2016.11.039

Huber, L., Ivanov, D., Krieger, S.N., Streicher, M.N., Mildner, T., Poser, B.A., Möller, H.E., Turner, R., 2014. Slab-selective, BOLD-corrected VASO at 7 tesla provides measures of cerebral blood volume reactivity with high signal-to-noise ratio. Magn. Reson. Med. 72, 137–148. https://doi.org/10.1002/mrm.24916

Huber, L., Tse, D.H.Y., Wiggins, C.J., Uludağ, K., Kashyap, S., Jangraw, D.C., Bandettini, P.A., Poser, B.A., Ivanov, D., 2018b. Ultra-high resolution blood volume fMRI and BOLD fMRI in humans at 9.4 T: Capabilities and challenges. Neuroimage 178, 769–779. https://doi.org/10.1016/j.neuroimage.2018.06.025

Hurley, A.C., Al-Radaideh, A., Bai, L., Aickelin, U., Coxon, R., Glover, P., Gowland, P.A., 2010. Tailored RF pulse for magnetization inversion at ultrahigh field. Magn. Reson. Med. 63, 51–58. https://doi.org/10.1002/mrm.22167

JASP team, 2021. JASP Version (0.14.1)[Computer software].

Jin, T., Kim, S.G., 2008. Improved cortical-layer specificity of vascular space occupancy fMRI with slab inversion relative to spin-echo BOLD at 9.4 T. Neuroimage 40, 59–67. https://doi.org/10.1016/j.neuroimage.2007.11.045

Kim, S.-G., Ogawa, S., 2012. Biophysical and physiological origins of blood oxygenation level-dependent fMRI signals. J. Cereb. Blood Flow Metab. 32, 1188–206. https://doi.org/10.1038/jcbfm.2012.23

Klein, B.P., Harvey, B.M., Dumoulin, S.O., 2014. Article Attraction of Position Preference by Spatial Attention throughout Human Visual Cortex. Neuron 84, 227–237. https://doi.org/10.1016/j.neuron.2014.08.047

Kleiner, M., Brainard, D., Pelli, D., Ingling, A., Murray, R., Broussard, C., 2007. What's new in psychtoolbox-3. Perception 36, 1–16.

Klink, P.C., Chen, X., Vanduffel, W., Roelfsema, P.R., 2021. Population receptive fields in nonhuman primates from whole-brain fMRI and large-scale neurophysiology in visual cortex. Elife 10. https://doi.org/10.7554/eLife.67304

Lerma-Usabiaga, G., Benson, N., Winawer, J., Wandell, B.A., 2020. A validation framework for neuroimaging software: The case of population receptive fields. PLoS Comput. Biol. 16, 1–18. https://doi.org/10.1371/journal.pcbi.1007924

Levin, N., Dumoulin, S.O., Winawer, J., Dougherty, R.F., Wandell, B.A., 2010. Cortical Maps and White Matter Tracts following Long Period of Visual Deprivation and Retinal Image Restoration. Neuron 65, 21–31. https://doi.org/10.1016/J.NEURON.2009.12.006

Lu, H., Basso, G., Serences, J.T., Yantis, S., Golay, X., Van Zijl, P.C.M., 2005. Retinotopic mapping in the human visual cortex using vascular space occupancy-dependent functional magnetic resonance imaging. Neuroreport 16, 1635–1640. https://doi.org/10.1097/01.wnr.0000181580.18636.ee

Lu, H., Golay, X., Pekar, J.J., van Zijl, P.C.M.M., Zijl, P.C.M. Van, van Zijl, P.C.M.M., 2003. Functional magnetic resonance imaging based on changes in vascular space occupancy. Magn. Reson. Med. 50, 263–274. https://doi.org/10.1002/mrm.10519

Lu, H., Hua, J., van Zijl, P.C.M., 2013. Noninvasive functional imaging of cerebral blood volume with vascular-space-occupancy (VASO) MRI. NMR Biomed. 26, 932–948. https://doi.org/10.1002/nbm.2905

Marques, J.P., Kober, T., Krueger, G., van der Zwaag, W., Van de Moortele, P.F., Gruetter, R., 2010. MP2RAGE, a self bias-field corrected sequence for improved segmentation and T1-mapping at high field. Neuroimage 49, 1271–1281.

https://doi.org/10.1016/j.neuroimage.2009.10.002

Menon, R.S., 2002. Postacquisition suppression of large-vessel BOLD signals in high-resolution fMRI. Magn. Reson. Med. 47, 1–9. https://doi.org/10.1002/mrm.10041

Mildner, T., Müller, K., Hetzer, S., Trampel, R., Driesel, W., Möller, H.E., 2014. Mapping of arterial transit time by intravascular signal selection. NMR Biomed. 27, 594–609. https://doi.org/10.1002/nbm.3098

Moeller, S., Pisharady, P.K., Ramanna, S., Lenglet, C., Wu, X., Dowdle, L., Yacoub, E., Uğurbil, K., Akçakaya, M., 2021. NOise reduction with DIstribution Corrected (NORDIC) PCA in dMRI with complex-valued parameter-free locally low-rank processing. Neuroimage 226. https://doi.org/10.1016/j.neuroimage.2020.117539

Ogawa, S., Lee, T.M., Kay, A.R., Tank, D.W., 1990. Brain magnetic resonance imaging with contrast dependent on blood oxygenation. Proc. Natl. Acad. Sci. U. S. A. 87, 9868–72. https://doi.org/10.1073/pnas.87.24.9868

Oliveira, Í.A.F., Roos, T., Dumoulin, S.O., Siero, J.C.W., van der Zwaag, W., 2021a. Can 7T MPRAGE match MP2RAGE for gray-white matter contrast? Neuroimage 240, 118384. https://doi.org/10.1016/j.neuroimage.2021.118384

Oliveira, Í.A.F., van der Zwaag, W., Raimondo, L., Dumoulin, S.O., Siero, J.C.W., 2021b. Comparing hand movement rate dependence of cerebral blood volume and BOLD responses at 7T. Neuroimage 226, 117623. https://doi.org/10.1016/j.neuroimage.2020.117623

Persichetti, A.S., Avery, J.A., Huber, L., Merriam, E.P., Martin, A., 2019. Layer-Specific Contributions to Imagined and Executed Hand Movements in Human Primary Motor Cortex. SSRN Electron. J. 1–5. https://doi.org/10.2139/ssrn.3482808

R Core Team, 2020. A Language and Environment for Statistical Computing. R Found. Stat. Comput.

Uludağ, K., Müller-Bierl, B., Uğurbil, K., 2009. An integrative model for neuronal activity-induced signal changes for gradient and spin echo functional imaging. Neuroimage 48,

150–165. https://doi.org/10.1016/j.neuroimage.2009.05.051

Victor, J.D., Purpura, K., Katz, E., Mao, B., 1994. Population encoding of spatial frequency, orientation, and color in macaque V1. J. Neurophysiol. 72, 2151–2166. https://doi.org/10.1152/jn.1994.72.5.2151

Vizioli, L., Moeller, S., Dowdle, L., Akçakaya, M., De Martino, F., Yacoub, E., Uğurbil, K., 2021. Lowering the thermal noise barrier in functional brain mapping with magnetic resonance imaging. Nat. Commun. 12, 5181. https://doi.org/10.1038/s41467-021-25431-8

Wandell, B.A., Winawer, J., 2015. Computational neuroimaging and population receptive fields. Trends Cogn. Sci. 19, 349–357. https://doi.org/10.1016/j.tics.2015.03.009

Winawer, J., Parvizi, J., 2016. Linking Electrical Stimulation of Human Primary Visual Cortex, Size of Affected Cortical Area, Neuronal Responses, and Subjective Experience. Neuron 92, 1213–1219. https://doi.org/10.1016/j.neuron.2016.11.008

Yu, Y., Huber, L., Yang, J., Jangraw, D.C., Handwerker, D.A., Molfese, P.J., Chen, G., Ejima, Y., Wu, J., Bandettini, P.A., 2019. Layer-specific activation of sensory input and predictive feedback in the human primary somatosensory cortex. Sci. Adv. 5, eaav9053. https://doi.org/10.1126/sciadv.aav9053

Chapter 6

General Discussion

General discussion

In this thesis, the overall aim was to investigate and mitigate typical 7T challenges for anatomical and functional purposes, specifically targeting neuroscience applications. In the first part of the present thesis, I have focussed on improvements in field homogeneity combining parallel transmit (pTx) capabilities and special pulse design for 7T, namely, TR-FOCI for more uniform inversion. Besides the structural purpose, the second part of this thesis focuses on implementing and investigating an alternative fMRI approach to BOLD.

The first part of the present thesis comprehends ***chapter 2***. I successfully showed that the combination of Universal pulses (Gras et al., 2017) for excitation and TR-FOCI pulse (Hurley et al., 2010) for inversion mitigate the transmit B1 field (B1+) inhomogeneity problem. Additionally, the combined MPRAGE (TR-FOCI + UPs) yielded higher SNR, CNR, and the gray-white matter contrast than the standard MPRAGE. We also compared the T1-weighted MPRAGE with the T1-weighted image acquired with the self-bias-field corrected MP2RAGE (Marques et al., 2010). For this case, the CNR and the gray-white matter contrast performance were superior to all MPRAGE acquisitions. Therefore, I concluded that the additional scan time of an MP2RAGE acquisition seems merited.

The second part of the present thesis comprehends the three following chapters. Starting from ***chapter 3,*** I successfully implemented the recent variant of VASO, called Slab Selective slab inversion VASO (SS-SI VASO) (Huber et al., 2014), specific for ultra-high-field (≥ 7T) scanners. This chapter investigated the linearity behavior of the VASO-CBV responses using a hand movement task. Previous studies found that the BOLD response tends to overestimate activation at very brief stimulus duration or short stimulus intensities. The reasons for this nonlinearity are still not fully understood. However, it is suggested that the significant part of the BOLD nonlinearity has a neuronal origin (Birn and Bandettini, 2005; Liu et al., 2009), and the remaining part is likely due to the vascular effects (Zhang et al., 2008). Here, I hypothesize that part of the nonlinearity may be driven by vascular nonlinearity effects (Liu et al., 2009), particularly the large vessel contributions. Because VASO promises higher microvascular specificity (arteriole and post-arterial CBV changes) with a lower sensitivity to the draining vein effect (Huber et al., 2017; Jin and Kim, 2008), we expect a different response when compared to BOLD. On the contrary, I observed a strong linear relationship between VASO-CBV and BOLD

responses, both similarly increasing with the movement rate and plateauing at high movement rates (≥ 1 Hz). As mentioned in chapter 3, a plausible explanation for this tight relationship between VASO-CBV and BOLD responses is that the CBV measurements reflect the nonlinear transformation from the stimulus to the neural response since CBV are closely related to the underlying neuronal activity.

Next, I investigated how the specificity of VASO-CBV compares to BOLD fMRI using digit selectivity measurements (Akselrod et al., 2017; Martuzzi et al., 2014; Olman et al., 2012). ***In chapter 4***, I hypothesized that the higher specificity of VASO-CBV would yield higher digit selectivity than BOLD. For this experiment, we recorded sub-millimeter VASO fMRI using individual finger movement (three fingers, thumb-index-little finger) and a stimulus based on a standard block-design task. I showed that VASO-CBV yields higher selectivity or less overlap between the digit clusters than BOLD for different metrics. Moreover, we demonstrate a consistent topographical representation of part of the sensorimotor digit regions (thumb-index-little fingers).

Finally, in **chapter 5**, I evaluated the feasibility of VASO-CBV for population receptive field mapping (pRF). Because of its distinct sensitivity to the microvascular blood volumes changes, I hypothesized that VASO-CBV would show smaller pRF sizes than BOLD. The VASO-CBV reliably shows similar polar angle and eccentricity maps to BOLD-based data. The pRF size increased systematically with eccentricity and going from V1 to V3, with high similarity between BOLD and VASO-CBV pRF sizes estimates. The expected higher microvascular specificity of VASO-CBV did not directly result in a smaller pRF size. These results suggest that the vascular contribution in the spatial pRF size is minimal or very similar for VASO-CBV and BOLD for the spatial resolution used here.

Considerations

Taking into account the first part of the present thesis ***(chapter 2)***, the combination of Universal Pulses for excitation and TR-FOCI pulse for inversion increased the SNR, CNR, and gray-white matter contrast compared to the standard MPRAGE sequence. These results show that the T1-weighted MPRAGE can be reliably improved and can be an alternative approach for clinical purposes or other applications where the segmentation of gray-white matter is not

the primary purpose. Another interesting point is in regard the temporal efficiency. This chapter uses a k-space shutter to increase the temporal efficiency by approximately 25% for the MPRAGE. We showed that using the k-space shutter did not compromise the image quality. Different methods such as Compressed Sensing (Dieckmeyer et al., 2021; Lustig et al., 2007), CAIPIRINHA (2D CAIPI) (Breuer et al., 2006; Falkovskiy et al., 2016), or wave-CAIPI (Bilgic et al., 2015; Polak et al., 2018), for example, can increase the temporal efficiency even further and accommodate the 7T setup for clinical reality.

There is an important remark on our results, specifically regarding spatial resolution. Higher spatial resolution (1mm or lower) may elicit different responses from the studies outlined in chapters 3 and 5, where we used 'conventional' 7T fMRI spatial resolution (1.5 and 1.75 mm isotropic voxels, respectively). Moreover, the higher specificity of VASO-CBV has proven to be highly effective when applied across cortical depth, targeting depth-dependent or layer fMRI questions, which is not the case in both studies. We could speculate that for pRF size estimates, the population of neurons contributing to the signal and the pRF size will decrease or show smaller width. As the neural point spread function of the pRF decreases at higher resolutions, the vascular component may become more evident. Hence, the difference between BOLD and VASO-CBV may become more apparent. We can also extend this speculation to the nonlinearity question. Smaller voxels may show the difference between the vascular and neural contribution to the linearity and a more apparent difference between BOLD and VASO-CBV signals. High-quality data at such high spatial resolution would then be very challenging; as shown for the pRF application in chapter 5, the scan time for VASO-CBV experiments would become practically unfeasible in terms of scan time.

Conclusion

This work investigated different approaches to improve image quality, focusing on correcting the $B1^+$ inhomogeneities and precision of functional measurements using VASO fMRI at Ultra-High Field MRI to get further insights into the human brain. It was shown that the combination of different methods **(chapter 2)** could significantly improve field uniformity reliably with the advantage of also gaining SNR and CNR for typical T1-weighted MPRAGE sequence. Regarding the VASO fMRI studies, I implemented the SS-SI VASO sequence to

record VASO-CBV and BOLD signals simultaneously. In **Chapter 3,** I observed a tight linear relationship between VASO-CBV and BOLD with respect to an increased hand movement rate in the motor cortex. In **chapter 4**, using sub-millimeter VASO and BOLD fMRI, I showed higher response selectivity for VASO-CBV or less overlap than BOLD. The results were consistent across participants and metrics, confirming the higher spatial specificity of VASO-CBV compared to BOLD. Finally, in **chapter 5**, I found similar pRF estimates for VASO-CBV and BOLD images. The present work focuses on High-Field MRI technical and fundamental aspects, aiming to improve image quality and overcome typical ultra-high field MRI challenges for anatomical and functional applications. In addition, by extending the VASO fMRI approach for different neuroscience questions, we got new insights that can help future clinical and neuroscientific studies.

References

Akselrod, M., Martuzzi, R., Serino, A., van der Zwaag, W., Gassert, R., Blanke, O., 2017. Anatomical and functional properties of the foot and leg representation in areas 3b, 1 and 2 of primary somatosensory cortex in humans: A 7T fMRI study. Neuroimage 159, 473–487. https://doi.org/10.1016/j.neuroimage.2017.06.021

Bilgic, B., Gagoski, B.A., Cauley, S.F., Fan, A.P., Polimeni, J.R., Grant, P.E., Wald, L.L., Setsompop, K., 2015. Wave-CAIPI for highly accelerated 3D imaging. Magn. Reson. Med. 73, 2152–2162. https://doi.org/10.1002/MRM.25347/ASSET/SUPINFO/MRM25347-SUP-0001-SUPPINFO.ZIP

Birn, R.M., Bandettini, P.A., 2005. The effect of stimulus duty cycle and "off" duration on BOLD response linearity. Neuroimage 27, 70–82. https://doi.org/10.1016/j.neuroimage.2005.03.040

Breuer, F.A., Blaimer, M., Mueller, M.F., Seiberlich, N., Heidemann, R.M., Griswold, M.A., Jakob, P.M., 2006. Controlled aliasing in volumetric parallel imaging (2D CAIPIRINHA). Magn. Reson. Med. 55, 549–556. https://doi.org/10.1002/mrm.20787

Dieckmeyer, M., Roy, A.G., Senapati, J., Wachinger, C., Grundl, L., Döpfert, J., Bertran, P.F., Lemke, A., Zimmer, C., Kirschke, J.S., Hedderich, D.M., 2021. Effect of MRI acquisition acceleration via compressed sensing and parallel imaging on brain volumetry. Magn. Reson. Mater. Physics, Biol. Med. 34, 487–497. https://doi.org/10.1007/S10334-020-00906-9/TABLES/9

Falkovskiy, P., Brenner, D., Feiweier, T., Kannengiesser, S., Maréchal, B., Kober, T., Roche, A., Thostenson, K., Meuli, R., Reyes, D., Stoecker, T., Bernstein, M.A., Thiran, J.P., Krueger, G., 2016. Comparison of accelerated T1-weighted whole-brain structural-imaging protocols. Neuroimage 124, 157–167. https://doi.org/10.1016/j.neuroimage.2015.08.026

Huber, L., Handwerker, D.A., Jangraw, D.C., Chen, G., Hall, A., Stüber, C., Gonzalez-Castillo, J., Ivanov, D., Marrett, S., Guidi, M., Goense, J., Poser, B.A., Bandettini, P.A., 2017. High-Resolution CBV-fMRI Allows Mapping of Laminar Activity and Connectivity of Cortical Input and Output in Human M1. Neuron 96, 1253-1263.e7. https://doi.org/10.1016/j.neuron.2017.11.005

Huber, L., Ivanov, D., Krieger, S.N., Streicher, M.N., Mildner, T., Poser, B.A., Möller, H.E., Turner, R., 2014. Slab-selective, BOLD-corrected VASO at 7 tesla provides measures of cerebral blood volume reactivity with high signal-to-noise ratio. Magn. Reson. Med. 72, 137–148. https://doi.org/10.1002/mrm.24916

Jin, T., Kim, S.G., 2008. Improved cortical-layer specificity of vascular space occupancy fMRI with slab inversion relative to spin-echo BOLD at 9.4 T. Neuroimage 40, 59–67. https://doi.org/10.1016/j.neuroimage.2007.11.045

Liu, Z., Rios, C., Yang, L., Zhang, N., Chen, W., He, B., 2009. Neural and Vascular Response Nonlinearity in Human Visual Cortex. Proc. 17th Sci. Meet. Int. Soc. Magn. Reson. Med. Honolulu 17, 510.

Lustig, M., Donoho, D., Pauly, J.M., 2007. Sparse MRI: The application of compressed sensing for rapid MR imaging. Magn. Reson. Med. 58, 1182–1195. https://doi.org/10.1002/MRM.21391

Marques, J.P., Kober, T., Krueger, G., van der Zwaag, W., Van de Moortele, P.F., Gruetter, R., 2010. MP2RAGE, a self bias-field corrected sequence for improved segmentation and T1-mapping at high field. Neuroimage 49, 1271–1281. https://doi.org/10.1016/j.neuroimage.2009.10.002

Martuzzi, R., van der Zwaag, W., Farthouat, J., Gruetter, R., Blanke, O., 2014. Human finger somatotopy in areas 3b, 1, and 2: A 7T fMRI study using a natural stimulus. Hum. Brain Mapp. 35, 213–226. https://doi.org/10.1002/hbm.22172

Olman, C.A., Pickett, K.A., Schallmo, M.P., Kimberley, T.J., 2012. Selective BOLD responses to individual finger movement measured with fMRI at 3T. Hum. Brain Mapp. 33, 1594–1606. https://doi.org/10.1002/hbm.21310

Polak, D., Setsompop, K., Cauley, S.F., Gagoski, B.A., Bhat, H., Maier, F., Bachert, P., Wald, L.L., Bilgic, B., 2018. Wave-CAIPI for highly accelerated MP-RAGE imaging. Magn. Reson. Med. 79, 401–406. https://doi.org/10.1002/MRM.26649/SUPPINFO

Zhang, N., Zhu, X.H., Chen, W., 2008. Investigating the source of BOLD nonlinearity in human visual cortex in response to paired visual stimuli. Neuroimage 43, 204–212. https://doi.org/10.1016/j.neuroimage.2008.06.033

Curriculum vitae

Ícaro Agenor Ferreira de Oliveira was born in Ribeirão Preto on 18 December 1985. His interest in MRI grew during his Bachelor in Medical Physics at the University of São Paulo (USP). He worked with Brain Perfusion throughout his Bachelor's degree using the non-invasive Arterial Spin Labeling (ASL) technique. In 2015, he continued to work in Professor Renata Leoni's laboratory graduating in 2017 Master's in science. In 2018, he started a PhD trajectory on Brain imaging at the Spinoza Centre for Neuroimaging, under the supervision of Serge Dumoulin, Wietske van der Zwaag and Jeroen Siero. The research over these four years has resulted in the present thesis.

Publications

Journal Articles

Oliveira, Í.A.F., Cai, Y., Hofstetter, S., Siero, J.C.W., van der Zwaag, W., Dumoulin, S.O., 2022. Comparing BOLD and VASO-CBV population receptive field estimates in human visual cortex. Neuroimage 248, 118868. https://doi.org/10.1016/j.neuroimage.2021.118868

Oliveira, Í.A.F., Roos, T., Dumoulin, S.O., Siero, J.C.W., van der Zwaag, W., 2021. Can 7T MPRAGE match MP2RAGE for gray-white matter contrast? Neuroimage 240, 118384. https://doi.org/10.1016/j.neuroimage.2021.118384

Oliveira, Í.A.F., van der Zwaag, W., Raimondo, L., Dumoulin, S.O., Siero, J.C.W., 2021. Comparing hand movement rate dependence of cerebral blood volume and BOLD responses at 7T. Neuroimage 226, 117623. https://doi.org/10.1016/j.neuroimage.2020.117623

Raimondo, L., **Oliveira, Í.A.F.**, Heij, J., Priovoulos, N., Kundu, P., Leoni, R.F., van der Zwaag, W., 2021. Advances in resting state fMRI acquisitions for functional connectomics. Neuroimage 243, 118503. https://doi.org/10.1016/j.neuroimage.2021.118503

Guimarães, T.M., Guimarães, M.R.C., **Oliveira, Í.A.F.**, Leoni, R.F., Santos, A.C., Dursun, S.M., Crippa, J.A.S., Bressan, R.A., Machado-de-Sousa, J.P., Lacerda, A.L.T., Hallak, J.E.C., 2021. Mononitrate Isosorbide as an Adjunctive Therapy in Schizophrenia. J. Clin. Psychopharmacol. Publish Ah. https://doi.org/10.1097/JCP.0000000000001388

Raimondo, L., Knapen, T., **Oliveira, Í. A.F.**, Yu, X., Dumoulin, S.O., van der Zwaag, W., Siero, J.C.., 2021. A line through the brain: implementation of human line-scanning at 7T for ultra-high spatiotemporal resolution fMRI. J. Cereb. Blood Flow Metab. 0271678X2110372. https://doi.org/10.1177/0271678X211037266

Conference Proceedings

Oliveira, Í.A.F.; Cai, Y.; Hofstetter; S., Siero; J.C.W., van der Zwaag; W., Dumoulin, S.O. Comparing population Receptive Field mapping using VASO-CBV and BOLD. In: Joint Annual Meeting ISMRM-ESMRMB, 2022, London.

Oliveira, Í.A.F.; Siero J.C.W; Dumoulin S. O.; van der Zwaag W. Improved digit selectivity using VASO-CBV in 7T motor mapping. In: Joint Annual Meeting ISMRM-ESMRMB, 2022, London.

Oliveira, Í.A.F.; van der Zwaag W.; Dumoulin S. O.; Siero J.C.W. BOLD and CBF nonlinear responses during a hand movement task with increasing movement rates using 3D-EPI VASO at 7T. ISMRM Virtual Conference. 2020.

Oliveira, Í.A.F.; Roos T.; Dumoulin S. O.; van der Zwaag W. Can 7T MPRAGE match MP2RAGE for gray-white matter contrast? ISMRM Virtual Conference. 2020.

Oliveira, Í.A.F.; van der Zwaag W.; Dumoulin S. O.; Siero J.C.W. Comparing VASO and BOLD responses elicited by different hand movement rates at 7T. In: XXV OHBM – Rome, Italy. 2019.

Oliveira, Í.A.F.; van der Zwaag W.; Dumoulin S. O.; Siero J.C.W. The effect of slice saturation in a 3D TFEPI SS-SI VASO for 7T applications. In: 36th ESMRMB – Rotterdam, The Netherlands. 2019.

Oliveira, Í.A.F.; van der Zwaag W.; Dumoulin S. O.; Siero J.C.W. Comparing VASO and BOLD response behavior with respect to movement rate at 7T. In: XI ISMRM Benelux Chapter– Leiden, The Netherlands. 2019.

Acknowledgments

This Ph.D. thesis is the result of teamwork. I would like to briefly express my gratitude to everyone who directly or indirectly contributed to this thesis.

My first acknowledgment goes to my supervisors, Wiestke van der Zwaag, Jeroen Siero, and Serge Dumoulin. Dear Wietske, Jeroen, and Serge thank you for having given me the opportunity of being part of your research groups. I was privileged to be part of three different lab groups. It was a fruitful and inspiring environment to make science. I learned a lot from all my colleagues at Spinoza and also from Jeroen's lab in Utrecht. Thank you for the weekly discussions, the encouragement, all the research advice, the manuscript corrections, presentation suggestions, and the feedback. I am thankful for what I have learned from all of you.

I would like to thank all Spinoza staff members for the unique atmosphere they provided and guaranteed during my Ph.D. time. It was a fantastic experience for me. Besides all my scientific experiences at the Spinoza, I'll never forget my first skating experience, boating trip, and many other good memories from our gathering and social moments.

To all my colleagues and friends thank you for helping me. Everyone that I shared moments at Spinoza contributed to this thesis. Especially my dear friends, Akhil, Shir, Yuxuan, Luisa, Gianfranco and Nikos. Thank you for your friendship, your company was an invaluable gift and an effective tool for overcoming the moments of frustration at work.

The last words are for you, my beloved and supportive wife Giuliana Takahashi, who is always by my side when I needed her most and has helped me throughout this journey.